Studying synthetic column density maps and absorption spectra from galactic wind models

Relatore:
Prof. Fabrizio Brighenti
Prof. Marcus Brüggen

Correlatore:
Dr. Wladimir Eduardo Banda-Barragán

Candidato:
Benedetta Casavecchia

Abstract

Galactic winds are multi-phase outflows that probe how feedback regulates the mass and metallicity of galaxies. Their cold phase, mainly observable with absorption lines, is often detected hundreds to thousands of pc away from the galactic plane and with velocities of hundreds of km s^{-1}. To understand observations, it is important to theoretically study how such lines are produced via numerical simulations of cloud systems exposed to winds and starburst UV backgrounds. In this thesis we study the thermodynamics, ion populations, and ion absorption lines of cold and warm radiative clouds evolving from magnetised wind-cloud systems and an unmagnetised shock-multicloud model. We account for radiative cooling with two different cooling floors and magnetic fields with two different orientations. In our wind-cloud simulations, cold clouds survive the interaction with the wind for longer, since they are less exposed to instabilities, than warmer clouds. Magnetic fields have a larger influence on warm clouds than in cold clouds. If transverse to the wind direction, the field creates a shield that confines the expansion of the cloud, delaying its evaporation. In our shock-multicloud simulation, cold gas at large distances is not accelerated by ram-pressure, but, instead, precipitates from mixed gas out of thermal equilibrium. To study ion populations and create synthetic spectra, we developed a flexible python interface to link our PLUTO simulations to TRIDENT via the YT-package infrastructure and CLOUDY. Our ion population analysis reveals that setting different cooling floors and magnetic fields affect the column densities of several ions. H I, O VI, Mg II, C III, and Si IV are more sensitive to the cooling floors, and H I, Mg II, C III, and Si IV can also trace the initial magnetic field direction, making them good candidates for comparisons with observations.

Sommario

I venti galattici permettono di indagare l'efficienza con cui il feedback stellare regola la distribuzione di massa e di metallicità nelle galassie. I venti galattici possiedono una componente di gas freddo, tracciabile mediante righe in assorbimento. Tale componente è spesso osservata a centinaia di pc di distanza dal piano galattico e con velocità di centinaia di km rms^{-1}. Lo studio dell'origine di tali righe richiede simulazioni numeriche di sistemi di nubi esposte a radiazione UV proveniente da regioni con massiccia formazione stellare. In questa tesi, studiamo la termodinamica, le popolazioni di ioni e le linee di assorbimento di nubi radiative cold e warm (rispettivamente a 50 e 10^4 K) interagenti con venti galattici. Le simulazioni analizzate consistono in modelli wind-cloud con campo magnetico e cooling radiativo, e modelli non magnetizzati di shock-multicloud, anch'essi con feedback da cooling radiativo. In questa tesi, consideriamo due temperature limite per il cooling radiativo, al di sotto delle quali il gas non può raffreddare ulteriormente, e campi magnetici con linee di campo aventi due diverse orientazioni. Nelle nostre simulazioni, le nubi cold, essendo meno soggette ad instabilità rispetto alle nubi warm, sopravvivono più a lungo all'interazione con il vento stellare. Inoltre, i campi magnetici hanno un'influenza maggiore sulle nubi warm rispetto a quelle cold. Nel caso in cui il campo magnetico è trasversale rispetto alla direzione di propagazione del vento, esso crea uno scudo che confina l'espansione della nube, ritardandone l'evaporazione. Nella nostra simulazione di shock-multicloud, il gas freddo, spesso osservato a grandi distanze dal piano galattico, non viene accelerato dalla ram-pressure. Piuttosto, viene generato dalla precipitazione della fase warm che viene perturbata a causa di instabilità termiche. Per studiare le popolazioni di ioni e creare spettri sintetici, abbiamo sviluppato un'interfaccia python flessibile che permette di collegare le nostre simulazioni PLUTO a TRIDENT tramite l'infrastruttura YT-package. La nostra analisi sulla popolazione di ioni rivela che l'implementazione di diverse temperature limite per il cooling radiativo e diversi campi magnetici influenza le densità di colonna degli ioni. In particolare, H I, O VI, Mg II, C III, e Si IV sono più sensibili alle due diverse temperature limite di cooling radiativo; e fra questi, H I, Mg II, C III e Si IV possono tracciare anche la direzione iniziale del campo magnetico, rendendoli buoni candidati per un eventuale confronto con le osservazioni.

Contents

Chapter 1

Introduction

It is now well known that galaxies are not isolated systems. Galaxies are dynamic systems and interact with other galaxies in their groups (e.g. Bregman [2007b]). They can grow via merger events or by accreting material from the intergalactic medium (e.g. Tumlinson et al. [2017]). Each galaxy is immediately surrounded by a galactic corona known as the circumgalactic medium (CGM), which contains gas, dust, and cosmic rays (e.g. Tumlinson et al. [2017]). Observations of such material reveal that the CGM is a complex and multi-phase environment regulated by feedback processes that allow for the exchange of matter and energy between the interstellar medium (ISM) and the intergalactic medium (IGM). Feedback processes can be due to star formation (e.g. Scannapieco & Broadhurst [2001], Scannapieco et al. [2001], Veilleux et al. [2005], Veilleux & Rupke [2005], Muratov et al. [2015]) or active galactic nuclei (AGN) (e.g. Scannapieco & Oh [2004], Fabian [2014], Kaviraj et al. [2017]). The former involves supernova feedback, stellar wind bubbles, superbubbles, and galactic winds; while the latter involves jets, radio lobes, AGN winds, and radiative pressure (e.g. Chapter 8.7, 8.8 of Cimatti et al. [2019]. Both types of feedback processes have a strong impact on a galaxy's evolution, its star formation rate (SFR) and its metallicity (e.g. Tremonti et al. [2004], Oppenheimer et al. [2010], Lu et al. [2015]).

In this chapter we explain the importance of CGM within both galactic and cosmological contexts. We describe how b studying this medium some solutions to problems related to the evolution of galaxies can be found. We also summarise how the CGM is studied nowadays, and discuss its multiphase structure. Finally, we explain how galaxies exchange matter and energy with the CGM via inflows and outflows processes.

1.1 The Major Problems of Galaxy Evolution and why we should study the CGM

The mechanisms involved in galaxy formation and evolution are many and complicated. Nowadays, progress has been made towards understanding these systems through cosmological simulations, astrophysical gas dynamical models, and multi-wavelength ob-

servations. However, there are still some open questions, such as: Why do galaxies have a lower baryon fraction than expected? How are metals distributed in the Universe? How do galaxies become and remain passive? How do galaxies sustain their star formation? A brief description of each of these questions is given below.

1.1.1   WHERE ARE THE MISSING BARYONS?

One of the most studied parameters in cosmology is the baryon fraction f_b, which is the ratio of the baryonic mass to the total mass in the Universe (see Chapter 6.7 of Cimatti et al. [2019]). According to the ΛCDM model, baryons should follow the gravitational collapse of dark matter halos, and cool down through radiative processes towards the centre of the halos. However, the baryon fraction expected from ΛCDM model is not the one actually observed; only a small amount of baryons, in fact, turns into stars or is found in the interstellar medium (ISM) (e.g. Fukugita & Peebles [2004], Spergel et al. [2007]). The only structures where we observe the expected baryon fraction are the most massive galaxy clusters. On smaller scales such as small clusters, galaxy groups, elliptical and spiral galaxies, the baryonic mass is only a fraction of what the models predict. The Milky Way is missing 2/3 of its baryons and less massive galaxies have retained less than 10% of their baryons (see Bregman [2007a], Chapter 6.7 of Cimatti et al. [2019]). Regarding the galactic scale, several possibilities have been considered: baryons may be in the halo but not yet detected because of instrumental limitations; baryons were accreted and subsequently ejected from the halos by, for example, galactic winds; or they were prevented from accreting into the halos from the beginning. To find an answer to this problem, investigating the CGM via observations and simulations is essential.

1.1.2   WHAT IS THE DISTRIBUTION OF METALS IN THE CGM?

Star-forming galaxies seem to retain a small fraction of the metals ($\sim 20-25\%$) produced in stars, and their dust (e.g Peeples et al. [2014]). It is thought that the metals are ejected from the galaxy via outflows (e.g. Tremonti et al. [2004]), but how they are radially distributed from the centre of the galaxy is still unclear. It is also not known whether the metals are ejected from the halo all together or recycled in the galaxy over a long period in the form of "halo fountains" (Oppenheimer & Davé [2008]). Thus, it would be interesting to study the CGM, in particular to observe how the metals are distributed outside galaxies.

1.1.3   HOW IS STAR FORMATION REGULATED WITHIN GALAXIES?

If galaxies were isolated systems, their ISM would last only a fraction of the time they have been taking to form stars (e.g. Dekel et al. [2013]). However, we know that galaxies are not isolated systems and somehow contain sufficient fuel for star formation to continue over several Gys. In addition, there is a difference between sub-L_* and super-L_*

galaxies in terms of their star formation history (e.g. Zolotov et al. [2012], Krumholz & Dekel [2012]). More massive galaxies tend to continuously form stars over time, while sub-L_* galaxies are more likely to have a bursty star formation history (e.g. Tumlinson et al. [2017]). These two different evolutions also imply different ways of accreting material from the cosmic web depending on the mass of the galaxy itself and its metallicity (e.g. Dekel & Woo [2003], Kereš & Hernquist [2009], Stewart et al. [2011], Nelson et al. [2013]).

Another outstanding problem involves quiescent galaxies, in particular how it is possible that they have become and remain passive. What we expect, in fact, is that the CGM gas cools down via radiative processes and becomes the new fuel for star formation. However, the CGM remains hot and does not collapse towards the centre, suggesting the existence of some mechanism, such as stellar or AGN feedback, that keeps it at high temperatures (e.g. Somerville et al. [2008]).

In this scenario, galactic inflows and outflows are crucial for the development of a model capable of fully describing the star formation history of the various galaxies. Therefore, it is important to observe and simulate the CGM in order to study these feedback mechanisms that cause mass motions towards or from the halos' centre.

1.2 The Circumgalactic Medium (CGM)

How galaxies accrete, eject, and recycle gas is the core problem for understanding their evolution. The CGM is where these interactions take place. The CGM is bounded externally by the virial radius or dark matter halo of the galaxy, and internally by the disk or ISM (see Tumlinson et al. [2017]). Some of the most debated questions about galaxy formation and evolution listed in the previous section are thought, as already mentioned, to be answered by looking into the structure of the CGM. In this section we describe how the CGM is studied and also its complex multiphase structure.

1.2.1 HOW DO WE STUDY THE CGM?

The properties of the CGM can be analysed in various ways:

- **Transverse absorption line studies**. Studying the spectral absorption caused by CGM gas clouds with respect to a background source offers several advantages since: it is a sensitive method even at very low column number densities (10^{12} cm^{-2}, see Tumlinson et al. [2017]), it can span a large range of column densities, and it does not depend on the redshift or luminosity of the host galaxy. For this kind of observations there is usually a background source which excites, with its radiation, the atoms in the CGM of the galaxies of interest. How spectra are generated is shown in the sketch of FIG 1.1, and we refer to that, not only for the "Transverse absorption line Studies", but also for "Down-the-barrel Spectroscopy" and "Emission-line Maps". Within the local Universe it is possible to use several lines of sight for

the same galaxy (e.g. Lehner et al. [2015], Bowen et al. [2016]), while at high redshift the radiation from background quasars lensed by galaxies along the line of sight is used (e.g. Rauch et al. [2011], Rubin et al. [2015]).

- **Stacking Analysis**. This method is used to study very faint sources (such as galaxy haloes) as it involves the summing of hundreds or thousands of spectra of the same source. Co-addition demolishes the statistical noise and brings out the average signal of CGM sources. Some examples can be found in Steidel et al. [2010], Zhu & Ménard [2013], and Peek et al. [2015].

- **Down-the-barrel Spectroscopy**. This type of spectroscopy uses background light from stars in the host galaxy and not from distant sources such as quasars, as it is shown also in FIGURE 1.1. Because of the Doppler effect caused by bulk motions, it is the preferred method for studying inflows and outflows in face-on star-forming galaxies, since the redshift of the lines indicates if the material is moving into or away from the galaxy. Some examples in the far-ultraviolet FUV, near-ultraviolet (NUV), and optical lines are Steidel et al. [2010], Bordoloi et al. [2011], Henry et al. [2015], and Chisholm et al. [2018].

- **Emission-line Maps**. Observations in emission search for photons released directly from the CGM. Since the emission measurement scales with n^2 and typical CGM densities are $n_H = 10^{-2}$ cm^{-2} or less, the study of emission lines is quite complicated and is only possible for galaxies in the local Universe (e.g. Anderson et al. [2013]), as it is underlined also in FIG 1.1. Such maps have been made for example for the Milky Way (MW) and other halo structures using the radio emission of the 21 cm H-line (e.g. Putman et al. [2012]. Other frequencies have also been investigated to study the CGM properties in other galaxies, such as UV/optical wavelength and the X-ray band (e.g. Vikhlinin et al. [2006], Hayes et al. [2016]).

- **Hydrodynamic Simulations**. Simulations play a key role in connecting physical models with observations. Within a simulation the evolution of the CGM and the galaxy can be controlled and monitored in order to find a scenario as close as possible to what is observed today. The most widely used methods for simulating the CGM are smoothed particles hydrodynamics (SPH) handled by e.g. Gadget (Oppenheimer et al. [2016]), Gasoline (Gutcke et al. [2017]) and GIZMO (Muratov et al. [2017]); adaptive mesh refinements (AMR) simulations handled by e.g. Enzo (Hummels et al. [2013]) and moving mesh simulations, e.g. AREPO and ILLUS-TRIS Suresh et al. [2017]. From the numerical perspective, the study of galaxy evolution is done either through cosmological simulations on the Mpc scale, where it is possible to observe the behaviour and interaction of several galaxies together (e.g. Vogelsberger et al. [2014]), or through high-resolution simulations that investigate the interaction between atomic and molecular clouds, and galactic winds, reaching pc and sub-pc resolutions (e.g Armillotta et al. [2016], Banda-Barragán et al. [2016],

Banda-Barragán et al. [2018], Banda-Barragán et al. [2019], Banda-Barragán et al. [2020], Banda-Barragán et al. [2021]). Further details can be found in Chapter 2 of this thesis.
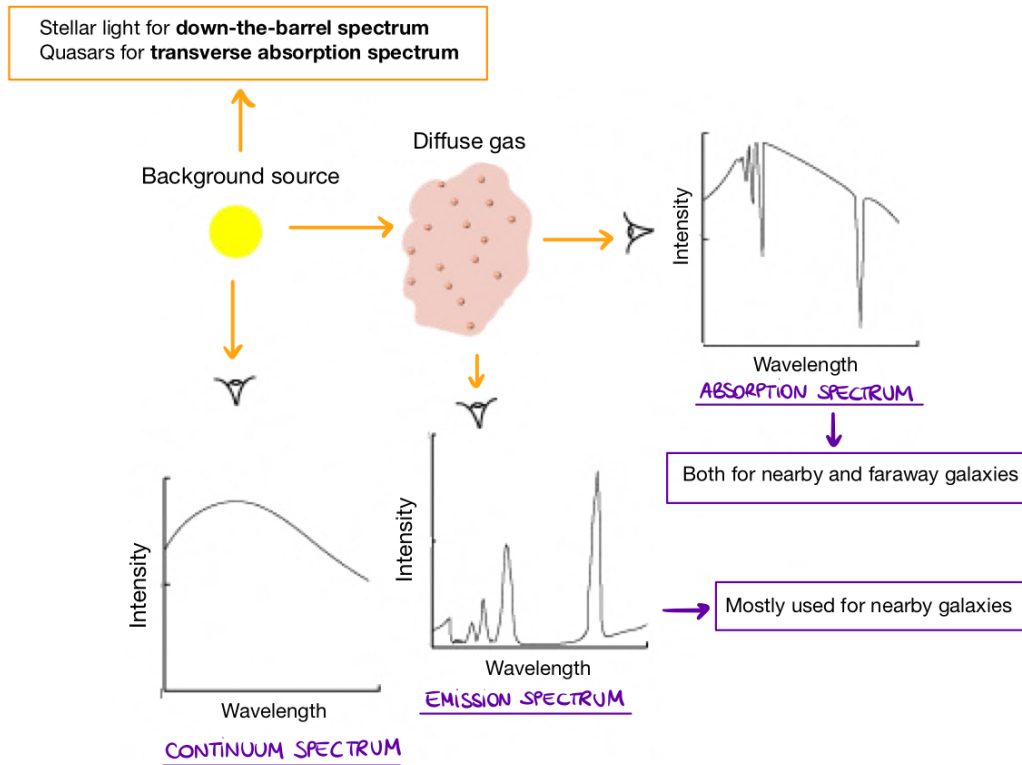
Figure 1.1: Production of absorption and emission lines. The radiation of a background source, once it interacts with some gas located between the source and the observer, is deprived of some photons that are absorbed by the CGM. These photons are then, re-emitted in other directions. The backgroud sources can be a distant quasars for transverse absorption spectra, or the stellar radiation of the observed galaxy, for down-the-barrel spectra.

1.2.2 HOW IS THE CGM STRUCTURED?

By observing the CGM, one can admire its multi-phase nature and complex dynamics. Empirically, a gas is said to be multi-phase when many metal ions spanning an order of magnitude in ionization potential energy are found within the same absorber system (Tumlinson et al. [2017]). If precise measurements for each ion can be obtained, then, gas flow speeds, their metallicity, and their baryon contents would be well constrained. However, not all ionisation states of each element are found at accessible wavelengths.

The CGM consists of a hot component (10^6 K) close to the virial temperature also called hot halo or corona.

$$T_{vir} \simeq 6.0 \times 10^5 \left(\frac{\mathcal{M}_{vir}}{10^{12} M_\odot} \right)^{2/3} \left(\frac{h}{0.7} \right)^{2/3} K \qquad (1.1)$$

This value is computed at $z = 0$ and by assuming $\nu = 0.6$ (for more details see Chapter 8.2 of Cimatti et al. [2019]). The hot component is observable in X-ray in emission (e.g Anderson et al. [2013]) and absorption along the QSO line of sight (e.g Gupta et al. [2012]). Direct spectroscopic evidence of hot gas comes from lines belonging to highly ionised metals which correlates with the low ionisation of High Velocity Clouds (HVCs) (e.g. Lehner et al. [2009], Wakker et al. [2012]). At high frequencies such as in the extreme-ultraviolet (EUV), some tracers of hot gas are Mg X, Si XII, which have been used to detect cold gas haloes in a few elliptical and spiral galaxies (e.g. Anderson et al. [2016]).
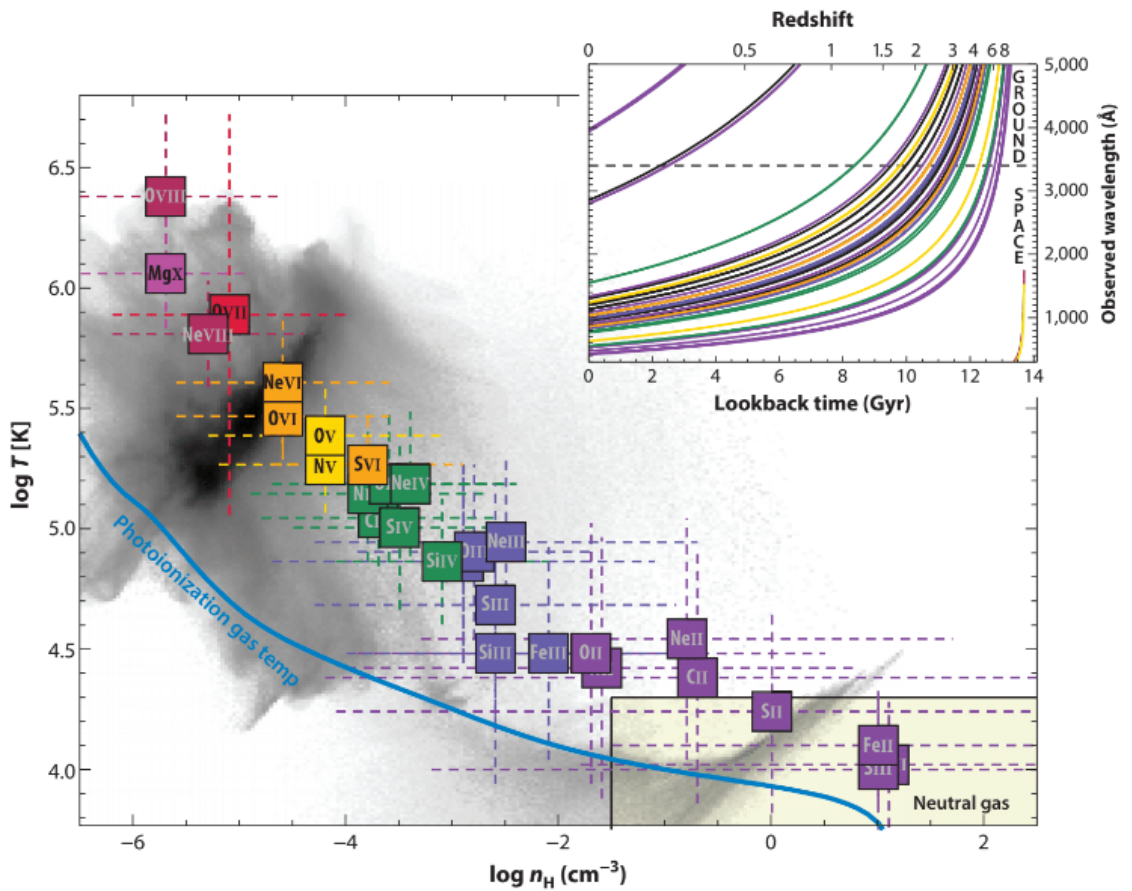
Figure 1.2: List of CGM ions with their respective density and temperature ranges at which they can be observed. The graph is taken from Tumlinson et al. [2017]. and the insert in the top right corner indicates the shift of the lines in Angstrom with the respect to the Lookback time in Gyr.

Other gas phases also found at lower temperatures are: warm component ($10^{4-5.5}$ K), mainly detected by C IV, N V, Ne VII, O VI, Ly alpha, Si II, Si II, Mg II, and C II absorption(e.g. Werk et al. [2016], Tchernyshyov et al. [2021], de la Cruz et al. [2021]); and finally, cold component with T$< 10^4$ K observed by low or neutral ions such as H I, Na I,

Ca II, and dust (e.g. McClure-Griffiths et al. [2013]). A graphical summary of the ions that can be observed at various temperatures and densities is shown in FIGURE 1.2; however, an accurate estimate of the mass of each component is not yet possible, making it difficult to give a definitive solution to the missing baryon problem. Kinematically, the complexity of the CGM is revealed by the detection of ions breaking into different components with different velocities and line widths as can be seen in FIGURE 1.3. The combination of aligned and unaligned components between the ionisation states reflects the presence of multiple clouds or streams. In addition, information on the column density N and the velocity offset v of each component can be deduced from the fit of the Voigt profiles. Therefore, from the spectroscopic study of the CGM, important information on the gravitational potential of the galaxy, mass motions and turbulence can be obtained, since these processes can affect the position and the width of the lines.
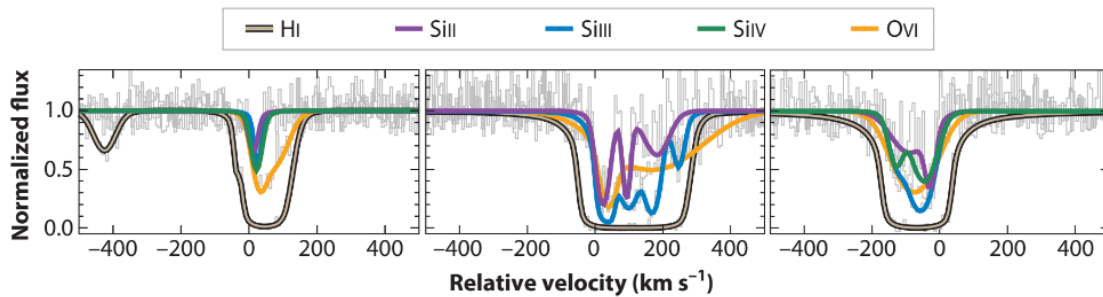
Figure 1.3: CGM absorption lines. These spectra are taken from Tumlinson et al. [2017] and represent the shape of some absorption spectral lines produced by CGM ions.

1.3 Inflows and Outflows

From observations, as mentioned above, it has been seen that the CGM is a large gas reservoir with complicated kinematics inside, which is difficult to study, especially for transverse line-of-sight absorption line studies. Furthermore, simulations show that the CGM possesses well-ordered large-scale structures that testify to accretion and outflow phenomena, such as cold gas filaments or biconical jets (e.g. Shen et al. [2012], Corlies & Schiminovich [2016]). The presence of these mass motions, however, seems to be less dominant at low redshift, where the CGM appears to be more well mixed (e.g Muratov et al. [2015]). Down-the-barrel observations are the best instrument to understand if the gas stream we observe is accreting onto the galaxy or is outflowing, based on whether it is redshifted or blueshifted, respectively. The subsections below explain how inflow and outflow phenomena are studied through CGM simulations and observations.

1.3.1   INFLOWS: HOT AND COLD ACCRETION MODELS.

Both analytical computations and simulations seem to indicate the existence of two modes of accretion: the hot mode, in which the gas is heated through shocks to the virial temperature, and the cold mode, in which the gas is still cold when it reaches the centre of the halo. The latter is common in systems where cooling is more efficient, i.e. in systems where the virial temperature is below the critical virial mass $cal M_{sh}$ at which there are no virial shocks (see Chapter 8.2 of Cimatti et al. [2019]). A summary diagram is shown in FIGURE 1.4 where it can be seen how, from Nelson et al. [2013]'s simulations, the type of accretion varies as a function of redshift and galaxy mass. In the hot mode, on the other hand, baryons are accreted with a temperature $> 10^5$ K (e.g Nelson et al. [2013]); however, since the accretion is not spherically symmetric, it is possible that cold streams form and reach the centre of the halo, even if the virial mass $\mathcal{M}_{vir}$ is greater than $\mathcal{M}_{sh}$. The presence of cold filaments in galaxies with $\mathcal{M}_{vir} > \mathcal{M}_{sh}$ seems to be dominant at high redshift, where the gas in the streams is quite dense and the cooling time is short; while far from the streams the accretion operates mainly in the hot mode (see Dekel et al. [2013]).
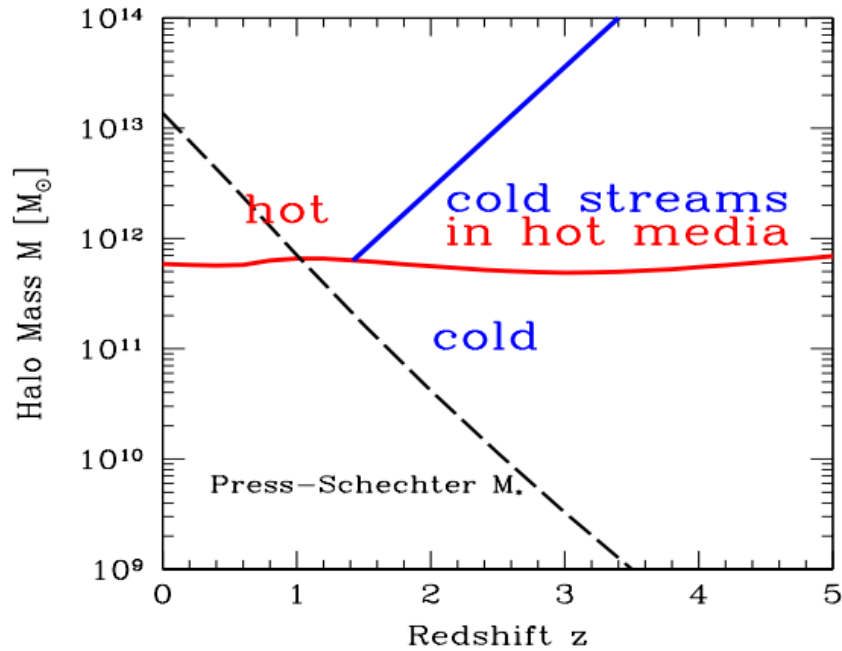
Figure 1.4: Different types of accretion in galaxies. The x-axis shows the redshift and the y-axis the mass of the dark matter halo. The red line separates cold accretion (bottom) from hot accretion (top). On the right of the blue line, instead, is reported a regime where the accretion on galaxies occurs through cold streams in a hot medium. The plot is taken from Dekel et al. [2013]

Also in the MW it is possible to observe evidence of accretion, thanks to the observation of blueshifted High Velocity Clouds and striking Magellanic Streams. HVCs have been

observed at a radius of 10 kpc from the centre, with velocities of $100 - 300 \, \mathrm{km \, s^{-1}}$, imply-ing that they will reach the MW disc in 10^{7-8} years (e.g. Putman et al. [2012]). The Magel-lanic Stream instead contains $2 \times 10^9 M_\odot$ of neutral and ionised gas and can provide a SFR $\sim 5 M_\odot \, \mathrm{year^{-1}}$ (e.g Tepper-García et al. [2015]). On the other hand, for external systems, it has been possible to observe clear signs of inflows in galaxies located at z=0.5 through Keck spectroscopy and Hubble imaging (e.g. Rubin et al. [2012]). These inflows typically have velocities of 80-200 km/s in star-forming galaxies with $log \mathcal{M}_\star / M_\circ = 9.5 - 10.5$. However, this kind of observations always provide lower limits for the estimation of the increased mass, since inflow streams are often obscured by outflow phenomena and emission from the ISM of the galaxy (e.g Steidel et al. [2010]).

1.3.2 OUTFLOWS: HOW STELLAR FEEDBACK INFLUENCES THE OBSER-VATIONAL PROPERTIES OF GALAXIES.

One of the largest evidences of outflows is the presence of metals outside galaxies, and simulations show that only robust outflows can justify such a large amount (e.g. Hummels et al. [2013], Suresh et al. [2017]). The presence of high-metal ions can be useful for setting constraints on the outflow phenomena that occurred during galaxy evolution. Observational evidence of outflows is present at all redshifts (e.g Veilleux et al. [2005]). In the near Universe, large multi-phase outflow streams have been observed in starburst galaxies (e.g. M82) and also in the MW (e.g. Fox et al. [2005]). Observations using down-the-barrel spectroscopy, in this case, can be useful to set estimate the mass and velocity of these outflows (e.g Martin [2005], Rubin et al. [2012]), but it still remains difficult to understand how far into the CGM these winds propagate. It is possible that the bulk of the energy that reaches outside the galaxy, is in the hot corona, while the bulk of the mass resides in the cold phase of the CGM (see Strickland & Heckman [2009]). Absorbers and transverse sightlines can also provide additional constraints on the impact of the winds on the CGM and how the abundance of certain ions can correlate with some galaxy fea-tures. For example, thanks to the COS-Halos survey it was possible to learn how in O VI absorbers galaxies, the abundance of O VI is directly proportional to the SFR and stellar mass of a galaxy (e.g. Tchernyshyov et al. [2021]). All the observations together highlight how most of the CGM has been fed by outflows and how, from its study, it is possible to obtain information on the past and present evolutionary history of the galaxy.

Chapter 2

Galactic Winds
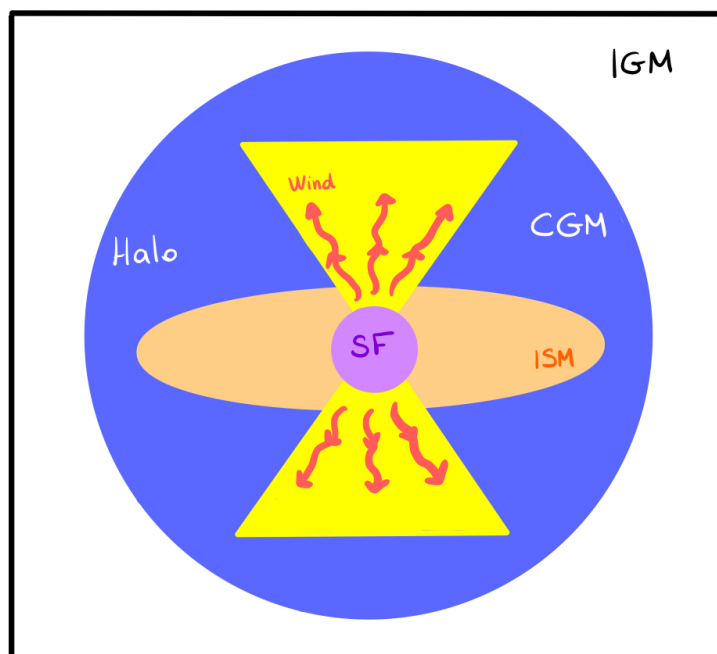
Figure 2.1: Galactic winds model. The sketch represents how galactic winds can be thought as an outflow of mass and energy starting from the star-forming region in the galactic center and ending in the CGM.

As mentioned in the previous chapter, from the CGM observations we can appreciate the existence of multi-phase gas and also outflows that advect gas from the ISM and eject it out of the galaxy. The main structure of a nuclear galactic wind, driven by star formation, is shown in FIG 2.1, where we can see the bi-conical structure of the wind, which is generated by the star-forming region in the centre of the galaxy and then flows into and through the CGM. However, there are still some unresolved questions related to the physics and history of the CGM. For example: how is it possible for gas at different

temperatures to co-exist within the same outflowing medium? What is the origin of the cold gas observed in the CGM? How is it possible to observe high-velocity clouds of cold gas hundreds of parsecs away from the galactic plane? In this chapter we will explain how observations and particularly simulations of galactic winds can largely contribute to answering these questions. Initially, we discuss some observational evidences of galactic winds in the MW and in the starburst galaxy M82. Then, we describe an analytical model on the formation of galactic winds. Afterwards, we focus on the theories that try to explain the presence of high-speed cold gas at large distances from the galactic plane and, finally, we discuss how simulations at different scales can contribute to answering the above questions.

2.1 Observations of nearby Galactic Winds in M82 and in the Milky Way

2.1.1 THE SUPERWIND IN STARBURST GALAXY M82

The starburst galaxy M82 is located at 3.6 Mpc from us, it has a star formation rate (SFR) of about $7 - 10 M_\odot$ per year and the starburst regions has an estimated radius of 400 pc (see Heckman & Thompson [2017]).There are many observations of multi-phase gas in M82 attesting to the presence of an outflow pattern that seems to be consistent with a galactic wind, as for the example the H_α emission shown with red color in FIG 2.2.

Figure 2.2: Emission of H_α in M82 taken from :http://hubblesite.org/image/1876/gallery. The emission in red represents the distribution of H_α in the starburst M82, which outlines the shape of the galactic wind.

The following are some of the various gas phases at different temperatures observed in this galaxy:

- **Hot gas**. This medium has been detected by X-ray emission, it has an estimated temperature of $T \sim 5 - 10 \times 10^6$ K (see Lehnert et al. [1999]) and, by observing the outflow, its location seems to be more internal to the wind than other phases.

- **Warm ionized medium**. In M82, one of the earliest observations able to track the presence of an outflow dates back to Jones et al. [1996] with the detection in emission in the optical wavelenghts (in particular H_α lines) of a filamentary structure extending from the centre of the starburst, in direction perpendicular to the Galactic plane. This warm gas has a temperature of $T \sim 10^4$ K, and seems to map quite well the biconical shape that characterizes galactic winds, as shown previously in FIG 2.1 and FIG 2.2. This gas has a speed of about 600 km s^{-1} and its structure correlates co-spatial with the hot phase. Probably this warm gas is an intermediate phase between the hot wind gas and the cooler gas which the wind is interacting with (see Shopbell & Bland-Hawthorn [1998]).

- **Cold and warm molecular gas**. This two phases have been observed respectively via spectroscopy in the mm-wave and in the mid/near IR (see Veilleux et al. [2009], Beirão et al. [2015], and Leroy et al. [2015]), and has a velocity on the order of $\sim 10^2$ km s^{-1}. The tracers used to study this cold gas are the HI 21 cm line, as in Leroy et al. [2015], or the [OI] and [CII] fine-structure lines in the far-IR (see Contursi et al. [2013]).

- **Dust**. It has been observed in the IR by thermal emission (see Contursi et al. [2013] and Leroy et al. [2015]) or by imaging in the far-UV due to the starburst radiation scattered by the grains (see Hoopes et al. [2005]). The velocity of the grains can only be measured near the starburst and appears to be within 100 km s^{-1} (see Yoshida et al. [2011]).

2.1.2 THE SUPERWIND IN THE MILKY WAY (MW) GALAXY

Also in the MW some features related to a past activity of galactic wind have been observed, first evidences of the nuclear wind in the MW are much older are reported in Bland-Hawthorn & Cohen [2003]. Further evidence was the discovery, with the Fermi-LAT (Fermi large-area telescope) γ-ray instrument, of the Fermi bubbles. They consist of two bubbles extending 50 degrees (i.e., ~ 8 kpc) above and below the Galactic center, with a width of about 40 degrees in longitude (see Su et al. [2010]), containing thermal gas with a temperature in the range of $10^6 - 10^8$ K (see Miller & Bregman [2016]). It is thought that the formation of these bubbles is related to either a past high star formation activity in the Galactic centre or past AGN-like activity from the SMBH at the centre

of the MW (see Crocker [2012]). More recent observations done with eROSAT, have detected the presence of two additional bubble-like structures, and, as reported in Predehl et al. [2020], they are roughly co-spatial with the Fermi bubbles. This is probably because they are generated by galactic winds as well (see FIGURE **??**). Additional proof comes from the S-Pass survey that, thanks to the polarized radio emission of celestial sources in the S band, i.e. at a frequency of 2.3 GHz, allowed to observe also radio counterparts of the bubbles (see Carretti et al. [2013]). Similarly to M82, warm and cold gas located at far distances from the Galactic plane and at high velocities has also been observed in the MW. In particular, a study of McClure-Griffiths et al. [2013] reported the detection of atomic hydrogen clouds at latitudes from the Galactic plane equivalent to 400 pc to 1 kpc, with a velocity of $\sim 200 - 300 \mathrm{kms}^{-1}$, which are likely associated with an outflow generated by the high star formation at the centre of the Galaxy.
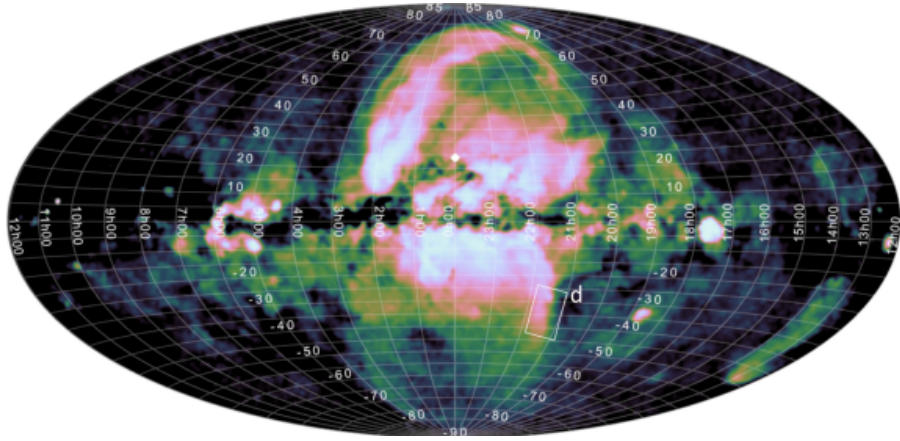
Figure 2.3: The soft-X-ray eROSITA bubbles. False-colour map of extended emission detected by eROSITA in the 0.6˜1.0 keV range, by Predehl et al. [2020].

2.2   Analytical model of stellar-driven bubbles

In this section we analyse in more detail the structure of a stellar-driven wind, what its origin is and how, with a simple analytical model, we can understand its linear evolution. The model is also reported in Chapter 8.7 of Cimatti et al. [2019].

The final moments of the evolution of very massive OB stars involves the ejection of the outer layers of the star in the form of a stellar wind, powered by radiation pressure. The stellar wind generates a bubble that expands into the ISM and its structure is shown in FIG 2.4. The wind launches high-speed particles that perturb the surrounding medium and generate an initial S2 shock. However, since the high-velocity particle flux from the star is continuous, it forms a reverted shock S1 that propagates into the wind and perturbs it. What we expect is that inside the bubble, due to the high temperatures ($T \sim 10^7$ K) caused by S1, it is difficult for cooling to be efficient, therefore, the bubble expands adiabatically. On the other hand, the shocked ISM shell manages to radiate away much of the energy and cool quickly. Thus, the final configuration involves an adiabatic bubble

surrounded by a radiative sphere.
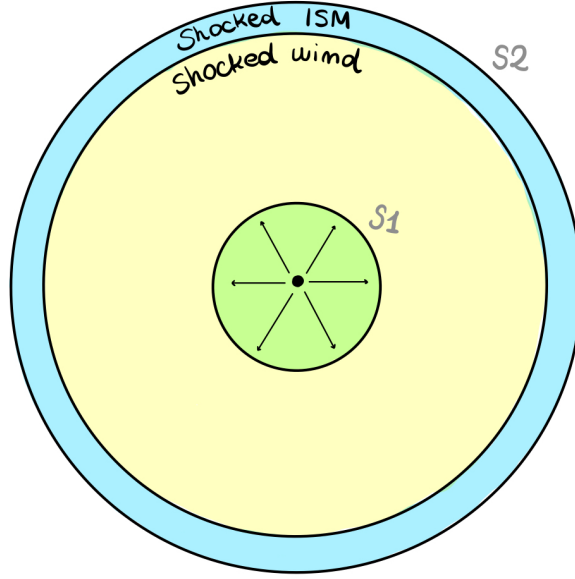
Figure 2.4: Stellar wind bubble. Sketch representing the different shock regions generated by the interaction between the stellar wind and the ISM, adapted from Cimatti et al. [2019].

The evolution of the system, at this point, can be described using the energy conservation equation:

$$\frac{\mathrm{d}E_b}{\mathrm{d}t} = L_w - P_b \frac{\mathrm{d}V}{\mathrm{d}t} \tag{2.1}$$

where E_b is the total energy of the bubble, P_b is the pressure the bubble exerts on the shell, V the volume of the bubble, and L_w is the mechanical luminosity, i.e., the kinetic energy of the wind per unit time:

$$L_w \equiv \frac{1}{2}\dot{M}_w v_w^2 \simeq 1.3 \times 10^{36} \left(\frac{\dot{M}_w}{10^{-6}\ M_\odot\ \mathrm{yr}^{-1}}\right)\left(\frac{v_w}{2\times 10^3\ \mathrm{km\ s}^{-1}}\right)^2\ \mathrm{erg\ s}^{-1} \tag{2.2}$$

In this equation $\dot{M}_w$ is the wind mass outflow and v_w is the velocity of the wind. Expression 2.2 can be substituted into equation 2.1 and solved in order to find the radius of the shell, r_{sh}:

$$P_b = \rho_0 \left(\frac{1}{3}r_{sh}\ddot{r}_{sh} + \dot{r}_{sh}^2\right) \tag{2.3}$$

If we assume a thin shell it is possible to rewrite $E_b = (3/2)P_bV$ for $\gamma = 5/3$, $V = (4\pi/3)r_{sh}^3$, and also $v_{sh} = \dot{r}_{sh} = \frac{\mathrm{d}r_{sh}}{\mathrm{d}t}$. If we assume that the mass of the ISM with density ρ_0 collected by the shock remains inside the bubble, then:

$$r_{sh} \simeq 7.0 \left(\frac{L_w}{10^{36} \text{ erg s}^{-1}} \right)^{1/5} \left(\frac{\mu n_0}{1 \text{ cm}^{-3}} \right)^{-1/5} \left(\frac{t}{10^5 \text{ yr}} \right)^{3/5} \text{pc} \qquad (2.4)$$

Consequently, the speed of the shock is:

$$v_{sh} \simeq 41.3 \left(\frac{L_w}{10^{36} \text{ erg s}^{-1}} \right)^{1/5} \left(\frac{\mu n_0}{1 \text{ cm}^{-3}} \right)^{-1/5} \left(\frac{t}{10^5 \text{ yr}} \right)^{-2/5} \text{km s}^{-1} \qquad (2.5)$$

So, in the presence of a constant source of kinetic energy generated by the stellar wind there is a fairly fast growth of the bubble radius.

In our Galaxy most of the OB stars reside within associations or clusters. If we assume that from the collapse of Giant Molecular Clouds (GMCs) the stars born there are coeval, then we can expect the simultaneous emission of stellar winds by a hundred massive stars, in a confined region. The combined action of so many stars can cause the formation of a superbubble and its evolution is similar to the model described above, but re-scaled for more stars (this phase is called stellar wind phase). After about 1 Myr the most massive stars end their unstable phase, stop producing winds and explode into SNe type II; consequently the superbubble expands even more because it is then powered by SNe explosions (supernova phase). If we consider this phase to last until 8 $M_\odot$ stars leave the main-sequence, $\tau_{MS}(8 \ M_\odot) \approx 3 \times 10^7$ yr. At this point, we can estimate the luminosity emitted by a superbubble generated by stars of an association as follows:

$$L_{SN} \approx \frac{N_{SN} E_{SN}}{\tau_{MS(8 \ M_\odot)}} \approx 10^{38} \left(\frac{N_{SN}}{100} \right) \left(\frac{E_{SN}}{10^{51} \text{ erg}} \right) \text{erg s}^{-1} \qquad (2.6)$$

Where E_{SN} is the energy of a SN II and N_{SN} the number of SNe. Equations 2.4 and 2.5 can be written as:

$$r_{sh} \approx 70 \left(\frac{N_{SN}}{100} \right)^{1/5} \left(\frac{E_S N}{10^{51} \text{ erg}} \right)^{1/5} \left(\frac{\mu n_0}{1 \text{ cm}^{-3}} \right)^{-1/5} \left(\frac{t}{10^6 \text{ yr}} \right)^{3/5} \text{pc} \qquad (2.7)$$

$$v_{sh} \approx 41 \left(\frac{N_{SN}}{100} \right)^{1/5} \left(\frac{E_S N}{10^{51} \text{ erg}} \right)^{1/5} \left(\frac{\mu n_0}{1 \text{ cm}^{-3}} \right)^{-1/5} \left(\frac{t}{10^6 \text{ yr}} \right)^{-2/5} \text{km s}^{-1} \qquad (2.8)$$

As the mechanical luminosity of the stellar wind phase and the supernova phase is about the same, since the second phase lasts about 10 times as long as the first; then SNe contribute much more in the feeding of superbubbles. From the formulas above we can deduce that superbubbles can expand for 10 Myr and reach the size of hundreds of pc. If we assume a spiral galaxy, the amount of friction that the superbubble experiences along the disc is much greater than in the vertical direction; consequently the bubble will no longer expand with spherical symmetry but will have a faster vertical expansion, this producing a biconical structure. Usually, galactic winds have a biconical shape, as can be seen in FIG 2.1 and FIG 2.2, and are responsible for the outflow of cold gas from the disc

into the CGM.

2.3 Why is Cold Gas Observed in The CGM at High Speeds?
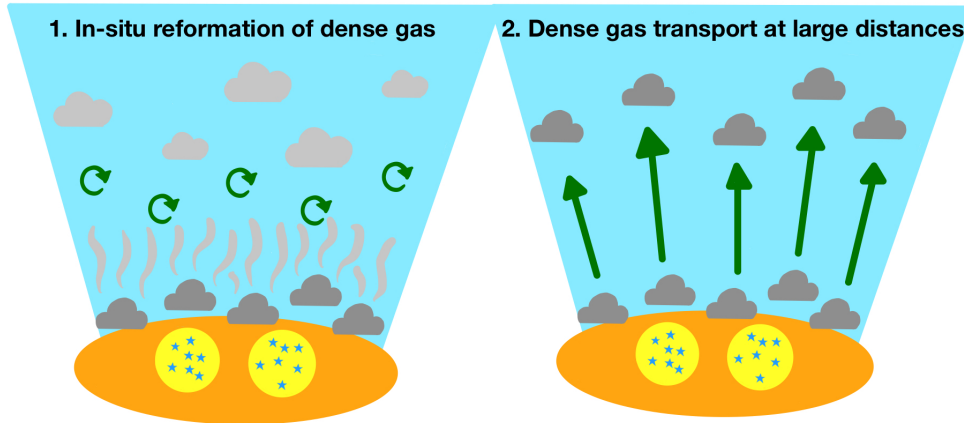
Figure 2.5: Cold gas in galactic winds. The two sketches illustrate how cold gas in galactic winds can be generated from the recycling of heated gas stripped from the ISM by the galactic wind, which, then, recondenses into the CGM (panel a); or from the displacement of cold gas by the galactic wind (panel b).

An important puzzle in galactic wind theory is to understand how to accelerate cool atomic and warm ionized gas to the observed velocities of hundreds and even thousands of km s^{-1} (e.g. McClure-Griffiths et al. [2013]). There are many models trying to address this issue and, as can be seen in FIG 2.5, they are divided mainly into two categories. Cold gas at high velocities can be generated by the collapse of the hot medium ejected by the stellar wind, or atomic/molecular gas clouds can be directly accelerated by outflow through, for example, ram pressure, cosmic ray pressure, or radiation pressure, and reach certain altitudes without being completely destroyed. In this section we will report some of these models.

2.3.1 HIGH SPEED COOL GAS FROM RADIATIVE COOLING OF THE HOT WIND

One way to produce fast outflows of cool/warm gas is via the precipitation from the hot phase. In the case of an energy-loaded wind, the mass outflow rate, $\dot{M}_{ED}$, can be written as (see Chapter 8.7 of Cimatti et al. [2019]):

$$\dot{M}_{ED} \approx \left(\frac{\alpha}{0.1}\right) \left(\frac{SFR}{M_\odot \text{ yr}^{-1}}\right) \left(\frac{v_w}{300 \text{ km s}^{-1}}\right)^{-2} M_\odot \text{ yr}^{-1} \qquad (2.9)$$

where α is the thermal efficiency and indicates how much of the energy from the SNe

explosion is transferred to the wind. At this point, the mass loading factor can be defined as (see Heckman & Thompson [2017]):

$$\beta \equiv \frac{\dot{M}}{SFR} \tag{2.10}$$

and for powerful winds with $\beta \geq 1$, the cooling time can become shorter than the dynamic time-scale. Thus, if the wind starts at a distance R from the centre of the galaxy, with temperature $T_{hot} \simeq 3/20 \left(m_p/k_B \right) v_w^2 \simeq 2 \times 10^7 \ (\alpha/\beta)$ K, and it cools adiabatically, on a large scale ($r > R$), its temperature can become lower than 10^7 K (see Wang [1995]). In this regime line-metal cooling dominates over bremsstrahlung, which make the medium radiatively unstable, as reported by Thompson et al. [2016]. The gas temperature can drop to $\sim 10^{3.5-4}$ K with velocities of $\sim 700 - 1200$ km s^{-1}.

2.3.2 COOL GAS ACCELERATION FROM THE HOT WIND RAM PRESSURE

Several papers in which the evolution of molecular/atomic clouds interacting with hot stellar winds has been simulated, have concluded that it is quite possible that these clouds are destroyed by the wind due to hydrodynamic instabilities (e.g. Banda-Barragán et al. [2016] and Banda-Barragán et al. [2018]). The time-scale at which these instabilities grow and destroy the cloud is a multiple of the cloud crushing time $t_{cc} \simeq (r_c/v_w)(\rho_c/\rho_w)^{1/2}$ (see Heckman & Thompson [2017]), where, for a spherically symmetric cloud, r_c is the radius and ρ_c the density. In this scenario, the cold gas is unable to achieve high velocities before its evaporation. However, it is possible that the lifetime of an atomic/molecular gas cloud is significantly extended by the presence of magnetic fields (McCourt et al. [2015]) or thermal conduction (Brüggen & Scannapieco [2016]). Indeed, in the former case, it has been shown by Banda-Barragán et al. [2016] that the cold gas cloud can be accelerated up to $\sim 10\%$ of the hot wind speed in models with non-turbulent or subsonically turbulent clouds and up to $\sim 30\%$ in models with supersonically turbulent clouds.

2.3.3 ACCELERATION VIA RADIATION PRESSURE AND COSMIC RAY PRESSURE

The difficulty for an energy-driven wind to achieve large β values and reach high speeds at the same time, has led to the idealization of a momentum-driven wind model by Murray et al. [2005]. In this case the gas can acquire momentum from several sources such as, the radiation pressure given by the absorption and scattering of starlight by dust grains, or the pressure transferred to the gas by cosmic rays. In order to ensure that the radiation pressure is efficient, it is necessary that the medium is optically thick $\tau \geq 1$, i.e., it does not allow the radiation to escape. In this scenario the mass outflow rate can be written as (see Heckman & Thompson [2017]):

$$\dot{M}_{MD} \approx \left(\frac{SFR}{M_\odot \ \mathrm{yr}^{-1}} \right) \left(\frac{v_w}{300 \ \mathrm{km \ s}^{-1}} \right)^{-1} M_\odot \ \mathrm{yr}^{-1} \qquad (2.11)$$

and can quite easily reach speeds of ~ 600 km s^{-1} (see Thompson et al. [2015]).

2.4 Galactic Wind Simulations

As discussed in this section, there are several theories that can explain how it is possible to have high-speed clouds of cold gas. To understand which of the previous models best represents the reality, several authors developed simulations of galactic winds to find the way to address the issue. In the following section, some examples of galactic wind simulations, at different scales and resolutions, is reported.

a)   b)   c)
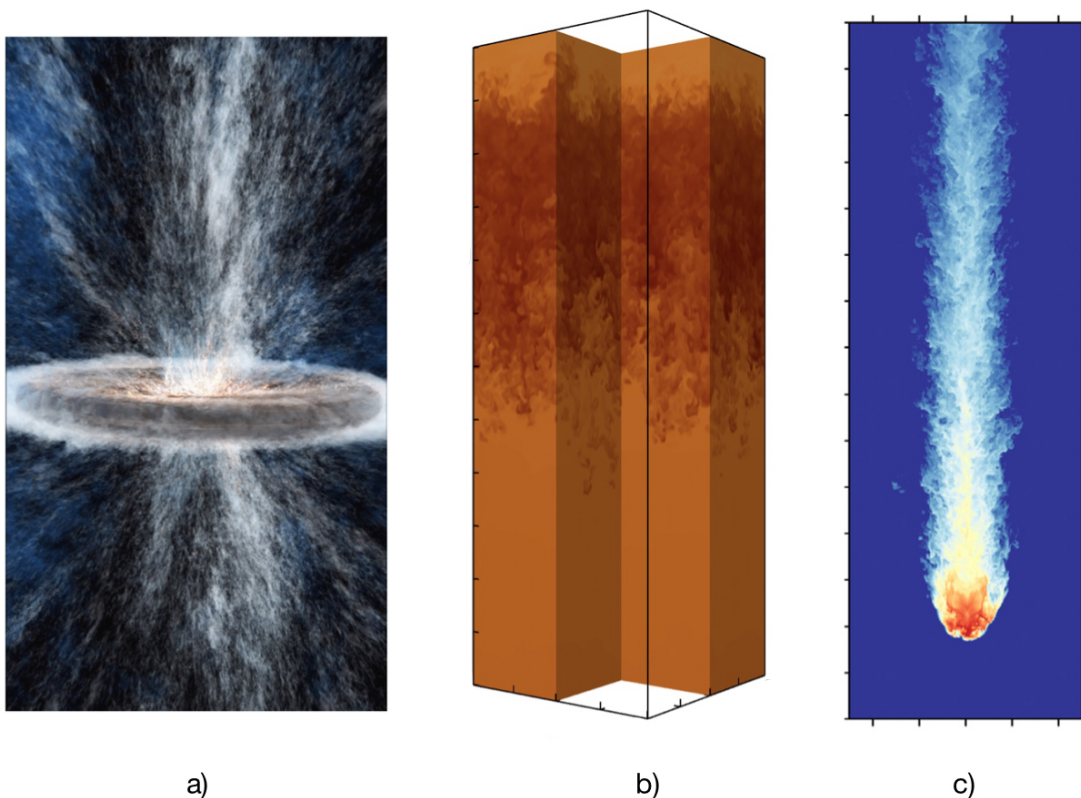
Figure 2.6: Galactic winds at different scales. Panel a) shows the density field rendering of a disc-wind simulation taken from Schneider et al. [2020]. In b) the gas number density in a shock-multicloud simulation taken from is shown Banda-Barragán et al. [2021]. Finally, in c) is plotted a wind-cloud simulation rendering taken from Banda-Barragán et al. [2019]

2.4.1   GALACTIC DISC-WIND MODELS

In simulations of this kind, researchers try to reproduce the evolution of a galactic wind on a galactic scale (see panel a) of FIG 2.6), by either capturing the whole outflow lobes (see Cooper et al. [2008], Schneider et al. [2018]) or vertical slices of it (Walch & Naab [2015], Kim & Ostriker [2018]). In the former case, they typically consider a disc galaxy with inhomogeneous density, within which the SNe explosion generates a galactic wind. The advantage of these simulations is that they offer the possibility to study wind launching in a self-consistent manner and also reproduce the bi-conical structure of the wind and also the filamentary structures observed for example in M82 (see Cooper et al. [2008] and also FIG 2.2). However, the resolution is not high enough to resolve individual atomic or molecular clouds and understand which processes may influence their evolution at the pc to sub-pc scales. On the other hand, in the latter case the full life cycle of cold clouds can be studied owing to the higher numerical resolutions of the SILCC and TIGRESS simulations. In Schneider et al. [2020], for example, the box has dimensions of $(L_x, L_y, L_z) = (10 \ \text{kpc}, 10 \ \text{kpc}, 20 \ \text{kpc})$ and a resolution of ~ 5 pc. In this study, it was possible to confirm the coexistence of hot and cool gas (with $T > 5 \times 10^5$ K and $T < 2 \times 10^4$ K, respectively) at all radii $(0 - 10 \ \text{pc})$. Furthermore, mixing between these two gas phases could be an efficient way to transfer momentum from hot to cool gas, making it reach speeds of $\sim 600 \ \text{km s}^{-1}$ at 8 kpc.

2.4.2   SHOCK-MULTICLOUD MODELS

In this type of simulations the evolution of multiple clouds embedded in a post-shock generated by a galactic wind is considered, as can be seen in FIG 2.6 (b). The domain of these simulations typically covers a few hundred pc, e.g in Banda-Barragán et al. [2020], 2021 the domain spans 100 pc $\times$500 pc $\times$100 pc and can reach.g., see Banda-Barragán et al. [2020], 2021. Although in these types of studies the overview of the bi-conical structure of the wind is not captured, they are extremely useful to study small-scale processes regulating the atomic/molecular clouds evolution such as magnetic fields and radiative cooling, while capturing at the same time the effects that multiple clouds have on each other and on the global outflow structure. In Alūzas et al. [2012], Alūzas et al. [2014], and Banda-Barragán et al. [2020], it is demonstrated that the evolution of these systems consists of 4 stages: 1) the division into reflected and refracted shocks once the initial shock gets in contact with the cold gas; 2) a compression phase of the cloud layer while forward shocks travel through it; 3) a re-acceleration phase of the shock that causes the cloud layer to expand; and 4) finally a mixing phase between the hot and cold gas phase, where shear instabilities stretch the clouds and generate turbulence. Thus, mixing processes and the generation of a turbulent outflow from systems of interacting clouds is adequately captured in this kind of simulations.

 These models also allow to isolate the effects of different density distributions in the

cold phase and also of radiative cooling. For instance, in Banda-Barragán et al. [2020], it was shown that in porous compressive cloud distributions, dense gas can survive but it acquires low momentum, while in compact solenoidal cloud distributions, dense gas does not survive. Similarly, radiative processes can greatly affect the life time of the dense medium. In fact, Banda-Barragán et al. [2021] showed that the ability of clouds to radiate energy allows dense gas to survive for longer. Once heated by the shock, the cloudlets cool down immediately. In this scenario, the dense gas follows a life cycle that seems to repeat several times during the simulation: cloudlets break up, mix, condense, fragment again, and some merge into filaments. The cold gas, rather than being accelerated, seems to precipitate and acquires momentum from the post-shock flow while the gas is in the mixed phase. In radiative models eventually, warm gas ($T \sim 10^4$ K) can reach velocities of $\sim 300 - 400$ km s^{-1} and cold gas $T \sim 10^2$ K speeds of $\sim 200 - 300$ km s^{-1} (see Banda-Barragán et al. [2021]). In the same simulation presented in Banda-Barragán et al. [2021] it was possible to find H I with density $N_{HI} = 10^{19} - 10^{21}$ cm^{-2}, velocity of $\simeq 200 - 300$ km s^{-1}, which travelled for $100 - 200$ pc; in agreement with the observations of McClure-Griffiths et al. [2013]. However, in shock-multicloud models, the resolution is not high enough to resolve the disruption of individual cloudlets via Kelvin-Helmholtz (KH) and Rayleigh-Taylor (RT) instabilities, which need to be studied by the next category of models.

2.4.3 WIND/SHOCK-CLOUD MODELS

Models investigating the interaction of a single cloud with a galactic wind allow us to analyse the hydrodynamic instabilities in the outer layers of the cloud, which are responsible for the destruction of the clouds. Furthermore, in these simulations we can see in detail how radiative processes, magnetic fields, turbulence (see Banda-Barragán et al. [2016], Banda-Barragán et al. [2018], and Banda-Barragán et al. [2019]), and thermal conduction (see Scannapieco & Brüggen [2015] and Brüggen & Scannapieco [2016]) can affect the evolution of wind-swept clouds, since resolutions of about 0.08 pc can be reached (for example in Banda-Barragán et al. [2019]). In FIG 2.6 (c) it is shown a representation of a single cloud interacting with a galactic wind, taken from Banda-Barragán et al. [2019]. Purely hydrodynamic models show that adiabatic clouds are destroyed by instabilities before travelling large distances, while radiative and thermally-conductive cloud models prove that the lifetimes of these clouds can be extended, but not sufficiently to be accelerated to the speeds at which they are observed (Scannapieco & Brüggen [2015] and Brüggen & Scannapieco [2016]). In these cases, the origin of cold gas at high velocities appears to be originated from the precipitation of the hot phase. Other important conclusions can be drawn from Banda-Barragán et al. [2018], where porosity and supersonic turbulence enhance cloud acceleration to $\sim 0.3 - 0.4$ of wind speed; while the magnetic fields protect clouds from ablation and causes Rayleigh-Taylor-driven sub-filamentation.

2.5 Specific objectives of this thesis

In order to get a more detailed picture of the multi-phase nature of galactic winds, it is necessary to find a way to compare simulations with observations. One option is through synthetic spectroscopy, obtained from (magneto)hydrodynamical models. In particular, understanding how simulated models, with different initial conditions, can produce different absorption spectra is crucial. An important goal of this thesis is to understand how some processes such as, magnetic stressed and radiative cooling can affect the shape of ion spectral lines, in order to confirm which processes are dominant in observed galactic wind systems.

The specific questions we aim to answer in this thesis include: what ions can we detect in the different evolutionary stages of clouds interacting with the galactic wind? What are the average abundances of individual ions in such interactions? How can the orientation of the magnetic field affect the ion column densities and the shape of their spectra? How can the usage of a different cooling floor in simulations that consider radiative cooling, affect cloud morphology and consequently ion spectra? To provide answers to these questions, we have created a tool able to produce remove column density maps and synthetic spectra of different ion species from simulations of change order, which also take into account a UV background consistent with the high star formation from which these systems typically evolve.

Chapter 3

Methods and Simulations

In this chapter we explain in detail how we conducted the wind-cloud and shock-multicloud model analyses. The chapter begins with an introduction of all the codes, softwares, and packages we used to create the PLUTO-Trident interface. After that, we describe the datasets for the wind-cloud and shock-multicloud simulations, including how they were implemented, initial and boundary conditions. Subsequently we define which diagnostics we employed for our analysis, with respective initial values reported in TABLE 3.1 and TABLE 3.2. Finally, the chapter concludes with the definition of dynamic time-scales and their inizial values. In this chapter we also include two examples of 2D-turbulence simulations (sub-sonic and super-sonic) that we have analyzed as a preliminary work for the subsequent study of medium-resolution wind-cloud and shock-multicloud models.

3.1 Software

3.1.1 PLUTO CODE v4.3

The PLUTO code is a software used for solving systems of conservation laws using finite difference or finite volume approaches based on Godunov-type schemes. It is mainly used to simulate the evolution of astrophysical systems such as Black Holes (BH) accretion, AGN jets, molecular clouds, galactic winds, stellar-driven winds, among others. In our project we analyze datasets describing the interaction of atomic clouds with galactic winds, akin to those observed in starburst galaxies. Given its flexibility and robustness, we employ PLUTO V4.3 code (Mignone et al. [2007]) to numerically solve the conservation equations of mass, momentum, and energy of ideal magneto-hydrodynamics. The code is written in C, however it also requires the installation of a version of Python > 2 as the interface for the setup of the initial conditions is written in Python.

3.1.2 PYTHON v3.6

We also use Python3, a high-level programming language, for the development of our project since it is very intuitive and has many libraries that can be adapted for the anal-

ysis of the PLUTO datasets such as `numpy, math, scipy, vtk`... The version we
used is 3.6 and the project was implemented in this programming language especially
because the main packages for spectra production, YT and Trident, are Python packages.
Moreover its versatility allowed us to develop scripts able to interface with the various
software packages. Some of these functions will be explained in more detail in section
4.1. Finally with the Python3 package `mathplotlib` we have produced the graphs and
animations of this thesis.

3.1.3   YT v3.6.0

YT (Turk et al. [2011]) is a Python toolkit for the analysis and visualization of volumetric
data. It works with fields, such as gas density and temperature. The fields can be read au-
tomatically from the library or can be implemented by the user with the respective units.
In our case the fields related to the gas that we defined in the dictionary (see section 4.1)
were: density in $\mathrm{g\,cm^{-3}}$, velocity in $\mathrm{cm\,s^{-1}}$, temperature in K, and gas metallicity in units
of $Z_\odot$. YT is the major dependency of Trident, in fact Trident uses the fields and some
functions of YT to make the chemical analysis of the object of study. Other functions that
were very useful for the development of the project were `yt.SlicePlot`, for the visual-
ization of how the fields are distributed within a section of the volume, `yt.PhasePlot`
for the creation of 2D histograms of temperature - density and `yt.ProjectionPlot`.
This last function, in combination with Trident, has been particularly useful in the vi-
sualization of how the various elements are distributed within projection of the evolving
atomic clouds. The version of YT we used is 3.6.0 and consequently the version of Trident
we downloaded is 1.2.3 as both are compatible with Python 3.6.

3.1.4   TRIDENT v1.2.3

The Trident package developed by Hummels et al. [2017], is a Python-based tool for post-
processing hydrodynamical simulations to produce synthetic absorption spectra. We
chose Trident for the project because it creates absorption-line spectra for any trajectory,
operates across the ultraviolet, optical, and infrared bands and generates column density
maps for any ion. Because of the close relationship of Trident to YT, many of the features
that Trident provides, such as the ability to post-process grid-based data sets to include
density fields for a desired ion, can be further used within the YT framework. This en-
ables users to make, for example, projections plots and slice plots of these ion fields and
also create phase plots. In order to create absorption lines for a given ion, it is necessary
that a fluid field representing the density of that ion be present for all elements sampled
by the `LightRay`. In our project we exploit the Trident sub-package `ion_balance` in
order to create a new field. This is possible since Trident defines the density of an ion i,
of an element X, as:

$$n_{X_i} = n_X f_{X_i} \tag{3.1}$$

where n_{X_i} is the total number density of the element and f_{X_i} is the ionization fraction of the ith ion. The function `ionbalance` computes n_X as:

$$n_X = n_H Z \left(\frac{n_X}{n_H} \right)_{\odot} \tag{3.2}$$

where Z is the metallicity, $(n_X/n_H)_{\odot}$ is the solar abundance by number and n_H is the total hydrogen number density, defined as:

$$n_H = \frac{\rho}{m_H} \tag{3.3}$$

In eq. 3.3, ρ is the total gas density and is the primordial H mass-fraction (adopted value = 0.76). Under the assumption of ionization equilibrium, the ionization fraction is a function of temperature, density, and the shape and intensity of the incident radiation field. In section 4.1, the main Trident functions we used for generating spectra are listed and described in more detail.

3.1.5   STARBURST99

Starburst99, by Vázquez & Leitherer [2017], is a software that provides sets of model predictions for spectrophotometric and related properties of galaxies with active star formation. We exploited the spectral energy distributions provided in the website in order to generate the UV background for the spectra production. In our case, we used existing runs from the Sb99 online database https://www.stsci.edu/science/starburst99/docs/table-index.html. The models in this database are presented in a homogeneous way for five metallicities between $Z = 0.040$ and 0.001 and three choices of the initial mass function. The age coverage is $10^6 - 10^9$ yr.

3.1.6   CLOUDY13

CLOUDY, by Ferland et al. [2013], is an open source plasma simulation code that is designed to simulate conditions in a non-equilibrium gas, and predict its metal composition given certain ranges of temperature and densities. The code incorporates physical processes to simulate the ionization, level populations, molecular state, and thermal state, over all extremes of density and temperature. CLOUDY can be applied to such diverse regions as the corona of a star, the intergalactic medium, or the accretion disk near the supermassive black hole in a luminous quasar. The diversity of problems it can address is a testimonial to the importance of treating the atomic physics at an elementary level. For this project we use the `CIAOLoop` tool provided in the `cloudy_cooling_tools` website, developed and maintained by Smith et al. [2017]. `CIAOLoop` is a perl- and python-based wrapping code capable of running and collating grids of CLOUDY models in parallel. We exploited its modules to produce ion tables in order to generate a starburst UV background.

3.2   Simulation datasets

In this section we describe how the wind-cloud, shock-multicloud, and 2D-turbulence simulations are implemented. The description of wind-cloud simulations set-up is shown also in **??**, but our dataset includes also cooling and heating functions in order to reproduce radiative feedback. The description of the shock-multicloud simulation set-up is described in **??**; we mention here the highlights.

3.2.1   PRODUCTION WIND-CLOUD SIMULATIONS

In this project, the study of the evolution of atomic clouds interacting with galactic winds was possible via simulations performed using the PLUTO v3.4 code. The setup we used is based on the models presented in Banda-Barragán et al. [2016]). The ideal equations of magnetohydrodynamics (MHD) were solved within a 3D Cartesian coordinate system X_1, X_2, X_3. The MHD equations of mass, momentum, energy conservation, and magnetic induction are:

$$\frac{\partial \rho}{\partial t} + \bigtriangledown \cdot [\rho \mathbf{v}] = 0, \tag{3.4}$$

$$\frac{\partial [\rho \mathbf{v}]}{\partial t} + \bigtriangledown \cdot [\rho \mathbf{v}\mathbf{v} - \mathbf{B}\mathbf{B} + \mathbf{I}P] = 0, \tag{3.5}$$

$$\frac{\partial E}{\partial t} + \bigtriangledown \cdot [(E + P)\, \mathbf{v} - \mathbf{B}(\mathbf{v} \cdot \mathbf{B})] = \Gamma - \Lambda, \tag{3.6}$$

$$\frac{\partial \mathbf{B}}{\partial t} - \bigtriangledown \times (\mathbf{v} \times \mathbf{B}) = 0 \tag{3.7}$$

where ρ is the mass density, $\mathbf{v}$ is the velocity, $\mathbf{B}$ is the magnetic field, $P = P_{th} + P_{mag}$ is the total pressure given by the sum of thermal and magnetic pressure ($P_{th} = (\gamma - 1)\rho\epsilon$, with $\gamma = 5/3$ for these simulations and $P_{mag} = \frac{1}{2}|\mathbf{B}|^2$), $E = \rho\epsilon + \frac{1}{2}\rho\mathbf{v}^2 + \frac{1}{2}|\mathbf{B}|^2$ is the total energy density, ϵ is the specific internal energy, Γ is the volumetric heating rate, and Λ is the volumetric cooling rate. Additional advection equations were included of the form:

$$\frac{\partial [\rho C]}{\partial t} + \bigtriangledown \cdot [\rho C \mathbf{v}] = 0 \tag{3.8}$$

where C represents the tracer used to track the evolution of the gas initially contained entirely in the cloud. Initially $C = 1$ for the whole cloud and $C = 0$ everywhere else.
To solve this system of hyperbolic conservation laws the PLUTO code was configured to use `HLLD` approximate Riemann solver of Miyoshi & Kusano [2005] jointly with the divergence cleaning algorithm by Dedner et al. [2002] (2005, 2008) to preserve the solenoidal condition, $\nabla \cdot \mathbf{B} = 0$. In order to achieve the stability, the Courant-Friedrichs-Lewy (CFL) number is 0.3.

Table 3.1: Initial conditions for our wind-cloud models. Column 1 indicates the model name. Column 2 indicates the number of cells of the computational domain. Column 3 is the adiabatic index, and Column 4 the initial density contrast between the centre of the cloud and the ambient medium. Column 5 indicates the temperature of the cooling floor. Columns 6 and 7 indicate the initial orientation of the magnetic field and its intensity.

(1) Model	(2) Number of cells	(3) γ	(4) χ	(5) Cooling floor [K]	(6) Magnetic Field	(7) B [μ G]
RWC-R32-AL-F1	$(384 \times 768 \times 384)$	5/3	10^3	50	Aligned	0.17
RWC-R32-TR-F1	$(384 \times 768 \times 384)$	5/3	10^3	50	Transverse	0.17
RWC-R32-AL-F2	$(384 \times 768 \times 384)$	5/3	10^3	10^4	Aligned	0.17
RWC-R32-TR-F2	$(384 \times 768 \times 384)$	5/3	10^3	10^4	Transverse	0.17

3.2.1.1 Initial and Boundary Conditions
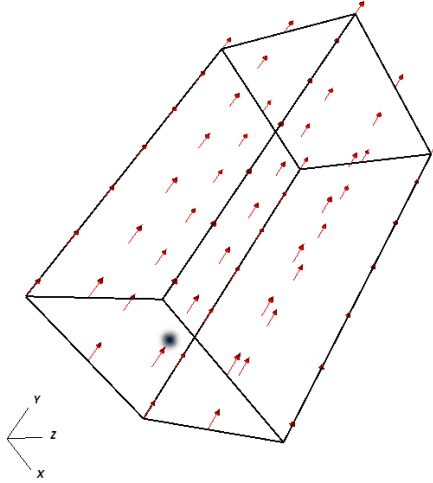
Figure 3.1: 3D set-up of our wind-cloud simulations, which features a spherical cloud with a density profile shaded in blue and arrows representing a uniform velocity field of the ambient galactic wind.

Our simulations involve a two-phase ISM composed of a single spherical cloud surrounded by a hot wind with a uniform velocity distribution (see TABLE 3.1). The simulation domain consists of a rectangular prism with diode boundary conditions on seven sides and an inflow boundary condition in the remaining side located in the lower left part of the volume (see FIGURE 3.1). The injection zone guarantees a continuous wind flow onto the domain.

Our simulations, the cloud is located at the origin of the coordinate system $(0, 0, 0)$ and its density distribution is:

$$\rho(r) = \rho_w + \frac{(\rho_c + \rho_w)}{1 + \left(\frac{r}{r_{core}}\right)^N} \tag{3.9}$$

where $\rho_c = 100$ is the density at the centre of the cloud, $\rho_w = 0.1$ is the density of the wind, $r_{core} = 0.5$ is the radius of the cloud core, and N is the steepness of the curve describing the density gradient (see FIGURE 3.2). The profile in eq 3.9 extends to infinity, so a value of $N = 10$ is taken and the density function is truncated at $r_{cut} = 1.58$, at which $\rho(r_{cut}) = 1.01\rho_w$. This type of density gradient is added to resemble the core and envelope of ISM clouds, in which a very dense H_2 core is surrounded by an envelope of $H\,I$ and an even more outer, rarefied shell of photo-ionized $H\,II$.
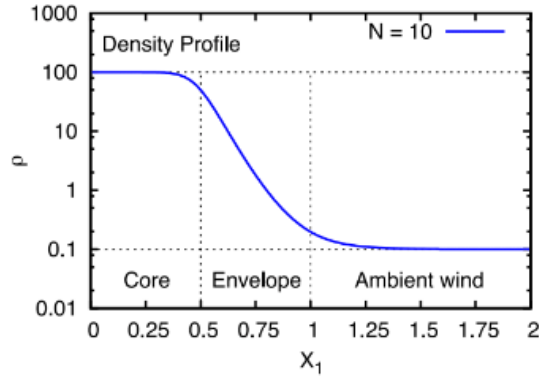
Figure 3.2: The radial density profile with $N = 10$, from Banda-Barragán et al. [2016]

All models analysed include magnetic fields and can be divided into two types:

- RWC-R32-AL where the magnetic field is aligned with the wind direction, i.e.,

$$\mathbf{B} = \mathbf{B_{Al}} = \mathbf{B_2} = \sqrt{\frac{2P_{th}}{\beta}}\hat{\mathbf{e}}_2 \tag{3.10}$$

- RWC-R32-TR simulations with a transverse magnetic field, perpendicular to the wind direction, i.e.,

$$\mathbf{B} = \mathbf{B_{Tr}} = \mathbf{B_1} = \sqrt{\frac{2P_{th}}{\beta}}\hat{\mathbf{e}}_1. \tag{3.11}$$

Both fields have the same initial strength ($\beta = 100$). In all MHD simulations, the magnetic field was initialised by using the magnetic vector potential $\mathbf{A}$, where $\mathbf{B} = \nabla \times \mathbf{A}$, also to ensure the field has zero divergence.

3.2.1.2   Cooling and heating function

Figure 3.3: Temperature-dependent cooling and heating functions implemented in our simulations, taken from Banda-Barragán et al. [2021]. The colored lines represent the trends at different numerical densities.
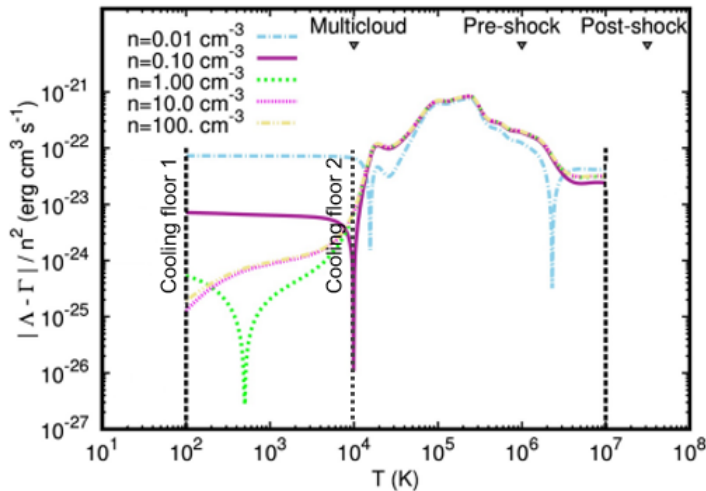
A tabulated cooling function $\widetilde{\Lambda}$ including radiative cooling from atomic species in a temperature range from 10 K to 10^9 K was used in our simulations (see Teşileanu et al. [2008]). In each of them cooling is turned off for $T > 10^7$ K. Moreover, the simulations we have analysed have two different types of cooling floor, some at 50 K (marked with F1) while others at 10^4 K (marked with F2). This means that at temperatures below the cooling floor threshold, the gas is no longer able to cool. In section 4.2 we will explain in more detail how the two different set-ups significantly affect the evolution of the cloud and how this also impacts on the spectra that are generated. The cooling rates are precalculated with CLOUDY assuming the gas has solar metallicity, is optically thin, and is composed only of atomic species. Tabulated values are expressed in erg cm^3 s^{-1}, so $\Lambda = [\rho/(\mu m_u)]^2 \, \widetilde{\Lambda} = n^2 \widetilde{\Lambda}$. A density-weighted heating function is also considered, it is calculated from the cooling rates so that at the beginning of the simulation, the gas with density $n = 0.1 \text{cm}^{-3}$ has an equilibrium temperature of $T = 10^4$ K. The heating function $\widetilde{\Gamma}$ is given by the following expression: $\Gamma = [\rho/(\mu m_u)] \, \widetilde{\Gamma} = n\widetilde{\Gamma}$. The thermal equilibrium equation is $n\widetilde{\Lambda} = \widetilde{\Gamma}$ and the cooling function $|\Gamma - \Lambda|/n^2$ depends on both temperature and density. This means that the heating counteracts the cooling but it cannot fully stop very dense gas from condensing to $\sim 10^2$ K temperatures, since the cooling rates scale with n^2 while the heating rates scale only with n. Therefore, if the gas becomes sufficiently dense, it will cool down near the cooling floor temperature.

Table 3.2: Initial conditions for our shock-multicloud models. Column 1 indicates the
model name. Column 2 indicates the number of cells of the computational
domain. Column 3 is the adiabatic index, and Column 4 the initial density
contrast between the centre of the cloud and the ambient medium. Column 5
indicates the temperature of the cooling floor.

(1)	(2)	(3)	(4)	(5)
Model	**Number of cells**	γ	χ	**Cooling floor [K]**
sole-k8-M10-rad-bl2	$(128 \times 1920 \times 128)$	$5/3$	10^2	50

3.2.2   PRODUCTION SHOCK-MULTICLOUD SIMULATIONS

The last case we have studied consists of a shock-multicloud model in which the evo-
lution of a distribution of multiple atomic clouds interacting with a stellar-driven wind
shock is studied. In this simulation (described also in Banda-Barragán et al. [2021]) as
model sole-k8-M10-rad, but in a larger computational domain, dynamic instabilities, tur-
bulence, radiative cooling and heating have been taken into account in order to study the
complex relationship between clouds and the shock. As in the case of individual atomic
clouds, the simulation was run with PLUTO v3.4 in order to solve the conservation equa-
tions of mass, momentum and energy, without magnetic fields and gravity terms:

$$\frac{\partial \rho}{\partial t} + \bigtriangledown \cdot [\rho \mathbf{v}] = 0 \tag{3.12}$$

$$\frac{\partial \rho \mathbf{v}}{\partial t} + \bigtriangledown \cdot [\rho \mathbf{v}\mathbf{v} + \mathbf{I}P] = 0 \tag{3.13}$$

$$\frac{\partial E}{\partial t} + \bigtriangledown \cdot [(E + P)\mathbf{v}] = \Gamma - \Lambda \tag{3.14}$$

where all the terms are also the ones defined in the single cloud model. Again, an addi-
tional advection equation 3.8 was solved in order to track the gas initially located within
the multicloud system; still with $C = 1$ for the gas belonging to the multicloud layer and
$C_\alpha = 0$ outside.

3.2.2.1   Initial and Boundary Conditions

The computational domain consists of a 3D prism of size $L \times 15L \times L$ which coincides
with a physical domain of 100 $pc \times$ 1500 $pc \times$ 100 pc. This volume is three times larger
than in Banda-Barragán et al. [2021] and therefore it is possible to study the evolution
of the cloud layer at much large distances and for longer time-scales with respect to the
point : at which the shock is initialised. The number of cells in the grid is $128 \times 1920 \times 128$,
so the numerical resolution is about 0.78 pc. The boundary conditions are periodic along
X and Z, inflow on the bottom Y side of the domain and outflow on the top Y side of
the domain. Details regarding the initial conditions for the shock-multicloud model are
shown in TABLE 3.2.

Table 3.3: Initial properties for the 2D-turbulence models. Column 1 indicates the type of turbulence. Columns 2, 3 and 4 are the normalization factors for density, velocity and length. Column 5 and 6 indicate the initial $\mathcal{M}_{rms}$ and the initial sound speed for an isothermal gas, respectively. Column 7 indicates mean temperature of the gas.

(1)	(2)	(3)	(4)	(5)	(6)	(7)
Model	ρ_0	v_0	L_0	$\mathcal{M}_{rms}$	c_{iso}	T
	[g cm^{-3}]	[cm s^{-1}]	[cm]			[K]
SUB-sonic	1.66×10^{-24}	10^6	3.1×10^{18}	~ 0.9	1	$\sim 10^4$
SUPER-sonic	1.66×10^{-22}	10^5	3.1×10^{18}	~ 2	0.6	$\sim 10^2$

3.2.3 CODE DEVELOPMENT SIMULATIONS (2D TURBULENCE)

In addition to the main production simulations, which are the core of our analysis, we also analysed additional 2D models of turbulent flows in order to develop and test the python functions we used for the main production models. Our code-development simulations include 2D turbulence simulation datasets performed using the PLUTO v3.4 code [Mignone et al., 2007] in order to describe the behaviour of the molecular and atomic phase of the interstellar medium (ISM). These simulations helped us build and test a data analysis framework whose results can be readily compared to well-established literature on ISM turbulence. These models aim to emulate the evolution in ~ 2 Myr of an isothermal gas with a uniform density distribution. The gas is contained in a 2^2 pc^2 domain with periodic boundary conditions. At the beginning the medium is uniform, at rest, and it is uniformly magnetised, with the magnetic field inclined by $45°$ with respect to both axes.

In this simulation, solenoidally-driven turbulence is introduced through the application of a statistically isotropic stochastic force field that generates large-scale random flows. The injection of this mechanical force causes adjacent gas layers to move at different speeds, creating instabilities that evolve into eddies and filamentary structures [Elmegreen & Scalo, 2004]. In this scenario, if turbulence is not stirred up, it will always be dissipated. In order to still have shear flows and rotation in the gas, a continuous injection of energy is necessary, but this also means that at some point the rate at which energy is input equals the dissipation rate. Thus, the system reaches a steady state where the average gas properties do not change and the turbulence can be studied in detail.

In this thesis we show the example of sub-sonic and super-sonic turbulence in order to examine how turbulence evolves in cold ($T \sim 10^2$ K) and warm ($T \sim 10^2$ K) gas. The TABLE 3.3 shows the normalization factors and some initial properties of the two simulations.

3.3   Simulation diagnostics

3.3.1   CODE DEVELOPMENT FOR THE COMPUTATION OF INTEGRATED QUANTITIES

The dataset produced by the PLUTO simulations provide for each time step the following data fields: gas density ρ, the x- and y-component of the velocity, the magnetic field. From these quantities it was possible to derive the total mass of the gas cloud by integrating the density of each cell multiplied by the volume of the cell itself,

$$M = \int_V \rho \; dxdydz \tag{3.15}$$

assuming $dz = dy = dx$. To obtain a more realistic value I then adopted a cloud depth of 2 pc and then, averaging over time. In order to make the graphs in FIG 3.4, the following formulas were used to calculate v_{rms} and $\mathcal{M}_{\mathrm{rms}}$:

$$v_{\mathrm{rms}} = \sqrt{(v_x^2 + v_y^2)} \tag{3.16}$$

$$\mathcal{M}_{\mathrm{rms}} = \frac{v_{rms}}{c_{s,iso}} \tag{3.17}$$

where $c_{s,iso}$ is the sound speed for an isothermal gas and we considered it $= 1$ in code units for the sub-sonic case, and $= 0.6$ for the super-sonic case. For a better understanding of how long it takes the gas to reach steady state it is necessary to define an auto-correlation time scale identified as the eddy turn-over time.

$$t_{to} = \frac{L_0}{v_{\mathrm{rms}}}. \tag{3.18}$$

Finally, the plasma beta parameter, which relates thermal and magnetic pressures, β was also calculated as follows:

$$\beta = \frac{P_{th}}{P_{mag}} \tag{3.19}$$

where the thermal pressure is equal to $\rho c_{s,iso}^2$ and the magnetic pressure is $\frac{1}{2}|B|^2$. The table below shows the values found in both cases.

In FIGURE 3.4 are shown how density, standard deviation of density, velocity rms and Mach number rms evolve over time in the subsonic case. All variables reach a plateau with very small fluctuations after less than 0.1 Myrs indicating the system is in steady state. Normally, in a cold molecular cloud, $\mathcal{M}_{\mathrm{rms}} \geq 1$ should be observed, but in this simulation, as can be seen in the bottom right graph of FIGURE 3.4, $\mathcal{M}_{\mathrm{rms}}$ is around 0.9; this means that the gas is in a transitory phase between the molecular and neutral atomic states. Initially, the gas is uniformly distributed and uniformly magnetised and then evolves under the influence of the stirring components of the force field. Bulk motions

also seem to be triggered during the simulation, confirmed by taking the average of the x- and y-components of the velocity, which show a non-zero value (see FIGURE 3.5). At the final instant of the simulation, the gas and the magnetic filed are distributed in filaments. From the VisIt (Childs et al. [2012]) representation, one can clearly see the formation of eddies as expected for solenoidal motions.
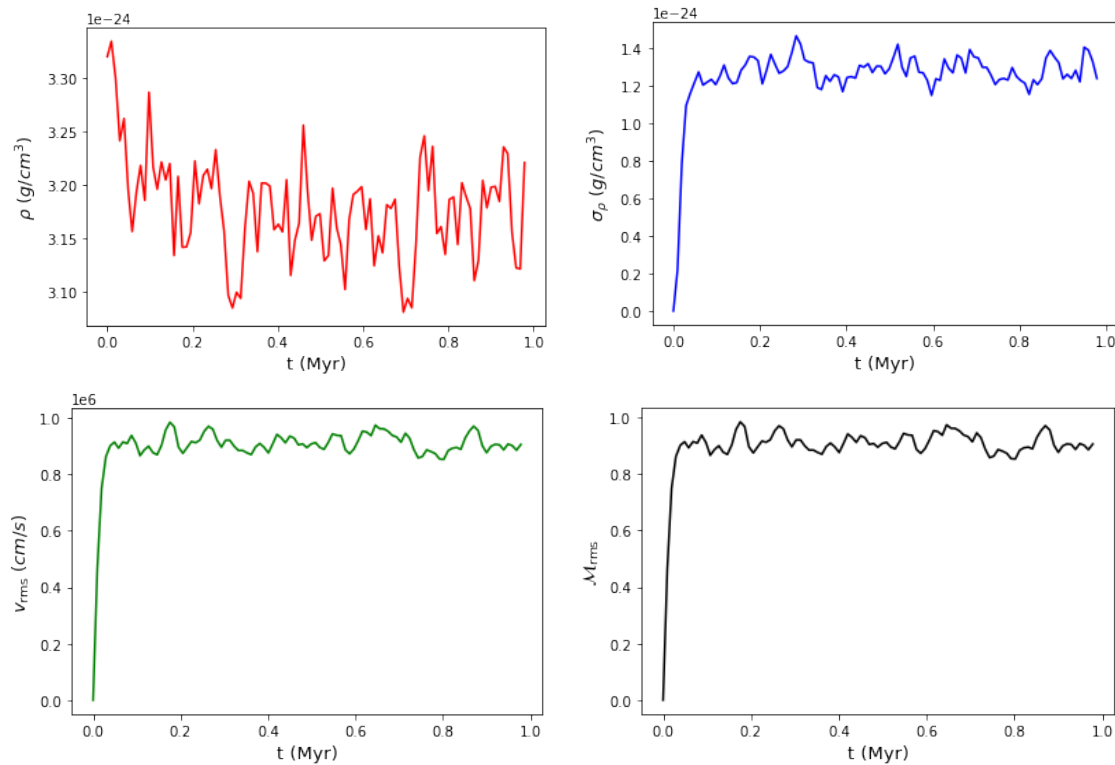

Figure 3.4: Temporal evolution of the gas cloud with subsonic turbulence. The top left panel represents the mean density, on the top right the standard deviation of the density is shown, the bottom left plot is the rms of the velocity and the bottom right plot the rms of the Mach number.

For the supersonic case, it has been found $\mathcal{M}_{\mathrm{rms}} = 2.28$ and $\beta \sim 0.53$, indicating that in this case the magnetic field is stronger owing to the extra compression. FIGURE 3.6 shows the time evolution of the density in red, the standard deviation of the density in blue, the rms of the speed in green and the Mach number in black. As can be seen, the system takes more time to reach steady state and this result is in agreement with $T_{to} \sim 0.36$ *Myr*, slower than the subsonic case.

In this supersonic simulation, the B ~ 9.13 μG and $v_{\mathrm{rms}} \sim 1.37$ km/s seem to be in fairly good agreement with those obtained from Larson and Crutcher's empirical laws.
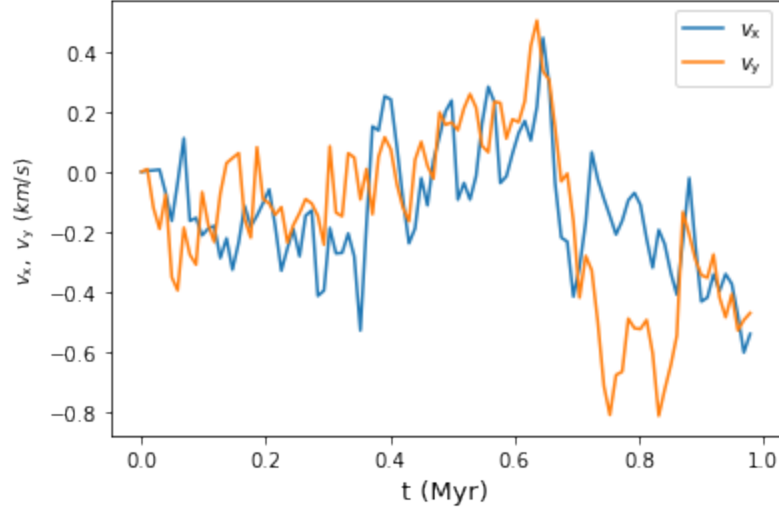
Figure 3.5: Time evolution of the x- and y- velocity components, in blue and orange respectively. Both values deviate from zero, indicating the presence of bulk motions.

Larson's size-dispersion law [Larson, 1981]

$$v_{\rm rms}\ ({\rm km/s}) = 1.1 \left(\frac{L}{1\ {\rm pc}}\right)^{0.38} \simeq 1.43\ {\rm km/s} \tag{3.20}$$

Crutcher's magnetic field - number density law [Crutcher et al., 2010]

$$B_{\rm max} \sim 10\ \mu{\rm G} \left(\frac{n}{300\ {\rm cm}^{-3}}\right)^{0.67} \simeq 7.59\ \mu{\rm G} \tag{3.21}$$

The comparison with the two empirical relations was not possible in the previous case because the cloud was subsonic and the medium too diffuse. For both subsonic and supersonic turbulence simulations, the PDF follows a lognormal distribution as shown in the FIGURE 3.7. Both functions have mean values around 1, however in the subsonic simulation (blue histogram) $\sigma_{\rho,sub} = 0.39$ while $\sigma_{\rho,sup} = 0.71$ (orange). This result is in agreement with the relation:

$$\frac{\sigma_\rho}{\rho} = b\mathcal{M}_{\rm rms} \tag{3.22}$$

which shows that the standard deviation of the PDF grows linearly with $\mathcal{M}_{\rm rms}$. The values of b obtained are $b_{sub} = 0.43$ and $b_{sup} = 0.34$, both in agreement with the results from Federrath et al. [2008] $b = 0.43 \pm 0.10$ and are consistent with solenoidal rather than compressive forcing.

Given all the analysis presented above and the match to the literature on turbulence, we can confidently use our functions to analyse any kind of PLUTO data via small adaptations in the code.
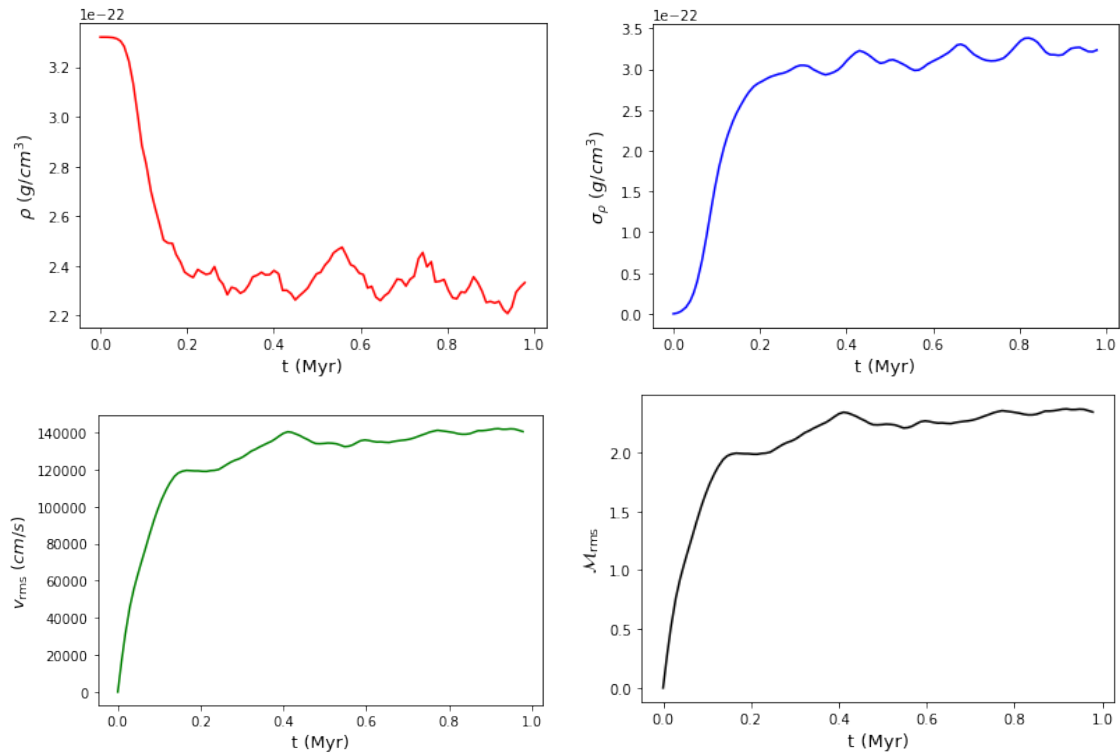
Figure 3.6: Temporal evolution of the gas cloud with supersonic turbulence. The top left panel represents the mean density, on the top right the standard deviation of the density is shown, the bottom left plot is the rms of the velocity and the bottom right plot the rms of the Mach number.

Figure 3.7: PDF: The two functions represent the PDFs of the subsonic simulation in blue and supersonic in orange, both are normalised to their respective mean values of ρ.

3.3.2   DATA ANALYSIS OF WIND-CLOUD AND SHOCK-MULTICLOUD MOD-ELS

3.3.2.1   *Analysis diagnostics*

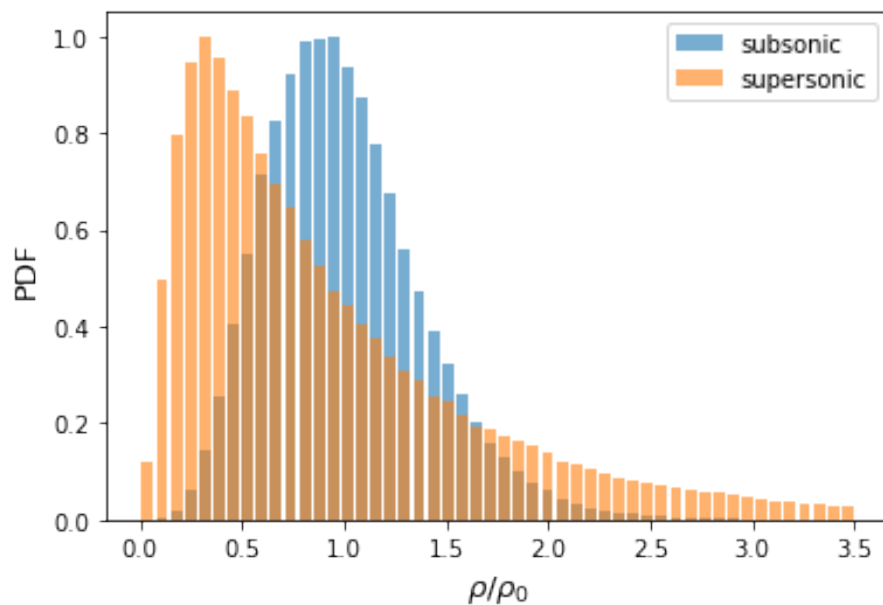To help us understand the evolution of both wind-cloud models and shock-multicloud models, we define several general diagnostic quantities in this section (see TABLE 3.4). Following the convention found in the literature [Banda-Barragán et al., 2016], I define the mass-weighted volume average of the variable $\mathcal{G}$ by

$$\langle \mathcal{G}_\alpha \rangle = \frac{\int \mathcal{G}\rho\,\mathcal{C}_\alpha \mathrm{dV}}{\rho\,\mathcal{C}_\alpha \mathrm{dV}} \tag{3.23}$$

denoted by angle brackets. In eq 3.23 V is the volume and $\mathcal{C}_\alpha$ is the tracer of the cloud. We remind the reader that $\mathcal{C}_\alpha = 1$ for the cloud and $\mathcal{C}_\alpha = 0$ everywhere else. From this equation it is possible to define the averaged cloud extension along one axes as $\langle X_{j,\alpha} \rangle$ with $j = 1, 2, 3$; and its rms along each axis $\langle X_{j,\alpha}^2 \rangle$. From this two quantities we computed the effective radii along each axis in order to study the evolution of the cloud shape with time:

$$\iota_{j,\alpha} = \left[5 \left(\langle X_{j,\alpha}^2 \rangle - \langle X_{j,\alpha} \rangle^2 \right) \right]^{1/2}. \tag{3.24}$$

The quantities related to the cloud are denoted by the subscript "cl" and some of them are ρ_{cl} (density), n_{cl} (number density) and M_{cl} (mass), calculated as follows:

$$\rho_{\mathrm{cl}} = \rho\,\mathcal{C}_\alpha \tag{3.25}$$

$$n_{\mathrm{cl}} = \frac{\rho_{cl}}{\mu m} \tag{3.26}$$

$$M_{\mathrm{cl}} = \int_V \rho_{cl}\,\mathrm{d}x\mathrm{d}y\mathrm{d}z \tag{3.27}$$

We also measured the degree of mixing between cloud and wind (see Xu & Stone [1995]):

$$f_{\mathrm{mix}} = \frac{\int \mathcal{C}_\alpha^* \mathrm{dV}}{M_{\alpha,0}} \tag{3.28}$$

with $0.01 < \mathcal{C}_\alpha^* < 0.99$. In both 3D simulations. To complete the thermodynamic study of the cloud, its temperature was also calculated:

$$T_{\mathrm{cl}} = \frac{P_{\mathrm{cl}}}{n_{\mathrm{cl}}\,k_{\mathrm{B}}} = \frac{P_{\mathrm{cl}}\,\mu m}{\rho_{\mathrm{cl}}\,k_{\mathrm{B}}} \tag{3.29}$$

In order to study quantities projected on the Plane of the Sky, we also measured the cloud column density both edge-on and down-the-barrel:

Table 3.4: Initial diagnostics values for wind-cloud and shock-multicloud models. Column 1 indicates the model name. Columns 2, 3 and 4 are the normalization factors for density, velocity and length. Column 5 and 6 indicate the initial Mach number and velocity of the wind in the wind-cloud models and for the shock in the shock-multicloud one. Column 7 indicates the initial temperature of the wind and the shock. Column 8 indicates the temperature at the centre of the cloud in the wind-cloud models and the mean initial temperature of the multicloud layer in sole-k8-M10-rad-bl2.

(1) Model	(2) ρ_0 [g cm^{-3}]	(3) v_0 [cm s^{-1}]	(4) L_0 [cm]	(5) $\mathcal{M}_{w,sh}$	(6) $v_{w,sh}$ [km s^{-1}]	(7) $T_{w,sh}$ [K]	(8) $T_{cl,multicl}$ [K]
RWC-R32-AL-F1	1.115×10^{-26}	10^7	3.1×10^{19}	4	516	8×10^5	8×10^2
RWC-R32-TR-F1	1.115×10^{-26}	10^7	3.1×10^{19}	4	516	8×10^5	8×10^2
RWC-R32-AL-F2	1.115×10^{-26}	10^7	3.1×10^{19}	4	516	8×10^5	8×10^2
RWC-R32-TR-F2	1.115×10^{-26}	10^7	3.1×10^{19}	4	516	8×10^5	8×10^2
sole-k8-M10-rad-bl2	1.115×10^{-25}	1.44×10^7	3.1×10^{19}	10	1440	3×10^7	10^4

$$N_{\text{cl, eo}} = \int N_z \, \mathcal{C}_\alpha \, \mathrm{d}z \qquad (3.30)$$

$$N_{\text{cl, dtb}} = \int N_y \, \mathcal{C}_\alpha \, \mathrm{d}y \qquad (3.31)$$

The other diagnostics related to galactic wind are the wind sound speed and wind Mach number, calculated in the following way:

$$c_{wind} = \sqrt{\gamma \frac{P}{\rho_{wind}}} \qquad (3.32)$$

$$\mathcal{M}_{wind} = \frac{v_{wind}}{c_{wind}} \qquad (3.33)$$

3.3.2.2 *Reference time-scales*

The relevant time-scales in our simulations are (see 3.5):

- The cloud-crushing time (see Jones et al. [1994] and Jones et al. [1996]):

$$t_{cc} = \frac{2r_{cl}}{v_{sh}} = \left(\frac{\rho_{cl}}{\rho_w}\right)^{\frac{1}{2}} \frac{2r_{cl}}{\mathcal{M}_w c_w} = \chi^{\frac{1}{2}} \frac{2r_{cl}}{\mathcal{M}_w c_w}. \qquad (3.34)$$

  where v_s is the speed the shock is propagates across the cloud. It represents the time it takes for the internal shock transmitted by the wind after the initial contact to cross the cloud.

- The wind-passage time Fragile et al. [2005]:

$$t_{wp} = \frac{2r_{cl}}{v_w} = \frac{1}{\chi^{\frac{1}{2}}}.$$ (3.35)

  It is the time taken by the wind to envelope the cloud.

- The shear-driven Kelvin-Helmholtz (KH) instability growth time Chandrasekhar [1961]:

$$t_{KH} \approx \frac{r_{cl}\chi^{\frac{1}{2}}}{2\pi v_{sh}} = \frac{t_{cc}}{2\pi}.$$ (3.36)

- The acceleration-driven Rayleigh-Taylor (RT) instability growth time Chandrasekhar [1961]:

$$t_{RT} \approx \left[\frac{r_{cl}}{2\pi(a_{eff})}\right]^{\frac{1}{2}} \approx \left[\frac{r_{cl}^2\chi}{0.8\pi\, v_{sh}^2}\right]^{\frac{1}{2}} = \frac{t_{cc}}{(0.8\pi)^{\frac{1}{2}}}.$$ (3.37)

  Where $a_{eff} \approx 0.4v_{sh}^2/(\chi r_{cl})$ is the effective cloud acceleration (see Banda-Barragán et al. [2019]). Both t_{KH} and t_{RT} correspond to a incompressible regime, so both quantities should be considered as indicative values for the compressible models reported in this thesis.

- The free-fall time:

$$t_{ff} = \left(\frac{2r_{cl}^3}{G\, m_{cl}}\right)^{\frac{1}{2}}.$$ (3.38)

  It represents the time it would take for the cloud to collapse on itself under the effect of the gravity force.

- An important time-scale associated with radiative processes is the cloud cooling time (Banda-Barragán et al. [2021]):

$$t_{cool,cl} = \frac{\frac{3}{2}n_{cl}k_B\langle T_{cl}\rangle}{n_{cl}^2\tilde{\Lambda}_{\langle T_{cl}\rangle}},$$ (3.39)

  where $\tilde{\Lambda}_{\langle T_{cl}\rangle} = 2.158000 \cdot 10^{-24}$ erg cm^3 s^{-1} is the equilibrium cooling function evaluated at $\langle T_{cl}\rangle$ and n_{cl}.

Table 3.5: Initial time-scales in wind-cloud and shock-multicloud models. Column 1 indicates the name of the model. Columns 2, 3, 4, 5, and 6 indicate the values of the initial time-scales defined in this section in Myr.

(1)	(2)	(3)	(4)	(5)	(6)
Model	t_{cc}	t_{wp}	t_{KH}	t_{RT}	t_{cool}
	[Myr]	[Myr]	[Myr]	[Myr]	[Myr]
RWC-R32-AL-F1	0.6	0.7	0.1	0.4	0.02
RWC-R32-TR-F1	0.6	0.7	0.1	0.4	0.02
RWC-R32-AL-F2	0.6	0.7	0.1	0.4	0.02
RWC-R32-TR-F2	0.6	0.7	0.1	0.4	0.02
sole-k8-M10-rad-bl2	0.05	0.2	0.009	0.036	0.008

Chapter 4

Results
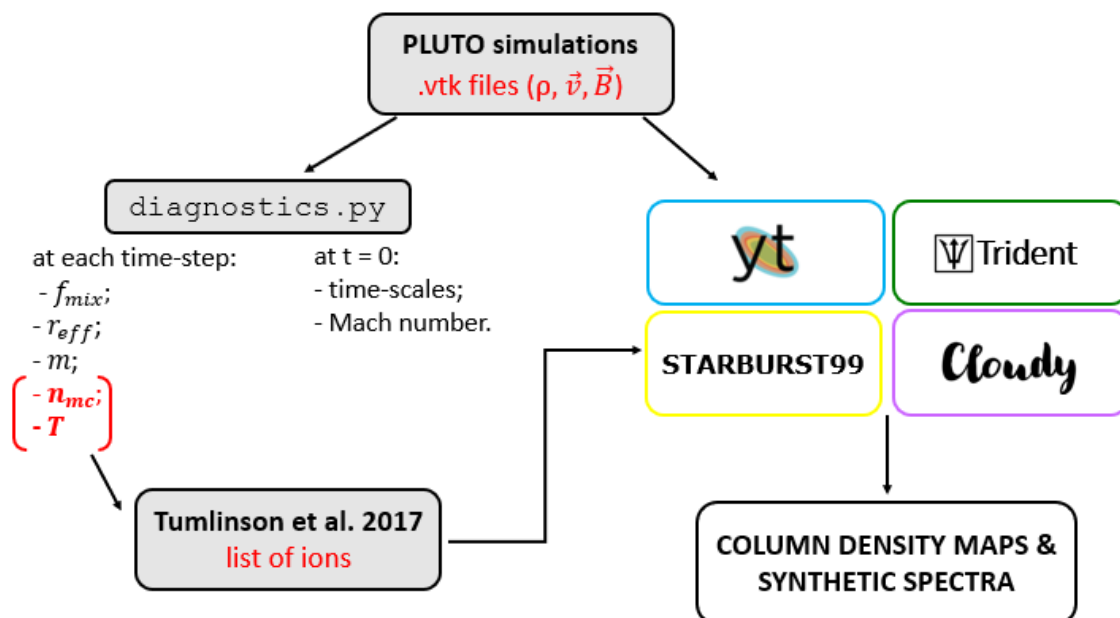
4.1 A python framework to link PLUTO and TRIDENT

Figure 4.1: Flow chart summarising the main components of the framework that produces column density maps and synthetic spectra from PLUTO simulations. The starting point is the datasets provided by PLUTO, which we initially analysed using the script diagnostics.py in order to find which ions would be included in the synthetic spectra. The right-hand side of the diagram shows which software we used to produce the ion density maps and spectra.

In this section we discuss the implementation of a framework able to produce synthetic spectra and column density maps of atomic/molecular clouds interacting with galactic winds from simulation datasets. The flowchart shown in FIGURE 4.1 provides a summary of the implementation of the project, and in the following paragraphs we will explain in more detail how each component of the code and the various software packages interact with each other. The first part of the framework involves reading the `.vtk` files

produced by the PLUTO simulations. Then, we analyse the data in order to study the dynamics of the system. For this purpose, we have created a script in Python called `diagnostics.py` that receives as input the `.vtk` files with density, velocity, magnetic field of each cell and normalisation factors in c.g.s units (ρ_0, v_0, L_0, μ and γ). Our analysis in Python provides two types of outputs: a set of diagnostics calculated at $t = 0$ such as: magnetic field, initial temperature, Mach number and time-scales; and a set of time-dependent quantities averaged over the whole simulation volume and calculated at each simulation time, such as: number density, mass, coordinates of the cloud centre of mass, the effective radius, temperature and mixing factor. In order to obtain spectra we first produce column density maps (both edge-on and down-the-barrel) and 2D histograms to understand the number density-temperature range at which different ion species exist. Using these results and Figure 6 from Tumlinson et al. [2017] we have identified which ions are typically observed in galactic winds and can be targeted in our research. In the next section we will explain in more detail how the spectra are produced by combining the two Python toolkits YT [Turk et al., 2011] and TRIDENT [Hummels et al., 2017], the STARBURST99 [Vázquez & Leitherer, 2017] software, and the CLOUDY Code [Ferland et al., 2017].
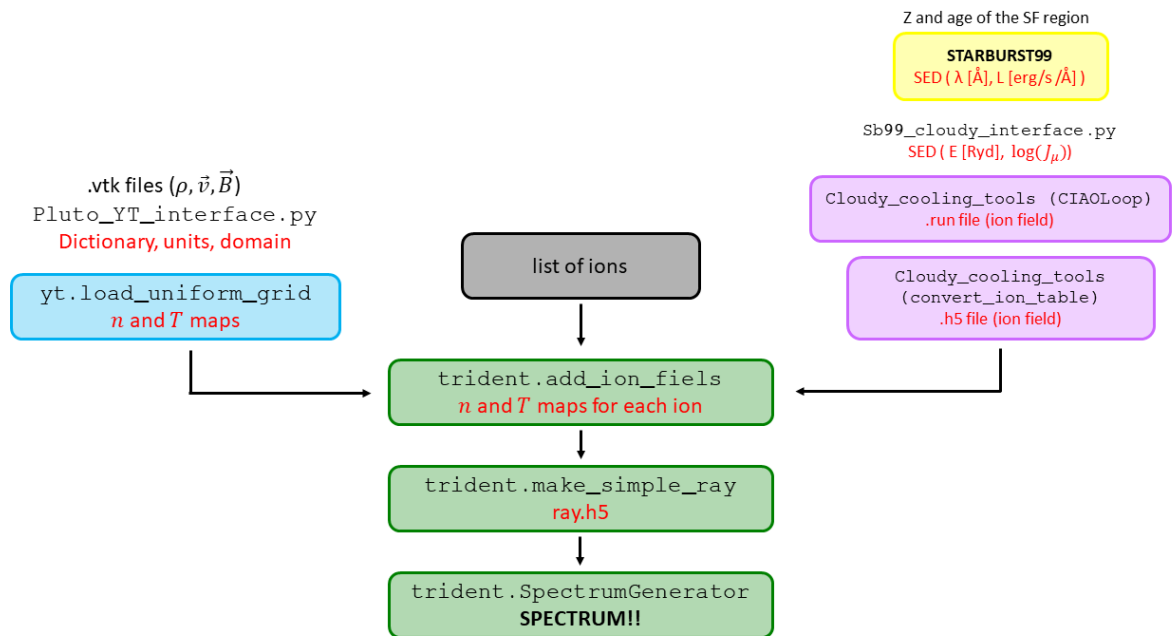

Figure 4.2: Flow chart detailing how YT, TRIDENT, CLOUDY, and STARBURST99 interact with each other in order to produce synthetic column density maps and absorption spectra. The blue box indicates how YT comes into play in the production of the spectra; the yellow cell concerns STRABURST99, the purple ones Cloudy and the green ones, Trident.

4.1.1 SPECTRA PRODUCTION

A more detailed picture of how the synthetic spectra are generated can be deduced from the flow chart in the FIG 4.2, which shows the key steps of the process. Starting from the steps above left, the first package we used was YT. YT is a toolkit for visualisation and analysis of datasets produced by 3D simulations. YT offers many advantages because once the datasets and units are loaded, it has some useful functions for data analysis, for example, we use `.proj` to compute projected quantities, such as column density, and we also generate projection or slice plots with `yt.SlicePlot` and `yt.ProjectionPlot`. Moreover, YT it is also the first dependency of TRIDENT. Thanks to the `yt.load_uniform_grid` function, it is possible to load the data and display temperature and density maps of the atomic cloud interacting with the galactic wind. However, YT does not have a native (default) tool that is able to directly read datasets produced by the PLUTO Code, so it was necessary to create a script to fill this gap. The Python script in matter is `Pluto_YT_interface.py` and it converts the content of each .vtk file into a series of numpy arrays. Subsequently, creates a dictionary with all the fields and their units in c.g.s. and defines a computational domain that coincides with the simulation one. A portion of the code is shown below as an example.

```
1  data = {('gas','density'): (rho, "g/cm**3"), ('gas','velocity_x'):\
2         (velx, 'cm/s'), ('gas','velocity_y'): (vely, 'cm/s'),\
3         ('gas','velocity_z'): (velz, 'cm/s'), ('gas', 'temperature'):\
4         (temp, "K"), ('gas', 'metallicity'): (metal, 'Zsun')}
5  bbox = np.array([[-6, 6], [-2, 22], [-6, 6]])
6
7  ds = yt.load_uniform_grid(data, rho.shape, length_unit=3.086e+19,\
8  mass_unit=(3.086e+19)**3, bbox=bbox, nprocs=1)
```

Once the grid-based data have been read into YT as a "StreamHandler" and once the ions to be analysed have been chosen, it is possible to produce column density maps, temperature and number density 2D histograms to compare with those produced earlier by the `diagnostics.py` script. If everything matches, the following step is to produce synthetic spectra exploiting the TRIDENT package. The first function used is `trident.add_ion_fields` which generates projected density maps for each ion in order to better understand their distribution within the cloud. The second step is to use the `trident.make_simple_ray` function to save all the field values of the ions intercepted by the beam and save them in an `.h5` file. Finally, the last part of the code involves the `trident.SpectrumGenerator` class which receives as input the ray and the range of wavelengths in Angstrom, the resolution $\delta\lambda$ and it generates as output the spectrum. In this final stage it is possible to decide the type of noise, its intensity, in order to produce a more realistic spectrum, and also to produce it in velocity space.

4.1.2 UV BACKGROUND

Trident uses by default the Haardt & Madau [2012] UV background, which only takes into account the cosmic UV background radiation. However, since the atomic clouds investigated in this study are located close to regions of high star formation, it is necessary to consider the extra UV radiation produced by the evolution of e.g. OB stars. The creation of a more realistic background is briefly summarised in the top right-hand part of FIG 4.2. We used the STARBURST99 software and the CLOUDY code, in particular the library `Cloudy_cooling_tools` (Smith et al. [2008], Smith et al. [2017]) to produce new ion tables to replace "hm2012_hr.h5" in the Trident configuration file. The steps followed to produce the UV background are:

- Choosing a SED from those produced by STARBURST99 that best represents the stellar population near the simulated atomic cloud. We chose a SED corresponding to a starburst system that has solar metallicity and is 3 Myr old, in agreement with McClure-Griffiths et al. [2013] paper concerning the observation of atomic hydrogen close to the Galactic center. SEDs have wavelength in on the x-axis and luminosity in $erg\ s^{-1}\ \text{Å}^{-1}$ on the y-axis.

- We converted the brightnesses to specific intensities and produced an `.out` file of the right format to be read by Cloudy. The Python script that deals with this procedure is `sb99_cloudy_interface.py` and the wavelengths with relative luminosities given as input, have been converted to E [Ryd] and $log(J_\mu)$. We also converted the SEDs representing the Haardt & Madau [2012] profile provided by CLOUDY13 and TRIDENT into the same units to visualize more clearly how important it is to consider a UV background which takes into account star formation. As can be seen in FIG 4.3, the SED produced with STARBURST99 has a flux at least one order of magnitude higher than the others, in the wavelength range that we are interested in. The SED we used for computing the ion balance in our models is in agreement with that reported in Werk et al. [2014] (see their FIGURE 13).

- We ran a simulation with `CIAOLoop` code, located inside `Cloudy_cooling_tools`, on Supermuc in order to obtain ion tables taking into account radiation from stellar feedback. The simulation receives as input the `.out` file produced in the previous step and was run with a temperature range from 1 to $10^9\ K$, hydrogen number density of $10cm^{-9} - 10^4\ cm^{-3}$ with step size of 0.0125 dex and at redshift = 0. This section of the project has been parallelized and run on SUPERMUC-NG (https://doku.lrz.de/display/PUBLIC/SuperMUC-NG).

- Finally, by exploiting the `convert_ion_balance_tables` function imported from `cloudy_grids` inside `Cloudy_cooling_tools` we generated the ion field output file in `.h5` format, which we then placed inside the `.trident` folder as the
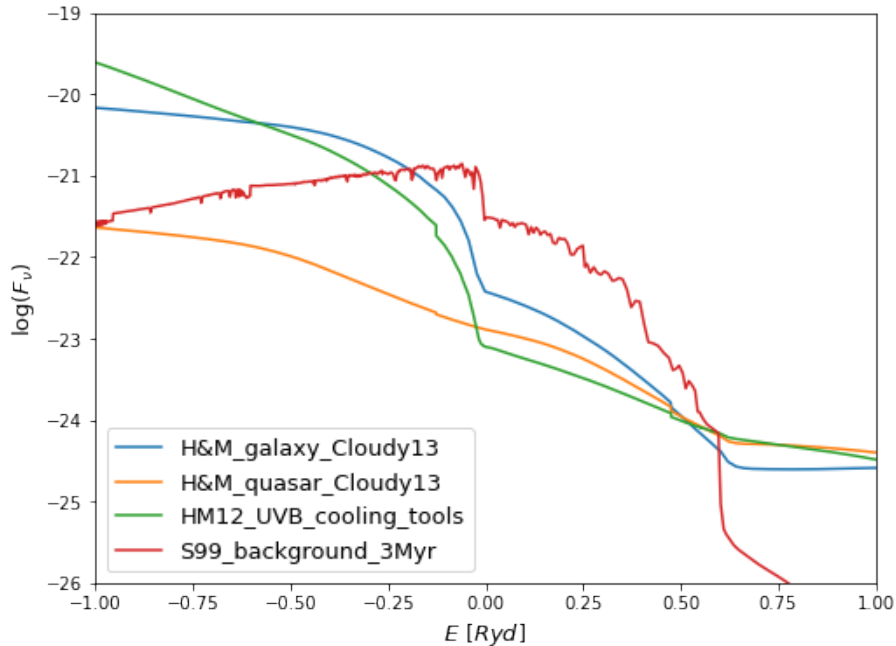
default background.

Figure 4.3: Several spectral energy distributions for the ionizing background radiation field. The first two lines in legend represent the SEDs compiled with data taken from https://www.ucolick.org/~pmadau/CUBA/HOME.html, covering the ionized cosmic emission produced by starforming galaxies (in blue) and quasars (in yellow). For the green model, data were downloaded from ./cloudy_cooling_tools/examples/grackle/HM12_UVB/z_0.0000e+00.out. While in red is shown the SED computed with STARBURST99 that best describes the UV background of our models.

4.2   Application to wind-cloud models

In this section we describe the evolution of wind-swept clouds over the duration of the simulations. In section 4.2.1 we describe how clouds develop different morphologies given different initial conditions. In particular, we study how different cooling floors and magnetic field orientations affect the evolution of clouds. To achieve this, we analyse the trends of the diagnostics discussed in section 3.3.2 combined with or edge-on and down-the-barrel column number density maps (FIGURE 4.4 and FIG 4.5). Subsequently, we describe how these differences also have effects on the ionization levels of the elements in the systems. We find that different cooling floors and magnetic fields, in fact, alter the morphology of the cloud and have secondary effects on the number density and temperature of the evolving flow. In section 4.2.2 we describe the synthetic spectra produced from single cloud simulations and discuss which ions are observable in our models and what their average column number densities are during the lifetime of clouds. Having number

density constraints for the various ions is crucial for comparison with observations and to understand what feedback processes influence cloud evolution in the observed galactic winds.

4.2.1   WIND-CLOUD EVOLUTION

In this sub-section we describe cloud evolution. In order to do so, we present in FIGURE 4.4 and in FIGURE 4.5 the column number densities of our 4 models, edge-on and down-the-barrel clouds, respectively, taken at 0.75, 2, and 3.25 Myr. In addition, in the panels in FIGURE 4.6 we have shown some of the trends in the diagnostics discussed in Section 3.3.2, such as radius, mixing fraction, number density and temperature, showing the comparison between the various models (the red line always represents the RWC-R32-AL-F1 model, the blue line the RWC-R32-TR-F1 model, the purple line the RWC-R32-AL-F2 model, and the green line the RWC-R32-TR-F2 model).

4.2.1.1   Filament formation and evolution

Each cloud, due to different initial conditions has a different evolution. Below, we report a detailed description for each model.

- **RWC-R32-AL-F1**. We recall that in this simulation the cooling floor is set at 50 K and the magnetic field is aligned with the direction of the galactic wind. The cloud, which initially has a spherical shape and is at rest, placed in the origin of the coordinate system, interacts with the wind and produces a tail along the vertical direction (see first column of FIGURE 4.4). The main mechanism leading to the formation of the tail is the emergence of pressure gradients along the streaming direction. KH and RT instabilities are quite damped in these model due to the increase of the density contrast χ in eq. 3.36, thus the cloud always remains fairly compact, maintaining its central symmetry in the x-z plane. This behaviour occurs because dense gas can rapidly cool down to $\sim$ 50 K, and become pressure confined, thus maintaining a small cross section throughout the evolution, as it is visible in the first column of FIGURE 4.5. This cloud therefore evaporates slowly, the outer material is constantly being stretched, however, since the system remains compact in the x-z plane, the cloud's cross section is kept small. As a result, the cloud does not gain much momentum from the wind, so it moves only slightly from its starting position and does not undergo significant acceleration.

- **RWC-R32-TR-F1**. In this model the cloud still has a cooling floor set to 50 K, but the initial magnetic field is transverse to the direction of the galactic wind. Also in this case, the system develops a tail due to the stretching via pressure gradients.
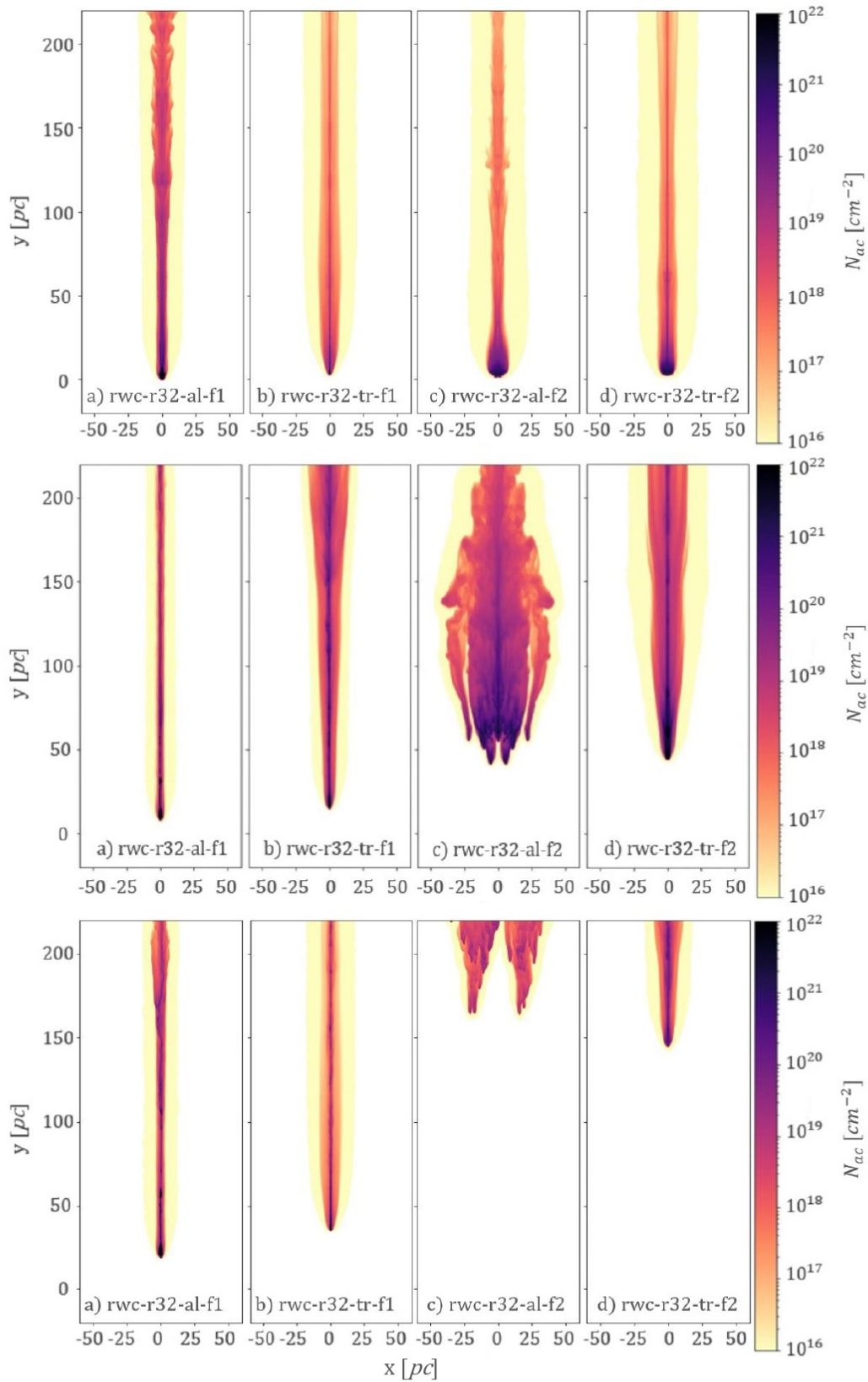
Figure 4.4: Evolution of edge-on column density projected along the z-axis, in wind-clouds models. The top 4 panels are taken at $t = 0.75$ Myr, at $t = 2$ Myr in the middle panels, and at $t = 3.25$ Myr in the bottom plots.
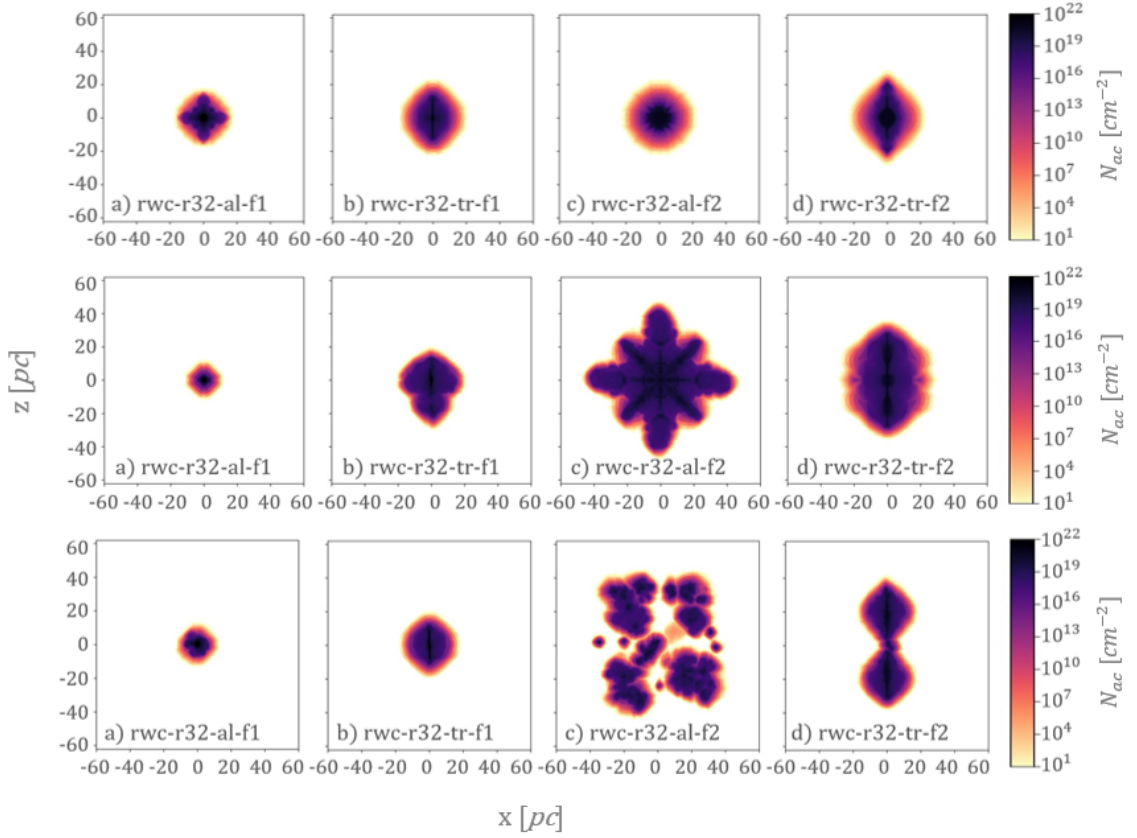
Figure 4.5: Evolution of down-the-barrel column density projected along the y-axis, in wind-clouds models. The top 4 panels are taken at $t = 0.75$ Myr, at $t = 2$ Myr in the middle panels, and at $t = 3.25$ Myr in the bottom plots.

Although the filament remains fairly confined along the x-z plane, in this case the cloud undergoes additional stretching along the z-axis (visible in the second column of FIGURE 4.5). Streaking along this direction causes the cloud's cross section to increase, and the cloud becomes more prone to evaporation. In the last timestep of the second column in FIGURE 4.4, in fact, the footpoint size is smaller than in the "RWC-R32-AL-F1" model, because more envelope gas has been removed by the wind. Again, the cloud does not seem to acquire much momentum from the wind, but it does move more than in the "RWC-R32-AL-F1" model. In fact, the position of the centre of mass is farther away along the y-axis than in the "RWC-R32-AL-F1" model. The tail also expands further than in the first model as the folding of magnetic field lines around the filament leads to the formation of a current sheet along Z. Diffuse gas, trapped between the folding lines, develops vorticity, which then aids cloud material to slip in between the folding B field lines and move downstream (see also Banda-Barragán et al. [2016]).

• **RWC-R32-AL-F2**. In this simulation the cooling floor is set at 10^4 K and the magnetic field is aligned with the direction of the galactic wind. The cloud has a very different evolution than in the previous cases, caused by its inability to cool down

below 10^4 K and become ultra compact as in the previous cases. The cloud always produces a downstream tail, but in this case the growth of instabilities in the outer layers of the footpoint and the tail allows the cloud to efficiently mix with the external wind, and evaporate quickly as a result (see third column of FIGURE 4.4). This model is the one in which the cloud reaches the largest size in all three axes, and the only one in which the cloud breaks up within the time-scale of the simulation. Because of the large cross section, shown in the third column of FIGURE 4.5, the cloud mixes faster with the wind than in the other cases and acquires more momentum from it.
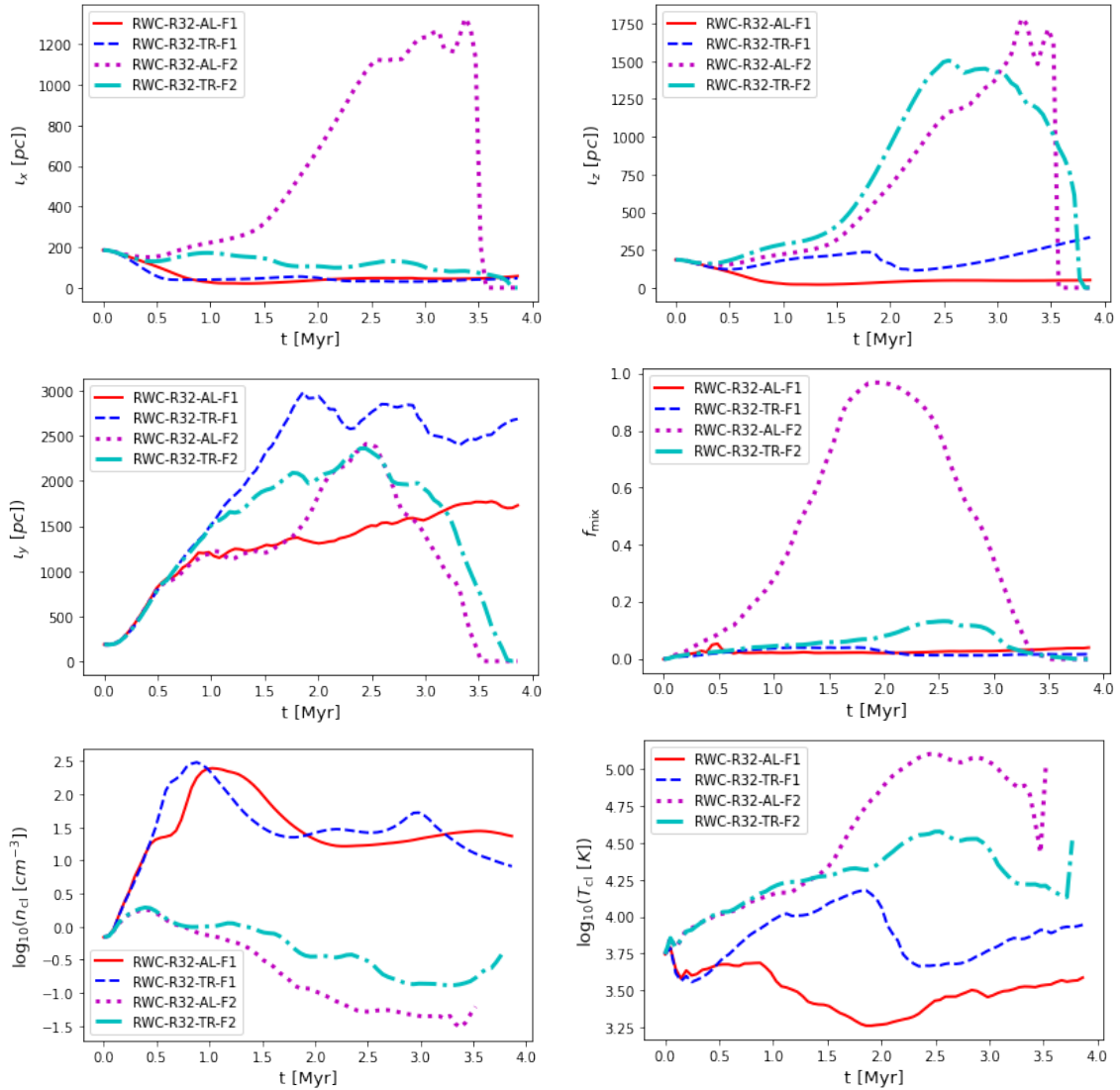

Figure 4.6: Diagnostics time evolution for the wind-cloud models. The top left panel, shows the cloud radius along the x-axis ι_x, the top right panel reports ι_y, the middle left panel displays ι_z, the middle right reports mixing fraction, the bottom left plot shows the cloud number density, and the bottom right, the cloud temperature. The RWC-R32-AL-F1 model is shown in red, RWC-R32-TR-F1 in blue, RWC-R32-AL-F2 in purple, and RWC-R32-TR-F2 in green.

As a result, in this model the cloud accelerates and reaches larger distances along the domain. Despite this, the growth of KH and RT instabilities destroys it before the end of the simulation. In fact, in this case, cloud breaks up and splits into cloudlets.

- **RWC-R32-TR-F2**. We recall that in this last model the cooling floor of the cloud is placed at 10^4 K and the magnetic field is transverse to the direction of the galactic wind. As in all other cases, also in this simulation the cloud develops a downstream tail. Compared to the "RWC-R32-AL-F2" case, however, the magnetic field orientation of this simulation causes the expansion of the cloud along the z-axis in the x-z plane (see fourth column of FIGURE 4.4). Since the cloud remains confined along the x-axis, its cross-section is not as large as in the "RWC-R32-AL-F2" model, but at the same time, it is not compact enough to prevent the cloud from splitting in at least two cloudlets (see fourth panel of FIGURE 4.5). In this case the cloud acquires momentum from the wind and is able to accelerate. Indeed, in the final stages all the gas belonging to the cloud exits the box.

4.2.1.2   50 **K cooling floor versus** 10^4 **K**

In the two models with the cooling floor at 50 K, dense gas in the clouds is able to cool down to temperatures near the cooling floor, while at the same time, mixed gas removed from the main cloud can also condense rapidly once it is perturbed by the galactic wind. This is in constrast to the models with cooling floor at 10^4 K, which are generally warmer and less confined. In fact, in the "-F1" models, we observe in the two top panels of FIG 4.6 a reduction of the cloud cross section in the x-z plane with respec to to its size at t=0 (in model "RWC-R32-AL-F1")), and a minor increase in the cloud cross section (in model "RWC-R32-TR-F1"). In these models isobaric cooling is expected, with the clouds trying to reach pressure balance with the outside medium. Radiative cooling causes a drop in thermal pressure, while shock heating an increase, so models with the 50K cooling floor, where cold gas is predominant become confined, while models with the 10^4 K cooling floor, where warm gas is predominant can expand further. As can be seen in the top panels of FIGURE 4.6, the "-F1" models are those in which the extensions ι_x and ι_z remain smaller overall throughout the evolution. The smaller cross sections of these clouds also mean they cannot efficiently accelerate along the y-axis. Actually, in the panel describing the ι_y evolution in the left panel of the central row in FIGURE 4.6, the values are generally high owing to the filamentary morphology of the clouds, which are fairly extended along the streaming direction. The decrease seen at the end of these curves is due to cloud material leaving the domain.

In both models with a cooling floor at 50 K, we note a minor growth of the KH and RT instabilities (first two columns of FIGURE 4.4), but in general they are highly damped as the clouds contract and their densities also increase at wind-cloud interfaces. If the KH and RT instabilities were able to develop significantly, they would also cause more

mixing between the material belonging to the cloud and the galactic wind. Indeed, in the right panel of the central row in FIGURE 4.6, the "-F1" models are those in which the mixing fraction is lowest; whereas in the "AL-F2" case, the cloud mixes almost fully with the surrounding medium, until it then evaporates completely. Moreover, the difficulty in forming KH and RT instabilities, makes the cloud take longer to evaporate. In fact, in the "-F1" models, instead of a global expansion of the cloud that would result in breaking up, we find a continuous erosion and a progressive decrease of ι_x, and also a decrease of ι_z in the "-AL" case, or an initial increase of ι_z, which then tends to decrease in the "-TR" model (top panels of FIGURE 4.6).

In addition, maintaining a small cross section in the x-z plane implies less momentum transfer from the galactic wind to the cloud. The "-F2" models, in which this cross section is larger, are those that reach larger distances and speeds.

Finally, the ability of the cloud to cool to lower temperatures and therefore reach higher densities is reflected in the bottom panels of FIG 4.6, where the trends of the temperature and number density of the clouds are shown. The "-F1" models are those with higher densities and lower temperatures, and we expect that these differences can be reflected in the synthetic spectra. In section 4.2.3 we will discuss in detail which ions can be observed in these four models based on the densities and temperatures of the underlying gas.

4.2.1.3 Aligned versus transverse magnetic fields

The initial topology of the magnetic field also has effects on the morphology of clouds as they evolve. In models where the magnetic field is aligned with the wind direction, the passage of the shock does not compress the field lines and therefore does not amplify the magnetic field in any particular direction. On the other hand, in the case where the magnetic field is transverse, the passage of the shock, folds the field lines around the clouds, compresses them in front of the clouds, and by doing so, amplifies the magnetic field by a factor of a $\sim$ 4 (see Banda-Barragán et al. [2016]). As a consequence of the folding of field lines along X, the cloud has less freedom to expand on the x-axis, and dilates along the z-axis (in the direction of the current sheet, see Banda-Barragán et al. [2016], Grønnow et al. [2017]). Another result of this shielding is the inhibition of KH instability growth, small-scale vortices are damped, and the tail has a more laminar flow as also described in Banda-Barragán et al. [2016]. The magnetic field makes the stripping of material from the outer layers more difficult; therefore, the filaments in transverse field models become less turbulent. This phenomenon is reflected in the trend of the mixing fraction in the right panel of the middle row in FIGURE 4.6, where the "TR" models have a lower mixing fraction value than their counterparts with an aligned magnetic field.

However, a transverse magnetic field does not have exactly the same effect on the cloud morphology in the two models with different cooling floors, suggesting that magnetic fields can have different effects on cold and warm wind-swept clouds. In FIGURE 4.5 we observe, for example, that in the "TR-F1" model the cloud cannot expand along the

x-axis, and the material tends to spread out along the z-axis. As seen in the bottom right panel of FIGURE 4.6 in fact, the "RWC-R32-TR-F1" model has higher temperatures than the "RWC-R32-AL-F1" model; this different trend causes some differences also in the synthetic spectra that we have produced and that we will discuss in section 4.2.3.

In the models with the 50K cooling floor, the cloud with transverse magnetic field also acquires more momentum from the wind than the "RWC-R32-AL-F1" model due to its larger cross section, and acquires more velocity as a result.

On the other hand, in the "RWC-R32-TR-F2" case, the shielding of the tail by the magnetic field makes the cloud more compact than in the "RWC-R32-AL-F2" model; i.e., less prone to expansion and therefore evaporation. Specifically, in this case, the "RWC-R32-TR-F2" system has higher densities and lower temperatures for much of the cloud evolution, compared to its counterpart with an aligned magnetic field. In the bottom panels of FIGURE 4.6 one can appreciate these differences between "RWC-R32-TR-F2" and "RWC-R32-AL-F2" models up to the time when a large fraction of cloud material exits the domain, blown away by the wind. The differences in number density and temperature also has some effects on the resulting ion populations and the spectra as well (see section 4.2.3).

4.2.2   ABSORPTION SPECTRA IN WIND-CLOUD MODELS

In this section we analyze the results obtained using the tool that we created, which is already described in section 4.1. After studying the dynamical evolution of the clouds in the respective simulations, we produced 2D histograms of number densities versus temperature in order to determine which ions can exist in our wind-cloud systems, and should therefore be included in our spectral analysis. Each ion, in fact, as can be seen in FIGURE 1.2, has its own range of temperature and number density in which it can be observed.

Once, we identify the ions, we utilise our PLUTO-Trident interface to compute density maps of some of them in particular H I and O VI, as both are widely observed in star-forming galaxies. We select only one time, t=2 Myr from the available simulation snapshots, as during this time it is possible to best appreciate the morphological differences of the various wind-swept clouds (as we already discussed in section 4.2.1). As can be seen from FIGURE 4.8 and FIGURE 4.9, we have produced column number density maps integrated along all three axes in order to understand how each atomic species is spatially distributed within the simulated clouds. Afterwards, we display the spectra of several ions, namely H I, O VI, Mg II, Ne VIII, N V, C III, Si IV, produced by Trident given the temperature and density conditions of the evolving clouds at the selected time of 2 Myr. For this, we use a ray passing exactly through the centre of each cloud.

Based on a first qualitative analysis of the spectra, we investigate whether the different initial conditions of our four wind-cloud models affect the selected atomic lines. At the end, we report the column number density values of the individual ions, spatially aver-

aged over the x-z plane. These average values were obtained at each time step, through down-the-barrel projections, performed using Trident. From this latest analysis we can deduce some important conclusions regarding whether different initial conditions have effects on the chemical concentrations of the various ions, and which ions should be more detectable at different instances of the evolution of these systems.

4.2.2.1   2D histograms of number density versus temperature in wind-cloud models

In this section we report 2D histograms of number density versus temperature of our four wind-cloud models. For consistency, we take the same times as reported in section 4.2.1, namely at 0.75, 2 and 3.25 Myr. The first feature we note from this thermodynamical analysis is that the different cooling floors between the F1 and F2 models causes in the first two rows of FIGURE 4.7 (F1 models) much gas to be at 50 K and with number densities between $1\ cm^{-3} < n < \times 10^2\ cm^{-3}$, while in the last two rows (F2 models), most of the cloud gas sits at temperatures $\geq 10^4$ K. Furthermore, in the F1 models, gas with $n \sim 10^{-1}\ cm^{-3}$ stays in the warm phase with $T \sim 10^4$ K, but the cooling function causes all gas with densities greater than $1 cm^{-3}$ to condense directly down to 50 K. This occurs because the heating function is $\approx n$ while the cooling function is $\approx n^2$; therefore, heating of material at high densities is unable to stop gas to collapse , but does prevent warm gas from cooling below 10^4 K, thus creating a three-phase medium, akin to that reported by **??** for shock- multicloud models. An important property, and in agreement with the previous section, is that in the F2 models, it is easier to appreciate differences related to the orientation of the magnetic field, which implies magnetic field can have more pronounced effects in warm clouds than in cold clouds. In fact, in the bottom two rows we can see that a large fraction of gas is found in the three images of the "RWC-R32-AL-F2" model with 10^6 K $> T < 10^4$ K and $10^{-1}\ cm^{-3} > n > 10^{-1}\ cm^{-3}$; whereas in the "RWC-R32-TR-F2" model, the gas tends to concentrate at $T \sim 10^4$ K, generating a plateau covering densities of $1\ cm^{-3} > n > 10^{-2}\ cm^{-3}$.

From this thermodynamic analysis and a comparative study of Cottle et al. [2018], where the chemical evolution of wind-clouds models with conductivity feedback is reported, we have opted to include in our analysis the synthetic spectra the following ions: C III, H I, Mg II, Ne VIII, N V, O VI and Si IV, which should all exist under the conditions we see in FIGURE 4.7. In the next two sections we report in detail the column density maps of HI and O VI, the other elements will be only briefly discussed.

4.2.2.2 N_{HI} maps of wind-cloud models

In this section we study the distribution of HI in our simulated clouds, at $t = 2$ Myr. FIGURE 4.8 shows column number density maps of the HI projected onto the x-z plane (top panels), x-y plane (middle panels), and z-y plane (bottom panels). From these plots we can deduce that the HI is in general a good tracer of cloud gas, since it is not observable outside of it, because the wind temperatures are too high and gas is fully ionised. From

the colourbar we can see that this species cover a wide range of column number densities and is particularly concentrated in the dense parts of the cloud.
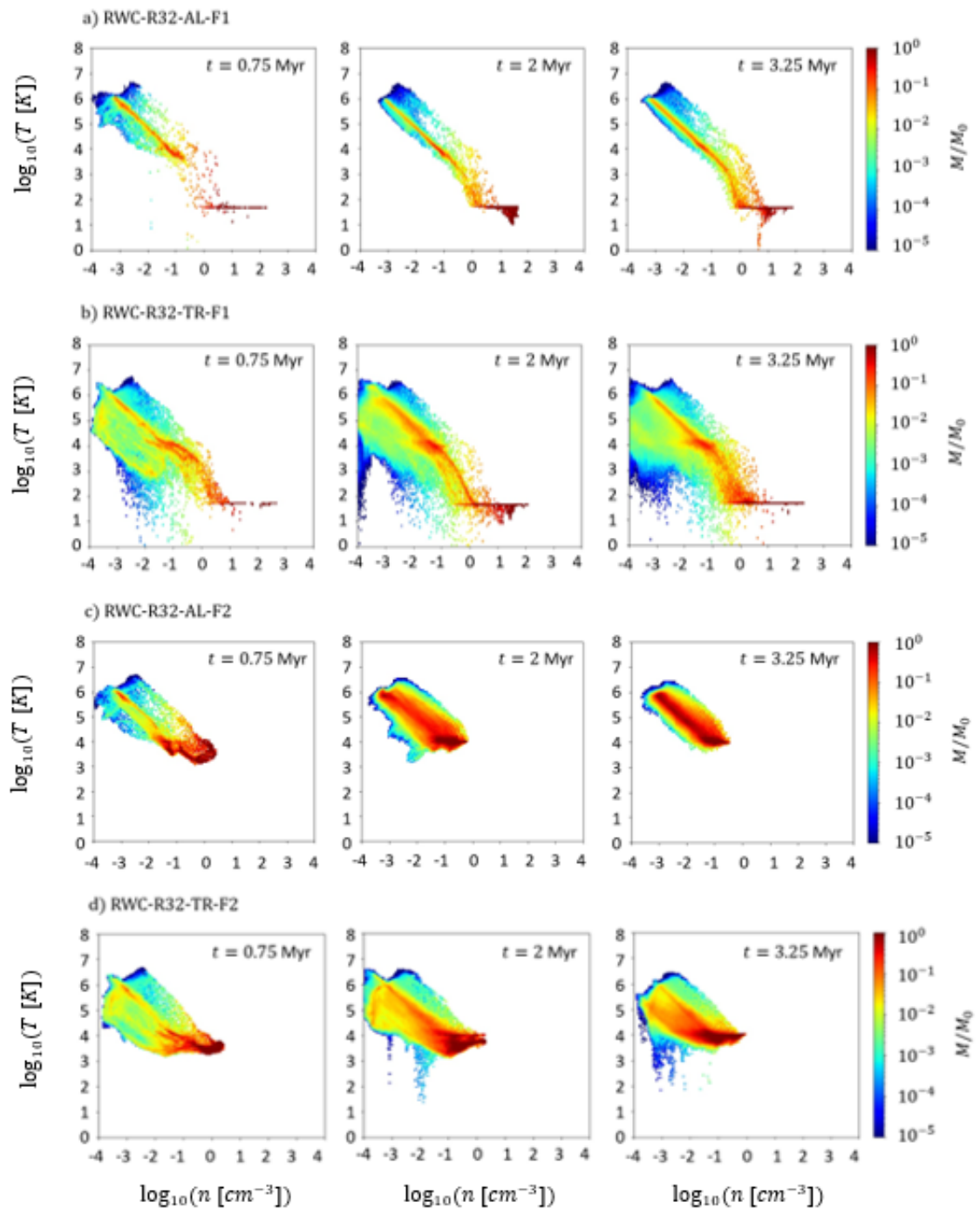

Figure 4.7: 2D histograms with number density and temperature of wind-cloud models. The first row represents the RWC-R32-AL-F1 model, the second row the RWC-R32-TR-F1, the third row the RWC-R32-AL-F2, and the fourth one, RWC-R32-TR-F2. For each of the wind-cloud models, 2D histograms are shown at the same three time instants also shown in the column density maps in FIGURES 4.12, 4.5, i.e., $t = 0.75$ Myr (in the left column), $t = 2$ Myr (in the middle column), and $t = 3.25$ Myr (in the right column).

The HI, in fact, is more contained in the inner regions of the four footpoints of all the filaments and in those areas of the tails where the interaction with the galactic wind causes gas compression via convergent flows. Another peculiarity is that in these plots it is also possible to observe the differences in the cloud morphologies caused by the different cooling floors and magnetic field orientations, which were reported in section 4.2.1.

If we focus on the top four panels of FIGURE **??**, especially on the centre of the clouds, we can appreciate some differences between the various models in the down-the-barrel spatial distributions of HI. In the F1 models, in fact, HI is highly clustered at the centre of the cloud projection and, thus, we expect to observe deeper and broader Lyman series lines than in F2 models. Indeed, in the F2 models, the number column density of the HI at the centre of the cloud down-the-barrel onto the x-z plane appears to be at least two orders of magnitude lower than in the F1 models. In addition, still in the F2 models, we also observe differences between the "RWC-R32-AL-F2" and "RWC-R32-TR-F2" cases. HI seems to be denser at the center of the cloud in the case with the transverse magnetic field compared to the aligned one. This supports the idea that a transverse magnetic field keeps the cloud more compact via shielding in the model with cooling floor at 10^4 K, making, consequently, HI more detectable, compared to the case with the same cooling floor and magnetic field aligned with the direction of the wind.

4.2.2.3 N_{OVI} **maps of wind-cloud models**

This section shows density maps of O VI observed from three different angles, namely down-the-barrel x-z plane in the top plots of FIGURE 4.9, x-y plane in the middle plots, and z-y in the bottom four plots. Contrary to H I, O VI is present in both cloud and wind material, however its concentration is higher inside the clouds, especially in the inner parts. Moreover, in this case N_{OVI} covers a much smaller range, two orders of magnitude versus eleven of HI.

Regarding the concentration of O VI at the center of the down-the-barrel projection on the x-z plane, we can state that in the F1 models we expect slightly higher column number densities of O VI in the case with transverse magnetic fields. For the F2 models, however, O VI appears to be more abundant at the center of the down-the-barrel projection of the "RWC-R32-AL-F2" model compared to "RWC-R32-TR-F2".

In the next section, where the synthetic spectra of the four dense clouds models at $t = 2$ Myr are shown, we examine whether the differences just reported for the number density maps of HI and O VI have any impact on the spectral lines, and whether differences can also be appreciated for the other ions.
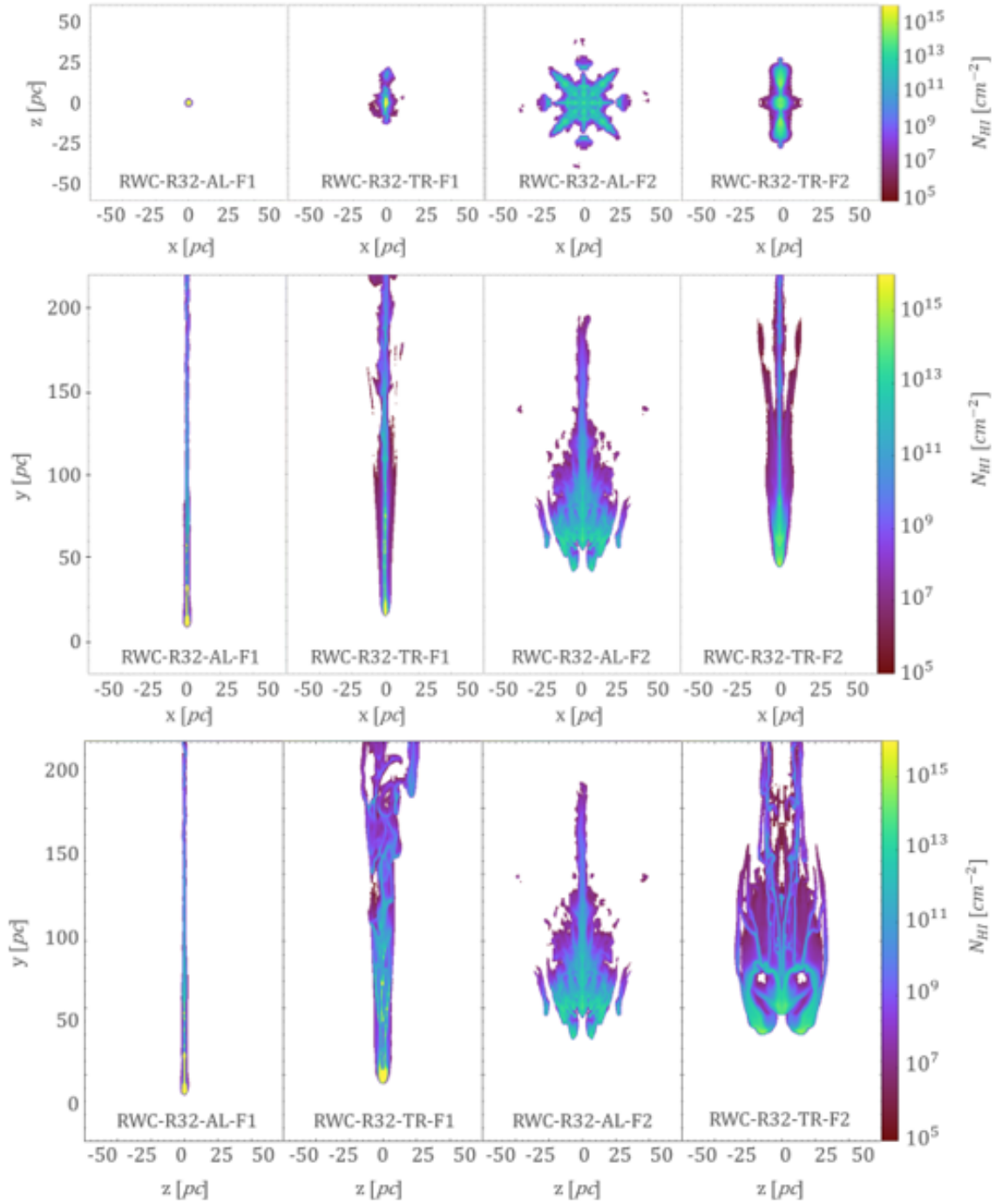
Figure 4.8: HI column number density in wind-clouds models at $t = 2$ Myr, computed with Trident. The column number densities are integrated along the y-axis in the first row, along the z-axis in the four panels in the middle, and along the x-axis in the bottom plots.

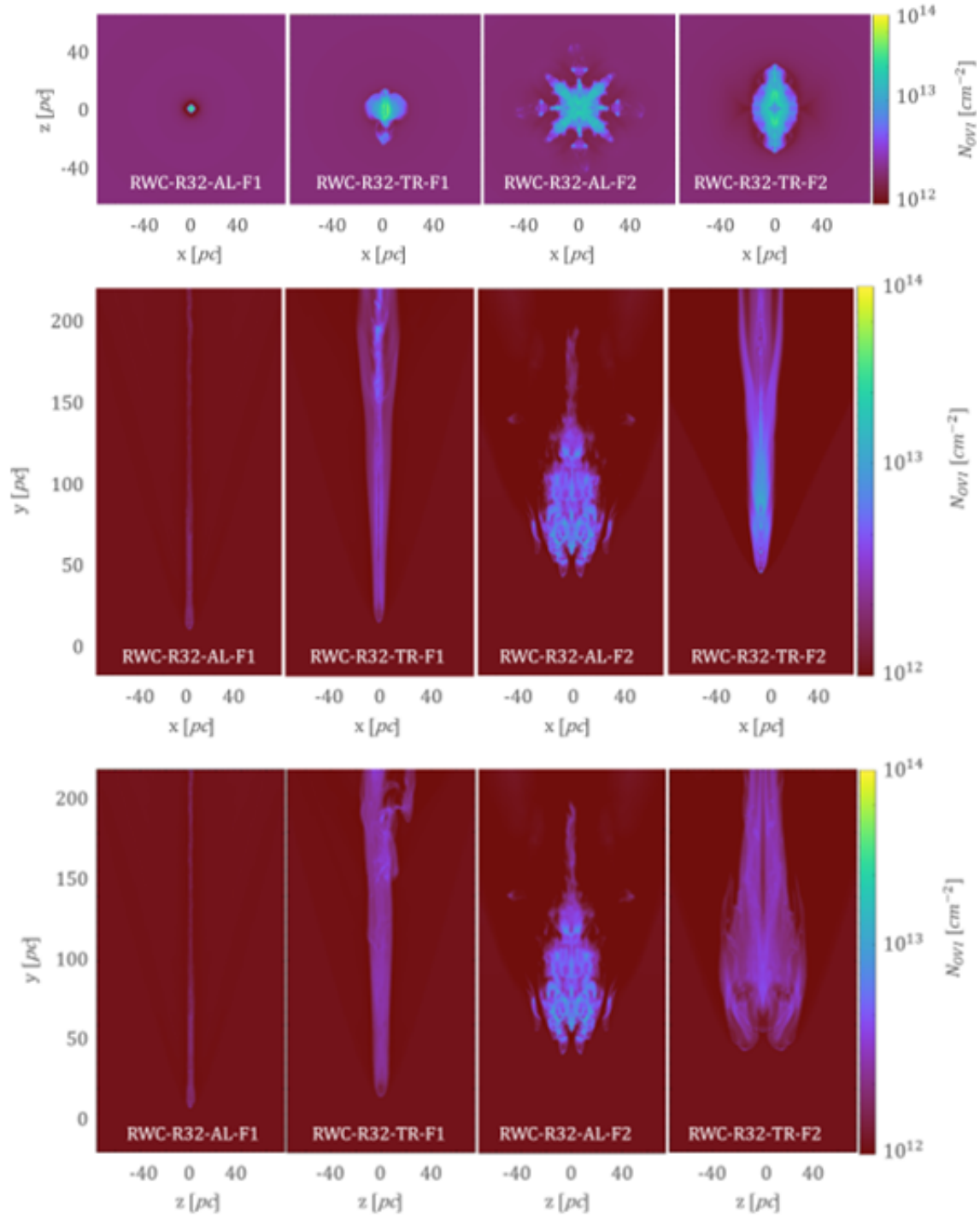Figure 4.9: O VI column number density in wind-clouds models at $t = 2$ Myr, computed with Trident. The column number densities are integrated along the y-axis in the first row, along the z-axis in the four panels in the middle, and along the x-axis in the bottom plots

4.2.2.4 Down-the-barrel spectra at $t = 2$ Myr

In this section, the down-the-barrel spectra of the four clouds, obtained at $t = 2$ Myr and with a ray passing through the center of the cloud, are shown in FIGURE 4.10. We

compute these spectra to study how different initial conditions influence the shape of the spectra. From the four panels in FIGURE 4.10, where we show spectra between 900-1500 Å, we find that the assumptions made about HI concentrations and the O VI discussed above are also present in the spectral lines. In the F1 models, for example, the depth of the Lyman series are deeper than in the F2 models, owing to the larger hydrogen column densities in the much colded F1 clouds. The orientation of the magnetic field, on the other hand, does not seem to particularly affect the spectra of HI, making the resulting spectral lines of this ion more sensitive to the cooling floor than to the orientation of the magnetic field (but of course if we would average the spectra over a wider area, instead of taking just one ray, this conclusion may differ). The O VI, too, does not contradict the conclusions drawn in section 4.2.1, since the depth of the lines is greater in the "RWC-R32-TR-F1" case than in the "RWC-R32-AL-F1". Whereas an opposite trend with respect to the magnetic field is observed in the F2 models, where the O VI lines are deeper in the "RWC-R32-AL-F2" case than in the "RWC-R32-TR-F2" (this is because the current sheet in the "RWC-R32-TR-F2" model is exactly at x,z=0, but if we take averages over a wider area, we may see a different picture).

As for the other elements, some of them do not seem to change their concentration under different initial conditions, such as, for example, C III and Si IV. Mg II, on the other hand, seems to be present only in the "RWC-R32-TR-F1" model. The N V lines instead do not seem to vary too much according to the initial conditions of the simulations, except for the case "RWC-R32-TR-F1" where less N V concentration is observed.

Thus, in this very first analysis, we can state that both cooling floors and magnetic fields have effects on cloud morphology, density and temperature, which are also reflected on chemical abundances and spectra. The differences, however, are more obvious in the column number density maps than in the spectra themselves, but at least some distinctive features of magnetic fields on the spectra have been found.
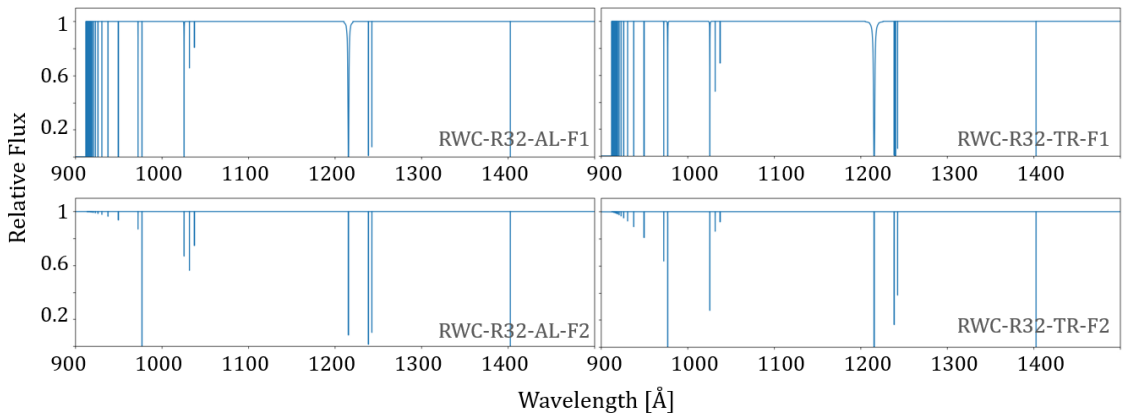

Figure 4.10: Down-the-barrel spectra of wind-cloud simulations made with Trident. Spectra are produced with a ray passing through the cloud center, and at $t = 2$ Myr.

4.2.2.5 Time evolution of averaged ion column densities $< N_{ions} >$, in wind-cloud models

One of the goals of this thesis is to understand whether consistent differences in column number densities of our ions can be captured, given different initial conditions. To make our study statistically more consistent we opted to calculate the column number densities of each ion, averaged across all cells in the x-z plane, i.e. down-the-barrel. This way we do not limit our study only to the center of the cloud as we did for the spectra in the previous section, and we also study their time evolution. To do this type of analysis, we considered column number density values for each ion greater than 10^{12} cm^{-2} since below this value it is difficult to make observational comparisons with the various models because of the noise added by the wind or very diffuse mixed gas. In this way, we would like to understand if it is always possible to observe all the selected ions during the evolution of the clouds, if there are drastic changes in ions column densities throughout the evolution of wind-cloud systems, and also which ions are more sensitive to the cooling floor and which ones to the initial orientation of the magnetic field. In FIGURE 4.11 all the trends for the various species are shown and we will discuss them one by one starting from the top left panel. In these plots we find in red "RWC-R32-AL-F1", in blue "RWC-R32-TR-F1", in purple "RWC-R32-AL-F2", and in green "RWC-R32-TR-F2":

- **H I.** As already deduced from the previous subsections, H I is very sensitive to different cooling floors; the concentration of this ion, in fact, is very sensitive to the different trends of n_{cl} shown in FIGURE 4.6. Initially, all four single cloud models start with $< N >_{HI} \sim 10^{16}$ cm^{-2}, but immediately the F1 models deviate significantly from the F2 models. In the former case, values of $< N >_{HI} \sim 10^{19-20}$ cm^{-2}, (similar values where observed in the MW by **??**), while in the F2 models $< N >_{HI}$ decreases to values $< 10^{14}$ cm^{-2}. From the plot in FIGURE 4.11, however, it can be seen that starting from ~ 1.5 Myr, we can also observe differences in the F2 models, regarding the magnetic field. In "RWC-R32-TR-F2" in fact, $< N >_{HI}$ is always above the "RWC-R32-AL-F2" model, which implies that transverse fields in warm clouds can shield some of the cold dense gas inside these cloud.

- **O VI.** The O VI does not show strong differences in $< N >_{OVI}$ among the four models; actually, the scatter between the various curves varies in the range of $10^{13.65} - 10^{13.8}$ cm^{-2}. This occurs because this ion is present not only in the cloud, but also in the surrounding wind. The "RWC-R32-AL-F1" model, for example, has values of $< N >_{OVI}$ that are extremely constant throughout the evolution of the simulation. This is because this is the case where the cloud expands less and also mixes less with the surrounding medium, the number of cells dominated by the galactic wind are greater than those occupied by the cloud. Also for the same reason, the "RWC-R32-AL-F2" model is the one where $< N >_{OVI}$ increases the most, since this is the one where the cloud expands the most.

- **Mg** II**.** This ion is also sensitive to the cooling floor even from the beginning, but less so to the initial magnetic field orientation. Also in this case, the F1 models have the highest average Mg II concentrations as Mg II is a known tracer for dense neutral CGM and ISM gas, maintaining a value more than four orders of magnitude above the F2 models, which are far too warm for this ion to be dominant. An important feature is that after ~ 0.7 Myr in the "RWC-R32-AL-F2" model the Mg II is no longer visible, as the values of $< N >_{\mathrm{MgII}}$ become lower than the threshold set at 10^{12} cm^{-2}. The same happens in the "RWC-R32-TR-F2" model after ~ 1.7 Myr from the initial instant.

- **Ne** VIII**.** For this ion, all the four models deviate little from each other, indicating that this ion is not sensitive to cooling floor and magnetic field variation. The trend of $< N >_{\mathrm{NeVIII}}$ is kept constant at $\sim 10^{13.6-13.7}$ cm^{-2} up to ~ 3 Myr. After ~ 3 Myr, for all models analyzed, a very steep increase in the concentration of this ion is observed, up to $< N >_{\mathrm{NeVIII}} = 10^{14.6}$ cm^{-2}. A really slight difference is shown by the "RWC-R32-AL-F2" case, which exhibits a smoother increase of $< N >_{NeVIII}$ than the other three models. From this analysis we conclude that Ne VIII is not a good indicator of cooling floor and magnetic field and the results concernig this ion will be studied in more detail in future work.

- **N** V**.** In the plot of FIGURE 4.11 showing the trend of $< N >_{\mathrm{NV}}$ in the various models, we can see that the four lines deviate little from each other up to ~ 1.5 Myr, with a growth of $< N >_{\mathrm{NV}}$ up to about $10^{14.4}$ cm^{-2}. From ~ 1.5 Myr to ~ 2.5 Myr, the "RWC-R32-AL-F1" model exhibits an increase in $< N >_{\mathrm{NV}}$ up to $\sim 10^{14.8}$ cm^{-2}. This trend exactly mirrors the increase in T shown in FIGURE 4.6, where, for the "RWC-R32-AL-F1" case, $\log_{10} T < 3.5$ K. Moreover, still starting at ~ 1.5 Myr, a decrease in N V concentration is observed in the "RWC-R32-AL-F2" model, which decays until the end of the simulation duration. Starting from the same instant ($t = 1.5$ Myr), in the F2 models, we can recognize differences caused by the magnetic field. The "RWC-R32-TR-F2" case, for example, at ~ 3.2 Myr, reaches values of $< N >_{\mathrm{NV}}$ one order of magnitude larger than the case with an aligned magnetic field. As was also seen for C III and HI, at ~ 3.5 Myr, in the "RWC-R32-AL-F1" case, the cloud exits the volume and the same happens at ~ 3.8 Myr in the "RWC-R32-TR-F1" model. This is due to the stronger acceleration of the clouds caused by the acquisition of momentum by the wind.

- **C** III**.** In the plot representing C III from FIGURE 4.11, we see that this ion could be a good tracer to identify differences in cloud evolution caused by the different cooling floors and magnetic field orientations. Initially, in all the four models $16 < \log_{10}(< N >_{\mathrm{CIII}} [cm^{-2}]) < 16.5$; but already after 0.5 Myr, in the "RWC-R32-AL-F1" case, the density of C III increases until it reaches column number densities $\sim 10^{17-17.5}$ cm^{-2} and then stabilises on this plateau. The "RWC-R32-TR-F1" model,

from the beginning, maintains a fairly constant trend throughout the duration of the simulation with values around $\log_{10}(< N >_{\text{CIII}} [cm^{-2}]) \sim 16.5$, which are 1 dex. lower than in the AL model. On the other hand, the models with cooling floor set to 10^4 K show a decreasing $< N >_{\text{CIII}}$ with time as these clouds remain warmer and have lower densities than their F1 counterparts, combined with the early escape, and by the early escape of the material belonging to the cloud from the simulation box. For example, as seen in section 4.2.1, the model "RWC-R32-TR-F1" exhibits a fairly constant trend throughout the simulation. In fact, clouds in F2 models are the ones that gain more momentum from the wind and accelerate the most, as seen in section 4.2.1. After ~ 1.5 Myr, then, the "RWC-R32-AL-F2" model exhibits an drastic decreasing $< N >_{\text{CIII}}$ which also coincides with the declining n_{cl} and increasing T_{cl}, ι_x and ι_z shown in the FIGURE 4.6 plots. Finally, the exit of the cloud from the volume coincides with a drop of $< N >_{\text{CIII}}$ to ~ 3.5 Myr in "RWC-R32-AL-F2" and to ~ 3.8 Myr in "RWC-R32-TR-F1".

- **Si IV**. As seen in the last panel of FIGURE 4.11, Si IV is one of those ions sensitive to the different cooling floors. In the bottom plot we see how the F1 models remain at $< N >_{\text{SiIV}} > 10^{15-2}$ throughout the entire evolution; while, the F2 models, starting at ~ 2 Myr exhibit a continuous decline of to $< N >_{\text{SiIV}}>$. As also for C III, H I and N V, in the F2 models it is possible to appreciate, the differences caused by the different orientation of the magnetic field, but for Si IV, this occurs later (after ~ 2 Myr), with the "-TR" model having 1 dex. higher column number densities of Si IV than its "-AL" counterpart. Since Si IV is tracer of warm gas in the clouds, as it disappears from the volume, $< N >_{\text{SiIV}}>$ also drops dramatically in the F2 models.

From this spectral analysis we have seen that each ion chosen to study individual cloud evolution has a different sensitivity to the set-up cooling floor and the initial magnetic field orientation. Excellent tracers of atomic warm and cold clouds are C III, H I, Mg II, N V, and Si IV, where the ability of the gas to condense down to 50 K causes the column number density of these ions to increase or remain constant over time in F1 models than in the F2 models. Some of these ions, such as C III, H I, N V, and Si IV, also trace differences in the plots of FIGURE 4.11, depending on the orientation of the magnetic field. When the magnetic field is transverse to the wind direction, it keeps the cloud more compact and with higher values of the column number density of these ions, compared to the counterpart with magnetic field aligned to the wind. On the other hand, for the F1 models, it is not possible to distinguish differences caused by the magnetic field during the lifetime of our simulations. Probably simulations lasting longer than 4 Myr and with larger volumes can give different results. Finally, some elements such as Ne VIII and O VI do not seem to be particularly sensitive to different atomic cloud evolution, with both ions providing very limited information about the cooling floor and magnetic field. O VI, however, in our simulations has been shown to be an excellent tracer of the galactic wind;

this element, in fact, seems to be a good indicator of star formation and stellar mass in galaxies, as reported in Tchernyshyov et al. [2021].
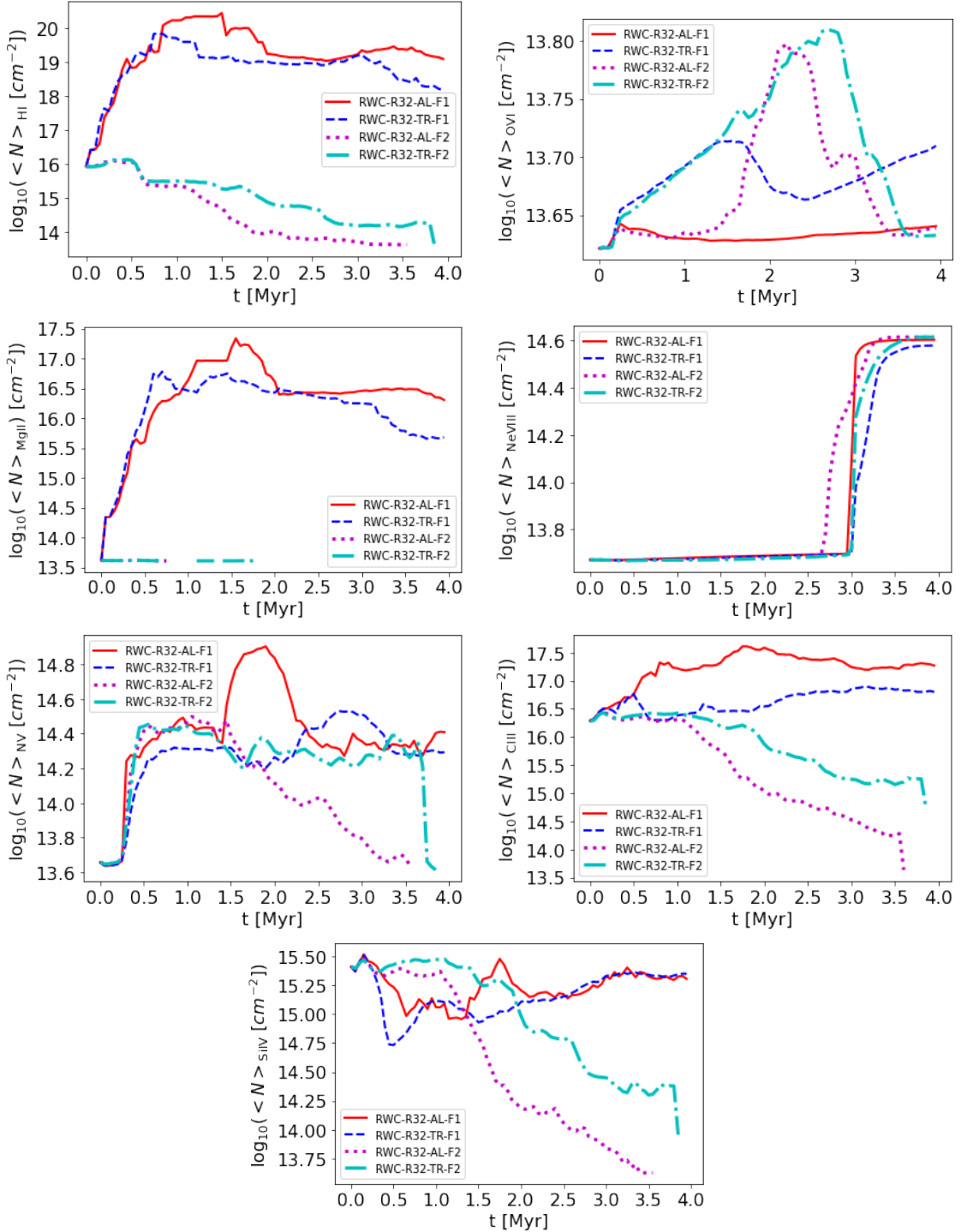

Figure 4.11: Time evolution of average ion column densities of individual ions in the wind-cloud models. Starting at the top left we find H I, O VI, Mg II, Ne VIII, N V, C III, and Si IV. Models are shown with the same color code as FIGURE 4.6: red for RWC-R32-AL-F1, blue for RWC-R32-TR-F1, purple for RWC-R32-AL-F2, and green for RWC-R32-TR-F2.

4.3 Application to a shock-multicloud model

In this section we examine the second type of simulation consisting on a shock-multicloud system. As done in the previous section, we start, in section 4.3.1, with the study of the morphology of the multicloud layer during the interaction with the galactic wind and the trend analysis of some diagnostics. Subsequently, in section 4.3.2, we focus on producing spectra, in order to demonstrate the flexibility of our tool, and on quantifying the average densities of the same elements seen for the wind-cloud models. Also in this case computing number density constraints for the various ions is crucial for comparison with observations in order to understand how different physical processes influence the ions that track warm and cold gas detection of cold gas with velocities of hundreds of km s^{-1} in the CGM.

4.3.1 EVOLUTION OF A SHOCK-MULTICLOUD SYSTEM

In this section we describe the evolution of the shock-multiclod system model and also what the trends of some diagnostics are, e.g., the total mass of clouds, their number density, temperature and mixing fraction (see FIGURE 4.14). For the first part of this description we use the following papers as a reference (Banda-Barragán et al. [2020] and Banda-Barragán et al. [2021]), since our model has the same initial conditions of Banda-Barragán et al. [2021] but a volume three times large.

In this simulation we can find the four phases described in Banda-Barragán et al. [2020]: (1) Initial contact and shock splitting; (2) Cloud layer compression and shock steady crossing; (3) Cloud expansion and shock re-acceleration; and (4) Cloud mixing and turbulence emergence. The model reported in this thesis also takes into account radiative cooling as in Banda-Barragán et al. [2021]. However, since the box is larger, we can observe the evolution of the clouds up to 1750 pc from the starting position. Below, we provide a more detailed description of the different phases involved in the evolution of radiative shock-multicloud systems:

- **Initial contact and shock splitting**. Initially the multicloud layer, before being impacted by the shock, starts cooling down (first trend observed in the top-right panel of FIGURE 4.14). As soon as the shock hits the cloud, it transfers part of its thermal energy to the multicloud layer. This contact causes an increase in temperature of the multicloud layer being shocked, which from being cold with $T < 10^4$ K, becomes warm, with $T > 10^5$ K (as can be seen in the temperature plot of FIGURE 4.14).

- **Cloud layer compression and shock steady crossing**. The transmission of the shock within the multicloud layer generates cloud compression, which consequently causes strong cooling capable to remove part of the thermal energy transmitted by the shock. This phase lasts up to ~ 0.25 Myr, and, as can be observed in the top-left panel of FIGURE 4.14, the number density of the multicloud layer increases, while
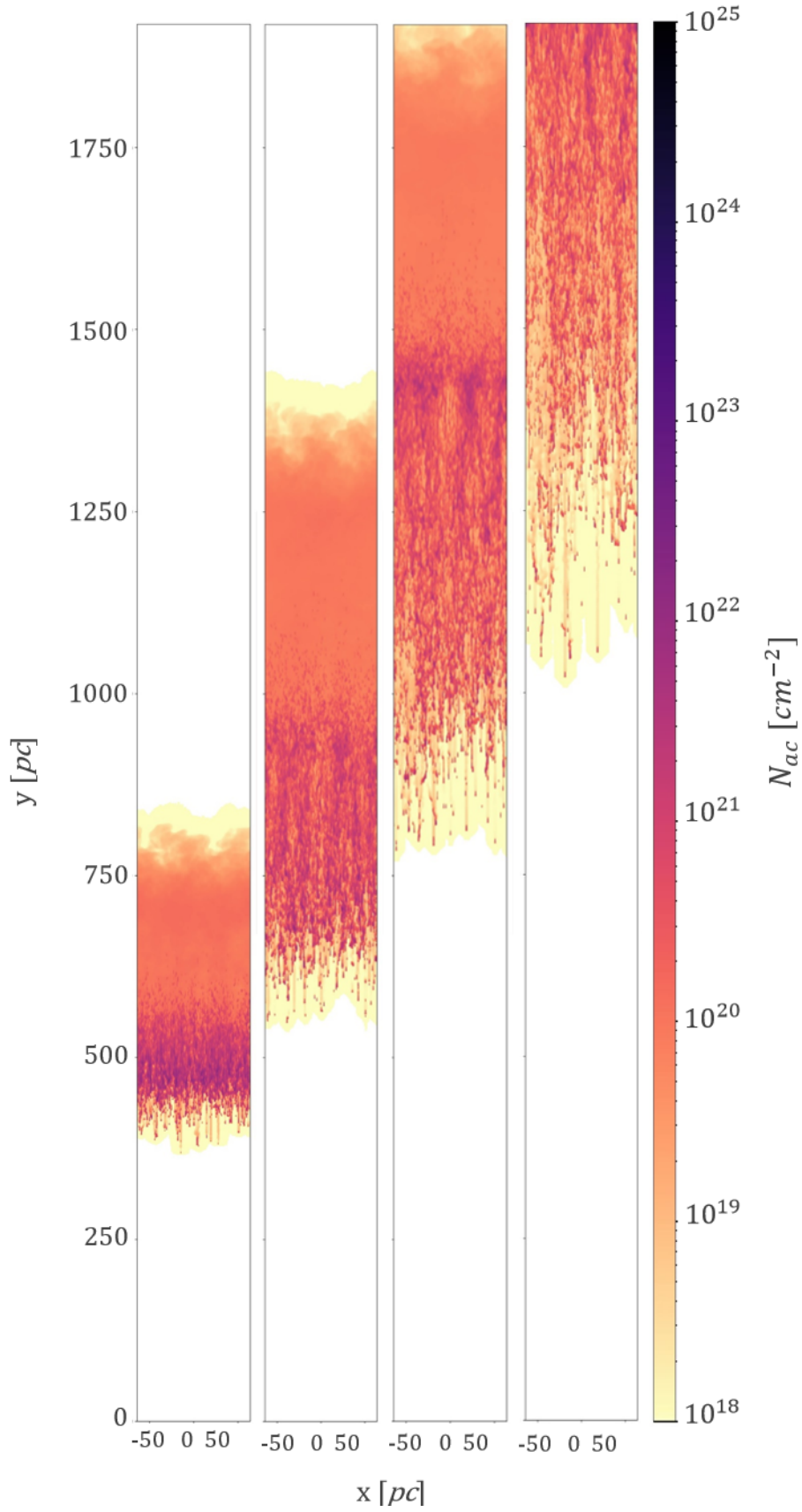
its

Figure 4.12: Evolution of edge-on column density projected along the z-axis, in the shock-multicloud model. From left to right, the four panels are made at $t = 0.6$ Myr, $t = 1.2$ Myr, $t = 1,8$ Myr and at $t = 2.5$ Myr.
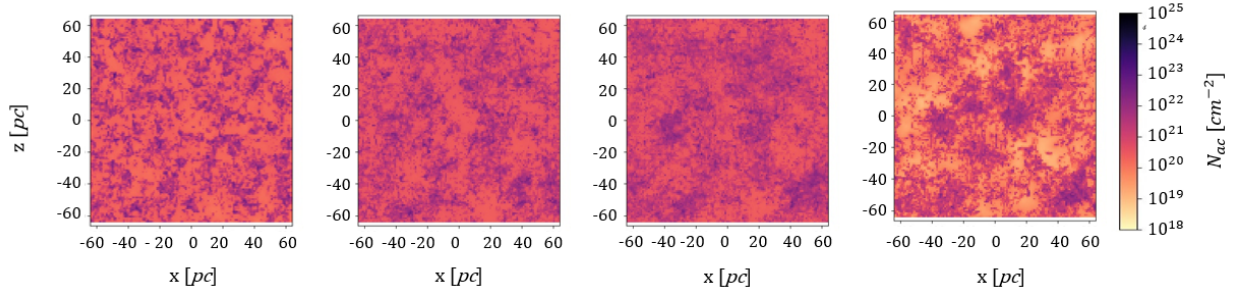
Figure 4.13: Evolution of down-the-barrel column density projected along the y-axis, in
the shock-multicloud model. From left to right, the four panels are made at
$t = 0.6\,\mathrm{Myr}$, $t = 1.2\,\mathrm{Myr}$, $t = 1,8\,\mathrm{Myr}$ and at $t = 2.5\,\mathrm{Myr}$.

temperature decreases (see temperature plot of FIG 4.14).

- **Clouds expansion and shock re-acceleration**. Once the shock has crossed all the
  multicloud layer it regains speed as it finds a less dense medium. The wind, in its
  flow, drags most of the medium of the multicloud layer with it. For this reason,
  clouds are stretched and filaments emerge. Since these cloudlets have acquired
  momentum from the wind, they move upwards. The clouds undergoing a vertical
  stretching are also more exposed to KH instability. However, the cooling leads to
  fragmentation and clumping of the dense gas (see Gronke & Oh [2020]), as we can
  already see in the first panel of FIGURE 4.13 and FIGURE 4.12.

- **Cloud mixing and turbulence emergence**. After about 0.4 Myr we have a multi-
  cloud system consisting of clouds with long tails that, rather than evaporating due
  to RT and KH instabilities, they condense and remain compact (as also seen in ra-
  diative wind-cloud models of section 4.2). This trend can be seen in the number
  density plot of FIGURE 4.14, where the material belonging to the clouds becomes
  less dense over time with a gentle decreasing trend. The clouds undergo constant
  erosion; the wind carries downstream the material belonging to the outer layers
  of the newly formed filaments, and, as a consequence, the tails increase in length.
  Therefore, the multicloud layer assumes a rain-like configuration that is preserved
  for the full duration of the simulation. The stretching of the tails, however, ex-
  poses them to KH instabilities, which make the downstream medium turbulent and
  favour the continuous mixing between cloud material and the outer medium. This
  is confirmed by both the bottom-left panel of FIG 4.14, where the material, once the
  maximum value of 1 is reached, forms a plateau; and also by the panels of FIGURE
  4.13, where the low and high column number density regions change continuously
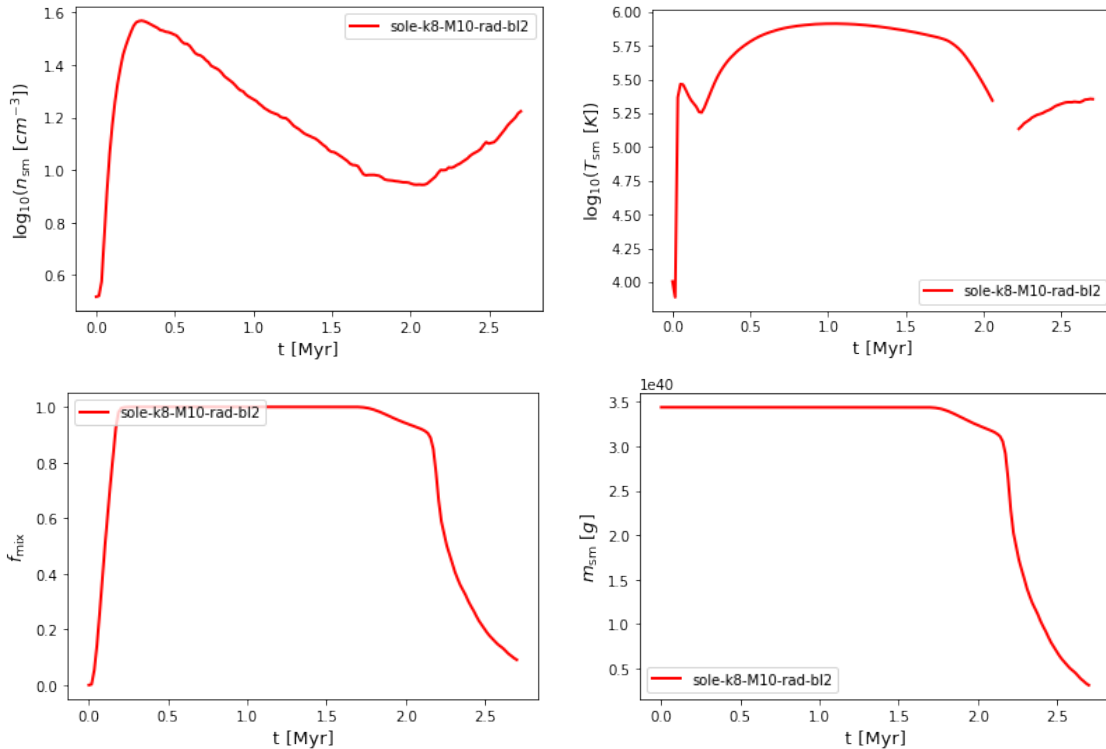 in the x-z plane.

Figure 4.14: Diagnostics time evolution for the shock-multicloud model. The top left panel, shows the number density, the top right panel reports the temperature, the bottom left plot shows the mixing fraction, and the bottom right, the mass.

With this first analysis of the shock-multicloud system we find the same conclusions reported in Banda-Barragán et al. [2021], and confirm that dense gas is continuously recycled throughout the evolution of these systems. Radiative processes quickly counteract the evaporation of the clouds, thus extending the lifetime of dense gas. In addition, the material belonging to the clouds becomes more turbulent (see Ji et al. [2019] and Mandelker et al. [2020]); so, it mixes and recondenses again creating new dense gas, even at large distances from the starting point (see Gronke & Oh [2018], Gronke & Oh [2020], and Banda-Barragán et al. [2021]).

The simulation analyzed in this thesis adds more information to the previous ones. What we can say from FIGURE 4.12 and FIGURE 4.13 is that, dense gas cloudlets and filaments survive for at least 3 Myr, but at the same time the material stripped and heated by the galactic wind recondenses again thanks to cooling. The identity of the primordial cloudlets is actually lost during the evolution. The densest parts of the cloudlets are also eroded as revealed by our mixing fraction calculations, but to study their thermal history, we would need to add additional tracers. The cold gas that reaches the smallest distances in the last panel of FIGURE 4.13 and accelerates less, compared to the downstream material in the tails is also gas that has reformed via condensation, but initially belonged to the regions further upstream in the multicloud layer. At about 1.7 Myr the material, which primordially belonged to the multicloud layer, reaches the top side of the compu-

tational domain and starts to exit it, also evidenced by the decrease in cloud mass in the bottom right panel of FIG 4.14. This material is not as dense as the upstream material. In fact, as shown in the top left panel of FIG 4.14, the number density of the cloud begins to increase slightly as less dense gas exits the box. The increasing trend in density continues until even the densest and most upstream footpoins exit the simulation volume, after 3 Myr. With this simulation we can confirm that it is possible to find dense material up to thousands of pc from the starting position of the multicloud layer, which observationally would correspond to regions near the clouds. These clouds of cold gas have velocities of a few hundred km/s as momentum is efficiently transmitted by the post-shock flow to the mixed phase via ram pressure. Quantifying their velocity distribution, especially after 0.6 Myr (maximum time of Banda-Barragán et al. [2021]), will be the subject of future works. On the other hand, as highlighted in Banda-Barragán et al. [2021], after traveling $100 - 200$ pc from the initial position, the clouds have a velocity of $\sim 200 - 300$ km s^{-1}, comparable with the values found by observations, e. g., McClure-Griffiths et al. [2013].

4.3.2   ABSORPTION SPECTRA IN OUR SHOCK-MULTICLOUD MODEL

The goal of this subsection is to verify the versatility of the PLUTO-Trident tool created for producing column density maps and spectra of ions. In addition, we also try to understand how the average column number density of each ion, the same as in the wind-cloud model, varies during the evolution of the multicloud layer. Following the structure of subsection 4.2.2, we start by studying the thermodynamics of the simulation with 2D histograms of the number density and the temperature. We then report column density maps of H I and O VI from different angles. In this first part, for both the 2D histogram and the column number density maps, we consider the shock-multicloud system snapshot at $t \sim 1.9$ Myr. Afterwards, always for $t \sim 1.9$ Myr, we have produced a down-the-barrel spectrum with the ray starting at coordinate point $(30, 0, 30)$ and ending at $(30, 1920, 30)$ both in code units. Finally, in the last subsection we analyse how the time evolution of the column number density of each ion, integrated along the y-axis and averaged over the x-z plane, is affected by the initial conditions and post-shock flow to the mixed phase reported in 4.3.1.

4.3.2.1   2D histograms of number density versus temperature for our shock-multicloud model

In this section we show a 2D histogram with the multicloud layer number density on the x-axis and temperature on the y-axis derived from data at $t \sim 1.9$ Myr (see FIGURE 4.15). We produced histograms for each time step, however, we only show one of the histograms in this thesis, the one at $t \sim 1.9$ Myr, as this is the snapshot we use to run Trident for the production of number density maps and the generation of spectra. From this histogram we can see that the system, during its evolution, covers a large range of number densities and temperatures. We can also see three accumulation areas of gas,

one at $T \sim 10^4$ K, another at 50 K, and the last one at $10^6 - 10^7$ K. In the first pooling zone, the gas has number densities in the range $-1 < \log_{10} n \ [cm^{-3}] < 1$, while in the accumulation area at 50 K, the gas has $-1 < \log_{10} n \ [cm^{-3}] < 1$. We see there is not much gas with intermediate temperatures between 10^4 K and 50 K. This is because the cooling function, which goes with n^2, is very efficient at high densities; while the heating function, which scales with n, is not able to prevent dense gas from cooling directly to the cooling floor, thus keeping a stable intermediate warm phase at 10^4 K.

Since the range of density and temperature is similar to the single cloud systems, we chose the same ions as in section 4.2.2 to produce the synthetic spectra, namely: C III, H I, Mg II, Ne VIII, N V, O VI, and Si IV.
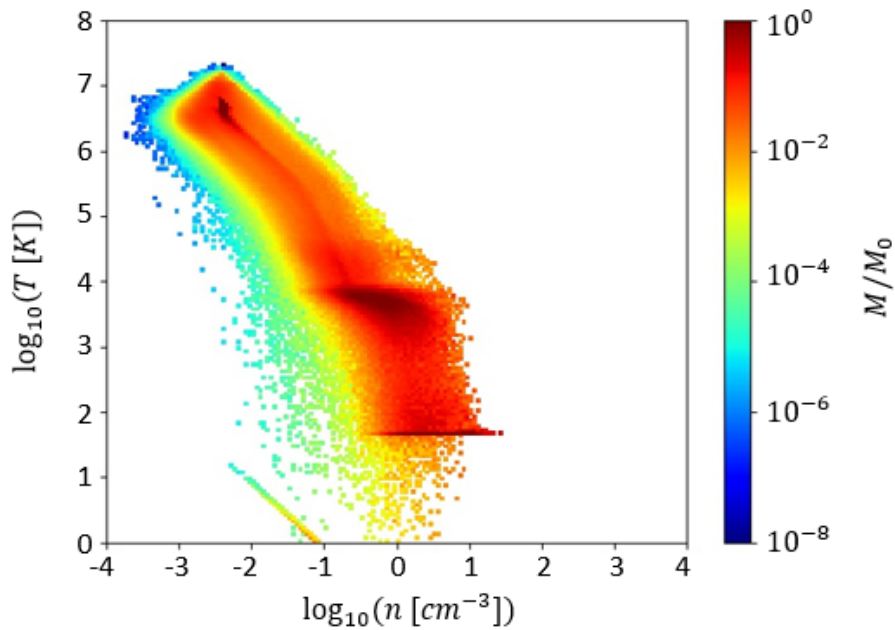

Figure 4.15: 2D histogram with number density and temperature of the shock-multicloud model at $t = 1.9$ Myr.

4.3.2.2 N_{HI} maps of our shock-multicloud model

In FIGURE 4.8 the column number density of the H I, projected along the z-axis and y-axis, respectively, at $t \sim 1.9$ Myr, is shown. Also in this case, as with the wind-cloud models, the H I covers a large range of column number densities $10^{10} < N_{HI} \ [cm^{-2}] < 10^{20}$. Furthermore, for both edge-on and down-the-barrel projection, H I is an excellent tracer for the multicloud layer, since it is not present in cells occupied only by the external post-shock flow. H I appears to be denser in the footpoints of the filaments formed by shock passage. It rather seems denser in regions that condensed following efficient mixing. Moreover, an accumulation of H I is present in the downstream region of the multicloud layer, where the tail material recondenses. Thus, we conclude that by using H I, which is a primary tracer of dense regions, it is possible to understand how cold gas in the

multicloud layer continues to exist even after ~ 1.9 Myr from interaction with a wind.
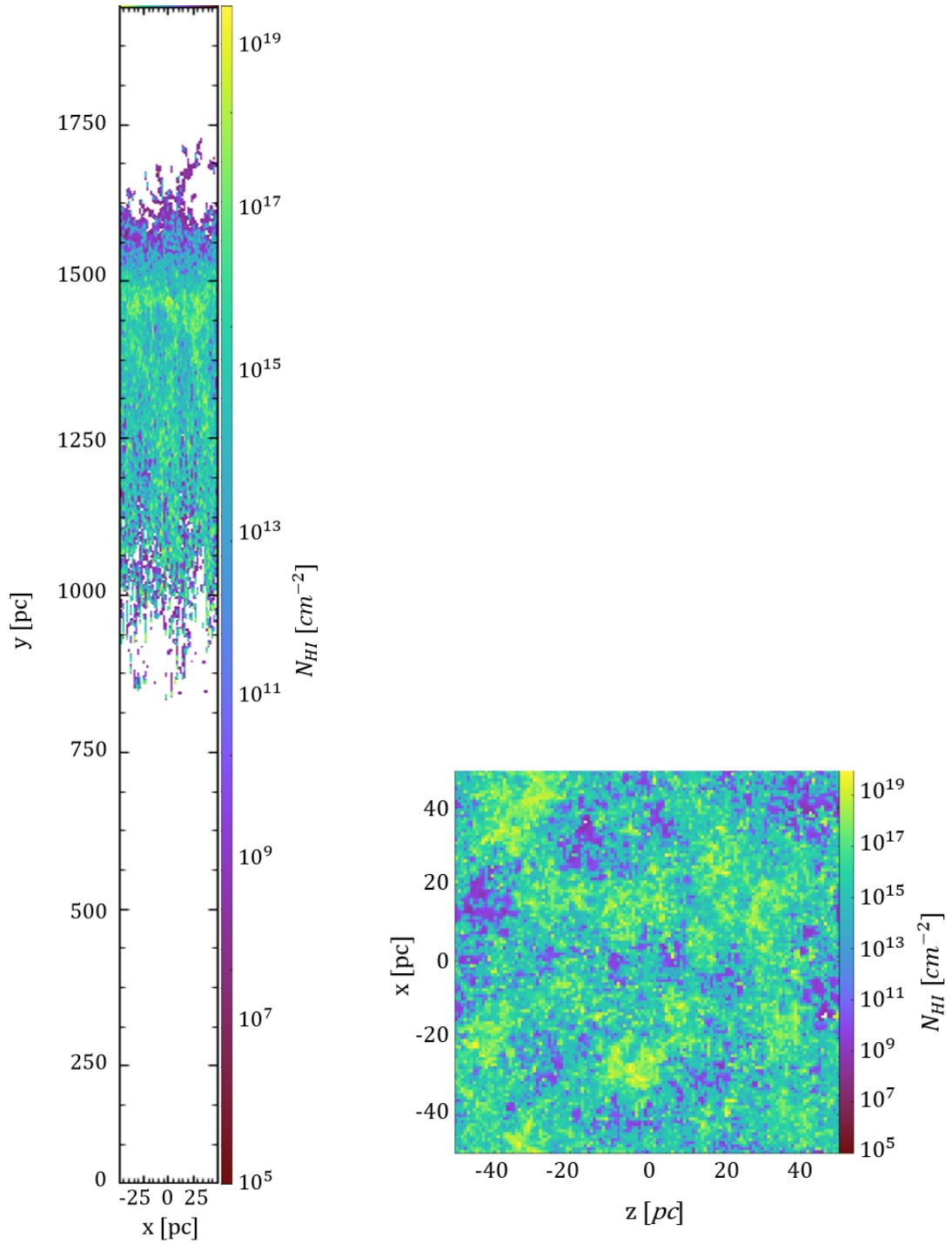

Figure 4.16: H I column number density in the shock-multicloud model at $t = 1.9$ Myr, computed with Trident. The column number densities are integrated along the z-axis in the left panel, and along the y-axis in the right plot.
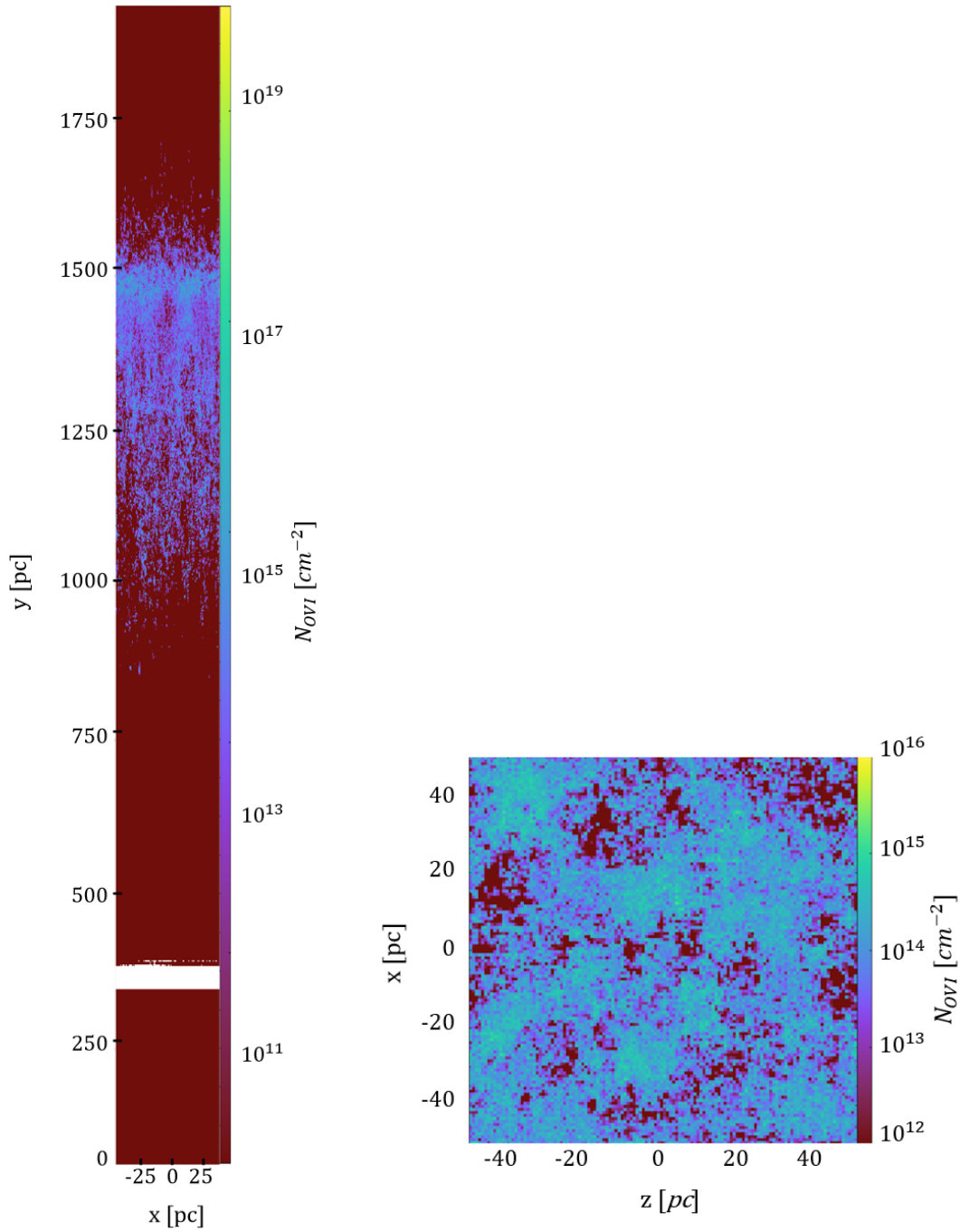
Figure 4.17: O VI column number density in the shock-multicloud model at $t = 1.9$ Myr, computed with Trident. The column number densities are integrated along the z-axis in the left panel, and along the y-axis in the right plot.

4.3.2.3 N_{OVI} **maps of our shock-multicloud model**

FIGURE 4.17 shows the column number density of O VI projected onto the x-y and x-z plane, respectively. The column number density range of O VI is smaller than HI (as also seen for wind-cloud models) and O VI is also present in the wind surrounding the cloud, but it has much lower column densities. Based on the predicted column density, it is

unlikely that O VI could be observed in the wind. What we detect in observations is more likely O VI associated with the clouds. The N_{OVI} scatter between wind and multicloud layer is at most $\sim 2 - 3$ orders of magnitude, in both the edge-on and down-the-barrel maps. The different H I and O VI patterns, observed at this time step, could also have implications for the temporal distribution of the mean column number densities, as we have also seen happening for the wind-clouds models.

4.3.2.4   Down-the-barrel spectrum at $t \sim 1.9$ Myr

The spectrum shown in FIGURE 4.18 is made at $t \sim 1.9$ Myr, by using a ray whose start and end coordinates, in pixel, are $(30, 0, 30)$ and $(30, 1920, 30)$, respectively. From the spectrum, the most visible ions are: the H I, from the Lyman series, among which the most marked lines are the *Lyα* and the *Lyβ*; the C III, the Si IV; and, finally, the doublet of the O VI and the N V. From a computational perspective, this result confirms how flexible our tool is and how it can be applied to several systems at different scales.

   From the down-the-barrel maps of column number density we can see how the column densities of the various ions can change enormously depending on the choice of the start and end point of the ray. In order to have a more statistically significant result to compare with other simulations and especially observations, it is necessary to average the chemical abundances of the ions over the entire x-z plane and see how they evolve over time. A first quantitative analysis is given in the next section, where, as in the wind-cloud models, we studied the time evolution of the column number densities of our ions averaged over the entire x-z plane, taking into account only the cells in the plane with $N_{ion} > 10^{12}$ cm^{-2}. However, owing to time constraints, we leave the analysis of other rays for future work.
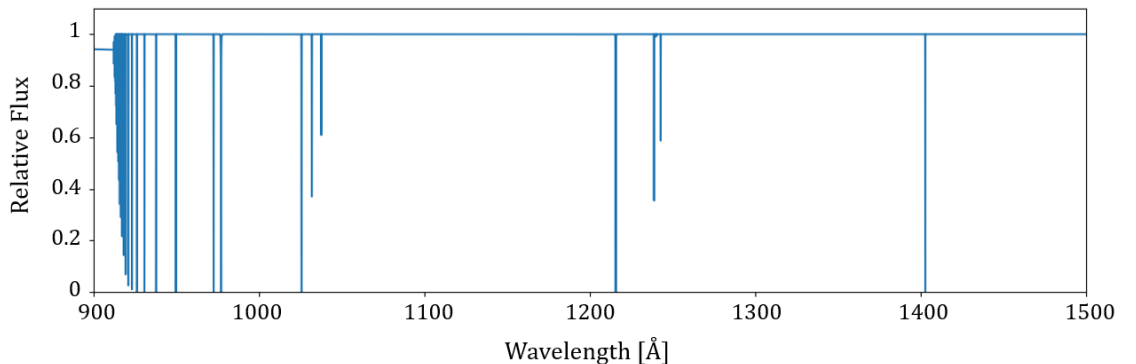

Figure 4.18: Down-the-barrel spectrum of the shock-multicloud model made with Trident. The spectrum is produced with a ray starting from $(30, 0, 30)$, ending at $(30, 1929, 30)$, both in code units, and at $t = 1.9$ Myr.
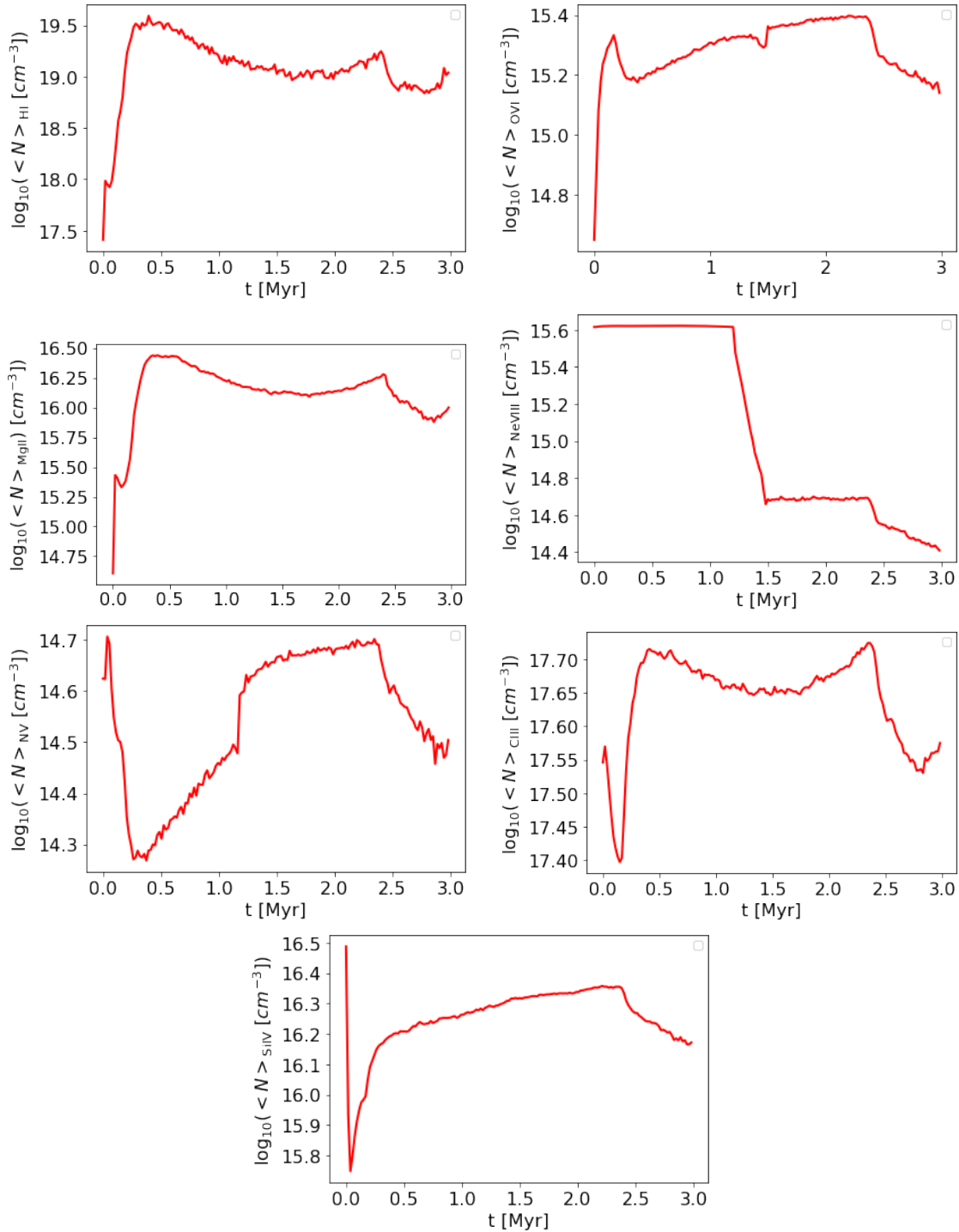
4.3.2.5 Time evolution of $< N >_{ions}$ in our shock-multicloud model

Figure 4.19: Time evolution of average ion column densities of individual ions in shock-multicloud model. Starting at the top left we find H I, O VI, Mg II, Ne VIII, N V, C III, and Si IV.

In this section we look at the time evolution of the column number densities of various ions averaged in the x-z plane. Trends in $< N >_{ions}$ are shown in FIGURE 4.19. The

goal of this section is to have an overview of which ions we would expect to detect when studying shock-multicloud systems and to understand how their concentrations change over time.

We provide below a description of the time evolution plots in FIGURE 4.19:

- **H** I. H I also has a trend similar to C III; after an initial growth, $< N >_{\mathrm{HI}}$ reaches a plateau around $10^{19.0} - 10^{19.5}$ cm^{-2}. However, when $t \sim 2.3$ Myr, a decline is also observed for H I due to the exit of gas from the computational domain. H I also remains pretty much constant, implying that H I is ubiquitous in this kind of outflows.

- **O** VI. $< N >_{\mathrm{OVI}}$, once the mixing fraction shown in FIGURE 4.14 reaches values around 1, assumes a constant trend $\sim 10^{15.2} - 10^{15.4}$ cm^{-2}. Finally, as in all other cases, a final decrease is perceived for O VI, which, however, is not as drastic as, for example, for H I, as O VI is a warmer gas tracer.

- **Mg** II. As seen for the previous two ions, Mg II can also be considered a good tracer of the multicloud layer. $< N >_{\mathrm{MgII}}$ grows with time until it reaches a plateau with values in the range $\sim 10^{16} - 10^{16.5}$ cm^{-2} after 0.5 Myr. Again, there is a drop due to gas leaving the simulation volume starting at 2.3 Myr.

- **Ne** VIII. $< N >_{\mathrm{NeVIII}}$ has a completely different trend than the previous ions. In fact, its value is always constant at $10^{15.6}$ cm^{-2} until $t \sim 2.3$ Myr. At this point it undergoes a sudden drop of an order of magnitude, and then remains constant at $< N >_{\mathrm{NeVIII}} \sim 10^{14.6}$ cm^{-2}. Finally, at $t \sim 2.3$ Myr the concentration of Ne VIII also declines, as gas is exiting the simulation box.

- **N** V. The increase in n caused by the shock passage through the multicloud layer, causes a decrease in $< N >_{\mathrm{NV}}$ to values $< 10^{14.3}$ cm^{-2}. Subsequently, the N V concentration continues to increase until $< N >_{\mathrm{NV}} \sim 10^{14.7}$ cm^{-2}, and then declines once the gas leaves the simulation volume.

- **C** III. $< N >_{\mathrm{CIII}}$, after an initial decrease coincident with the increase in n caused by the shock passing through the multicloud layer shown in FIGURE 4.14, its concentration remains constant at $\sim 10^{17.65}$ cm^{-2}. The formation of this plateau corresponds to the phase when the gas in the multicloud layer is completely mixed with the wind (~ 1 value in the mixing fraction plot in FIGURE 4.14). Subsequently, $< N >_{\mathrm{CIII}}$ drops, as a result of the multicloud layer escaping from the computational domain.

- **Si** IV. $< N >_{\mathrm{SiIV}}$ undergoes an initial decrease coinciding with the small increase in T in FIGURE 4.14, caused by the contact of the multicloud layer with the shock. Once the shock crosses the multicloud layer, however, $< N >_{\mathrm{SiIV}}$ remains constant at values between $10^{16.2} - 10^{16.4}$ cm^{-2}. We also found this plateau trend for CIII, H I,

Mg II and O VI, and, as with the previous ions, it stops as soon as the multicloud gas begins to leave the box.

In this section, we can conclude that elements such as C III, H I, Mg II, O VI, and Si IV are good candidates for studying the properties of the multicloud layer swept by galactic winds. On the other hand, Ne VIII and N V depend much more on the stage of evolution of the system. Constant values of $< N >_{ions}$, for these ions, indicate that the gas has mixed completely with the wind, and so they are good tracers of the mixed phase. Then, the presence of cold gas at large distances mainly originates from the cyclic cooling and mixing of the gas belonging to the multicloud layer, which is ripped, heated up, and then condenses again. In the future we will pursue the full chemical analysis of shock-multicloud systems. We will produce down-the-barrel spectra averaged over the whole x-z plane, and not just passing through a single point. In that manner, we will be able to set some constraints on the ion column densities and optical depths, which we can also compare with observations of starburst or general star-forming galaxies with outflows.

Chapter 5

Conclusion

The study of galactic winds plays a central role in our understanding of galaxy evolution. In particular, galactic winds probe how star formation feedback regulates the mass content and metallicity of galaxies (see Chapter 1 for further details). Galactic winds have warm and cold gas components embedded within a much hotter outflow. Such warm and cold phases are observable via emission or absorption lines. Absorption lines are one of the primary tools for studying the properties of galactic winds, both in the local and distant Universe. This cold gas component of the wind is observed at hundreds to thousands of pc from the galactic plane of their host galaxies and it is generally moving at velocities of hundreds of km s^1. Given that observations provide only a projected view of galactic winds, which in reality are complex 3D structures, it is crucial to study how such absorption lines are produced along galactic winds using numerical simulations and ion abundances computed with realistic starburst UV backgrounds.

Therefore, in this thesis, we investigate galactic wind simulations at different scales (see Chapter 2 for a review on galactic wind models). Firstly, we analyse high-resolution models of single atomic clouds with uniform density distributions interacting with galactic winds, considering also the effects of radiative cooling and magnetic fields (with configurations based on Banda-Barragán et al. [2016]). In addition, we study a medium-resolution shock-multicloud system, considering radiative processes and with a volume three time bigger than in Banda-Barragán et al. [2021], in order to follow the evolution of clouds for larger distances and for longer time-scales. Both types of simulations, wind-cloud and shock-multicloud models, belong to a suite of 3D magneto/hydrodynamical simulations, produced by the PLUTO code (Mignone et al. [2007]). We have post-process them to estimate gas column densities and synthetic absorption spectra of several ion species.

5.1   A new computational framework to produce synthetic absorption lines from PLUTO simulations

To be able to extract ion information from our simulations, we first created a computational framework capable of producing synthetic spectra from galactic wind simulations. Thus, this thesis involved the development and testing of a novel PLUTO-TRIDENT interface, which allows to read in numerical datasets from the PLUTO code and post-process them using YT (Turk et al. [2011]), CLOUDY (Ferland et al. [2017]), the cloudy cooling tools (Smith et al. [2008], Smith et al. [2017]), and the Trident code (Hummels et al. [2017]). While all these tools were publicly available before the start of the project, they needed to be substantially adapted to be able to post-process PLUTO data automatically (see Chapter 3). The framework is now ready to use (see aou recent paper Casavecchia et al. [2022] for additional details). The advantage of this tool is that it is quite flexible and can be used to study the physics and chemistry of different astrophysical systems on different scales. In addition, it makes it possible to produce column density maps for individual ions and spectra with customised UV backgrounds that take into account the high star formation that occurs in a starburst galaxy, a feature not available before and also contributed by this thesis.

Apart from the code itself, the main findings of this thesis, regarding the physics of galactic winds, are listed below.

5.2   On the thermodynamics of wind-cloud and shock-multicloud models

- We analysed wind-cloud models, with two different cooling floors, 50 K (cold clouds or F1 models) and 10^4 K (warm clouds or F2 models), and two magnetic field configurations: aligned with or transverse to the direction of the wind. In all four models, the galactic wind heats up and removes the outer layers of clouds carrying them downstream. This produces tails of warm material with different morphologies depending on the initial conditions. We compared the evolution of cold and warm clouds, finding that the ability of clouds to cool down to $T = 50$ K extends their lifetime, but drastically limits their acceleration. The capacity of these clouds to maintain a limited cross section and high densities makes them less exposed to the growth of shear instabilities and consequently to evaporation.

- The different cooling floor between F1 models (set at 50 K) and F2 models (at 10^4 K) has important consequences on cloud evolution. F1 models maintain temperatures $\sim 1 - 2$ orders of magnitude lower than F2 models, and densities $\sim 2 - 3$ orders of magnitude higher. Cold clouds remain more compact, are less exposed to instabilities, and have a longer lifetime than warm clouds.

- From the column density maps of our wind-cloud we also found that warm clouds (F2 models) gain more momentum from the wind owing to their ability to expand, and manage to achieve higher velocities than cold clouds.

- Again in the wind-cloud models, we have seen that differences caused by the different orientation of the magnetic field are more appreciable in the models with the higher cooling floors (F2 models). The transverse magnetic field has the effect of creating a shield along the x-axis that prevents the clouds, in models with cooling floor at 10^4 K, from expanding along the z-axis. Then, during the interaction with the wind, these clouds have a longer lifetime.

- In our shock-multicloud model, having a simulation with volume three times larger than in the models presented in Banda-Barragán et al. [2021] allowed us to analyse the evolution of the multicloud layer over a longer period of time. In this case the post-shock flow (i.e., the wind) has a temperature of $T_{wind} \sim 10^7$ K, higher than in the wind-cloud models. From the column number density maps of this model, we found that dense gas survives for the entire duration of the simulation as cold gas is continuously created throughout the volume from the (re)condensation of mixed gas ripped from clouds and heated up by the wind. This thesis confirms what was reported in Banda-Barragán et al. [2021]; cold gas observed in galactic winds originates from gas continuously recycled. Some of it originally belongs to the wind while some is initially part of the multicloud layer, which is heated up, evaporated, mixed, and then it re-condenses again, once it reaches temperatures at which radiative cooling via atomic species is efficient.

5.3 On the chemistry and ion population of wind-cloud and shock-multicloud models

- In wind-cloud models, the different initial cooling floors and magnetic fields also have implications for the average column number densities of several ion species. We find that the elements that best track the evolution of clouds are: C III, H I, Mg II, and Si IV. In our average column density maps, these ions are the most sensitive to the cooling floor, showing higher abundances in the case where the cooling floor is set to 50 K than in the models with cooling floors set to 10^4 K (up to three orders of magnitude larger, for example, in the case of H I). For the same ions, in models with cooling floor at 10^4 K, it is possible to appreciate differences related also to the magnetic field. In these models, the simulation with a transverse magnetic field exhibits average values of $< N >_{ions}$ up to an order of magnitude larger than its counterpart with an aligned magnetic field.

- Again, for wind-cloud models, O VI is observable both in cells occupied by gas belonging to clouds and cells occupied by the hot wind. It can also be used for

distinguishing clouds with cooling floors at 50 K and clouds with cooling floors at 10^4 K.

- For the shock-multicloud models, C III, H I, Mg II, O VI, and Si IV ions are tracers of the multicloud layer, and their average column densities have approximately constant trends for most of the evolution of this simulations. This also reflects the constant value of mixing fraction close to 1 of these systems, which indicates that, after ~ 0.3 Myr much of the gas belonging to the multicloud layer has mixed with the galactic wind.

5.4   Future developments

With this thesis we verified that, dense clouds interacting with galactic winds can travel hundreds and thousands of pc from the galactic plane, provided that they are part of a multicloud system. In single cloud models, travel only modest distances from their initial positions before they are dispersed, but once they are part of a conglomerate of clouds, as in our shock-multicloud models, their very destruction contributes to mixed gas that can recondense into new dense gas. The ability of clouds to cool down to 50 K increases their lifetime and, in the shock-multicloud model, where $T_{wind} \sim 10^7$ K, clouds accelerate. This result is in agreement with previous studies in which individual clouds are rapidly dispersed, except in a few scenarios, while cloud conglomerates give rise to outflows with dense components. In future work, we will quantify in detail, for the shock-multicloud model, the velocities of clouds and compare the results with those observed for example in M82 and the Milky Way.

The goal of future chemical analysis is to set limits on the ion column densities, optical depths, and covering fractions to understand how these quantities are affected by magnetic field and radiative processes, and whether or not their effects are large enough to be identifiable in spectral observations. We will compare our results with other numerical studies on the chemical evolution of wind-cloud models, such as Cottle et al. [2018], de la Cruz et al. [2021], but especially with observations such as in Tchernyshyov et al. [2021], where the SFR and stellar mass were related to O VI density in starburst galaxies.In future work, we will produce spectra and column density maps for each ion with different UV backgrounds, and, to obtain statistically significant spectral results by generating synthetic spectra with rays having different trajectories and orientations. Finally, regarding the code development, future goal will be to parallelise the routine for the production of the spectra.

5.5   Acknowledgements

5.6   Disclaimer

Sections 3.1 and 4.1 of this thesis are based on Casavecchia et al. [2022]. In particular the description of the softwares, codes and python packages used, such as: the PLUTO code (Mignone et al. [2007]), the Trident package (Hummels et al. [2017]), the YT package (Turk et al. [2011]), the CLOUDY code (Ferland et al. [2013]), the suite of CLOUDY tools (Smith et al. [2017]), the STARBURST99 software (Vázquez & Leitherer [2017]). In addition, the procedure followed to create the PLUTO-Trident interface, to produce the UV background consisting of starburst, and to generate our synthetic column density maps for each ion and synthetic spectra is also reported in Casavecchia et al. [2022].

Bibliography

Alūzas R., Pittard J. M., Hartquist T. W., Falle S. A. E. G., Langton R., 2012, *Numerical simulations of shocks encountering clumpy regions*, MNRAS, 425, 2212

Alūzas R., Pittard J. M., Falle S. A. E. G., Hartquist T. W., 2014, *Numerical simulations of a shock interacting with multiple magnetized clouds*, MNRAS, 444, 971

Anderson M. E., Bregman J. N., Dai X., 2013, *Extended Hot Halos around Isolated Galaxies Observed in the ROSAT All-Sky Survey*, ApJ, 762, 106

Anderson M. E., Churazov E., Bregman J. N., 2016, *A deep XMM-Newton study of the hot gaseous halo around NGC 1961*, MNRAS, 455, 227

Armillotta L., Fraternali F., Marinacci F., 2016, *Efficiency of gas cooling and accretion at the disc-corona interface*, MNRAS, 462, 4157

Banda-Barragán W. E., Parkin E. R., Federrath C., Crocker R. M., Bicknell G. V., 2016, *Filament formation in wind-cloud interactions - I. Spherical clouds in uniform magnetic fields*, MNRAS, 455, 1309

Banda-Barragán W. E., Federrath C., Crocker R. M., Bicknell G. V., 2018, *Filament formation in wind-cloud interactions- II. Clouds with turbulent density, velocity, and magnetic fields*, MNRAS, 473, 3454

Banda-Barragán W. E., Zertuche F. J., Federrath C., García Del Valle J., Brüggen M., Wagner A. Y., 2019, *On the dynamics and survival of fractal clouds in galactic winds*, MNRAS, 486, 4526

Banda-Barragán W. E., Brüggen M., Federrath C., Wagner A. Y., Scannapieco E., Cottle J., 2020, *Shock-multicloud interactions in galactic outflows - I. Cloud layers with lognormal density distributions*, MNRAS, 499, 2173

Banda-Barragán W. E., Brüggen M., Heesen V., Scannapieco E., Cottle J., Federrath C., Wagner A. Y., 2021, *Shock-multicloud interactions in galactic outflows - II. Radiative fractal clouds and cold gas thermodynamics*, MNRAS, 506, 5658

Beirão P., et al., 2015, *Spatially resolved Spitzer-IRS spectral maps of the superwind in M82*, MNRAS, 451, 2640

Bland-Hawthorn J., Cohen M., 2003, *The Large-Scale Bipolar Wind in the Galactic Center*, ApJ, 582, 246

Bordoloi R., et al., 2011, *The Radial and Azimuthal Profiles of Mg II Absorption around 0.5 < z < 0.9 zCOSMOS Galaxies of Different Colors, Masses, and Environments*, ApJ, 743, 10

Bowen D. V., Chelouche D., Jenkins E. B., Tripp T. M., Pettini M., York D. G., Frye B. L., 2016, *The Structure of the Circumgalactic Medium of Galaxies: Cool Accretion Inflow Around NGC 1097*, ApJ, 826, 50

Bregman J., 2007a, *Most of the Baryons in Galaxies*, XMM-Newton Proposal

Bregman J. N., 2007b, *The Search for the Missing Baryons at Low Redshift*, ARA&A, 45, 221

Brüggen M., Scannapieco E., 2016, *The Launching of Cold Clouds by Galaxy Outflows. II. The Role of Thermal Conduction*, ApJ, 822, 31

Carretti E., et al., 2013, *Giant magnetized outflows from the centre of the Milky Way*, Nat, 493, 66

Casavecchia B., Banda-Barragán W., Brüggen M., Brighenti F., 2022, in IAU S362: Predictive Power of Computational Astrophysics as a Discovery Tool.

Chandrasekhar S., 1961, *Hydrodynamic and hydromagnetic stability*

Childs H., et al., 2012, in , High Performance Visualization–Enabling Extreme-Scale Scientific Insight. pp 357–372

Chisholm J., Bordoloi R., Rigby J. R., Bayliss M., 2018, *Feeding the fire: tracing the mass-loading of 10^7 K galactic outflows with O VI absorption*, MNRAS, 474, 1688

Cimatti A., Fraternali F., Nipoti C., 2019, *Introduction to Galaxy Formation and Evolution. From Primordial Gas to Present-Day Galaxies*, arXiv e-prints, p. arXiv:1912.06216

Contursi A., et al., 2013, *Spectroscopic FIR mapping of the disk and galactic wind of M 82 with Herschel-PACS*, A&A, 549, A118

Cooper J. L., Bicknell G. V., Sutherland R. S., Bland-Hawthorn J., 2008, *Three-Dimensional Simulations of a Starburst-driven Galactic Wind*, ApJ, 674, 157

Corlies L., Schiminovich D., 2016, *Empirically Constrained Predictions for Metal-line Emission from the Circumgalactic Medium*, ApJ, 827, 148

Cottle J. N., Scannapieco E., Brüggen M., 2018, *Column Density Profiles of Cold Clouds Driven by Galactic Outflows*, ApJ, 864, 96

Crocker R. M., 2012, *Non-thermal insights on mass and energy flows through the Galactic Centre and into the Fermi bubbles*, MNRAS, 423, 3512

Crutcher R. M., Wandelt B., Heiles C., Falgarone E., Troland T. H., 2010, *Magnetic Fields in Interstellar Clouds from Zeeman Observations: Inference of Total Field Strengths by Bayesian Analysis*, ApJ, 725, 466

Dedner A., Kemm F., Kröner D., Munz C. D., Schnitzer T., Wesenberg M., 2002, *Hyperbolic Divergence Cleaning for the MHD Equations*, Journal of Computational Physics, 175, 645

Dekel A., Woo J., 2003, *Feedback and the fundamental line of low-luminosity low-surface-brightness/dwarf galaxies*, MNRAS, 344, 1131

Dekel A., Zolotov A., Tweed D., Cacciato M., Ceverino D., Primack J. R., 2013, *Toy models for galaxy formation versus simulations*, MNRAS, 435, 999

Elmegreen B. G., Scalo J., 2004, *Interstellar Turbulence I: Observations and Processes*, ARA&A, 42, 211

Fabian A., 2014, in 40th COSPAR Scientific Assembly. pp E1.5–23–14

Federrath C., Klessen R. S., Schmidt W., 2008, *The Density Probability Distribution in Compressible Isothermal Turbulence: Solenoidal versus Compressive Forcing*, ApJ, 688, L79

Ferland G. J., et al., 2013, *The 2013 Release of Cloudy*, Rev. Mex. Astron. Astrofis., 49, 137

Ferland G. J., et al., 2017, *The 2017 Release Cloudy*, Rev. Mex. Astron. Astrofis., 53, 385

Fox A. J., Wakker B. P., Savage B. D., Tripp T. M., Sembach K. R., Bland-Hawthorn J., 2005, *Multiphase High-Velocity Clouds toward HE 0226-4110 and PG 0953+414*, ApJ, 630, 332

Fragile P. C., Anninos P., Gustafson K., Murray S. D., 2005, *Magnetohydrodynamic Simulations of Shock Interactions with Radiative Clouds*, ApJ, 619, 327

Fukugita M., Peebles P. J. E., 2004, *The Cosmic Energy Inventory*, ApJ, 616, 643

Gardiner T. A., Stone J. M., 2008, *An unsplit Godunov method for ideal MHD via constrained transport in three dimensions*, Journal of Computational Physics, 227, 4123

Gronke M., Oh S. P., 2018, *The growth and entrainment of cold gas in a hot wind*, MNRAS, 480, L111

Gronke M., Oh S. P., 2020, *How cold gas continuously entrains mass and momentum from a hot wind*, MNRAS, 492, 1970

Grønnow A., Tepper-García T., Bland-Hawthorn J., McClure-Griffiths N. M., 2017, *Magnetized High Velocity Clouds in the Galactic Halo: A New Distance Constraint*, ApJ, 845, 69

Gupta A., Mathur S., Krongold Y., Nicastro F., Galeazzi M., 2012, *A Huge Reservoir of Ionized Gas around the Milky Way: Accounting for the Missing Mass?*, ApJ, 756, L8

Gutcke T. A., Stinson G. S., Macciò A. V., Wang L., Dutton A. A., 2017, *NIHAO - VIII. Circum-galactic medium and outflows - The puzzles of H I and O VI gas distributions*, MN-RAS, 464, 2796

Haardt F., Madau P., 2012, *Radiative Transfer in a Clumpy Universe. IV. New Synthesis Models of the Cosmic UV/X-Ray Background*, ApJ, 746, 125

Hayes M., Melinder J., Östlin G., Scarlata C., Lehnert M. D., Mannerström-Jansson G., 2016, *O VI Emission Imaging of a Galaxy with the Hubble Space Telescope: a Warm Gas Halo Surrounding the Intense Starburst SDSS J115630.63+500822.1*, ApJ, 828, 49

Heckman T. M., Thompson T. A., 2017, *Galactic Winds and the Role Played by Massive Stars*, arXiv e-prints, p. arXiv:1701.09062

Henry A., Scarlata C., Martin C. L., Erb D., 2015, *Lyα Emission from Green Peas: The Role of Circumgalactic Gas Density, Covering, and Kinematics*, ApJ, 809, 19

Hoopes C. G., et al., 2005, *GALEX Observations of the Ultraviolet Halos of NGC 253 and M82*, ApJ, 619, L99

Hummels C. B., Bryan G. L., Smith B. D., Turk M. J., 2013, *Constraints on hydrodynamical subgrid models from quasar absorption line studies of the simulated circumgalactic medium*, MNRAS, 430, 1548

Hummels C. B., Smith B. D., Silvia D. W., 2017, *Trident: A Universal Tool for Generating Synthetic Absorption Spectra from Astrophysical Simulations*, ApJ, 847, 59

Ji S., Oh S. P., Masterson P., 2019, *Simulations of radiative turbulent mixing layers*, MNRAS, 487, 737

Jones T. W., Kang H., Tregillis I. L., 1994, *Cosmic Bullets as Particle Accelerators and Radio Sources*, ApJ, 432, 194

Jones T. W., Ryu D., Tregillis I. L., 1996, *The Magnetohydrodynamics of Supersonic Gas Clouds: MHD Cosmic Bullets and Wind-swept Clumps*, ApJ, 473, 365

Kaviraj S., et al., 2017, *The Horizon-AGN simulation: evolution of galaxy properties over cosmic time*, MNRAS, 467, 4739

Kereš D., Hernquist L., 2009, *Seeding the Formation of Cold Gaseous Clouds in Milky Way-Size Halos*, ApJ, 700, L1

Kim C.-G., Ostriker E. C., 2018, *Numerical Simulations of Multiphase Winds and Fountains from Star-forming Galactic Disks. I. Solar Neighborhood TIGRESS Model*, ApJ, 853, 173

Krumholz M. R., Dekel A., 2012, *Metallicity-dependent Quenching of Star Formation at High Redshift in Small Galaxies*, ApJ, 753, 16

Larson R. B., 1981, *Turbulence and star formation in molecular clouds.*, MNRAS, 194, 809

Lehner N., Staveley-Smith L., Howk J. C., 2009, *Properties and Origin of the High-Velocity Gas Toward the Large Magellanic Cloud*, ApJ, 702, 940

Lehner N., Howk J. C., Wakker B. P., 2015, *Evidence for a Massive, Extended Circumgalactic Medium Around the Andromeda Galaxy*, ApJ, 804, 79

Lehnert M. D., Heckman T. M., Weaver K. A., 1999, *Very Extended X-Ray and Hα Emission in M82: Implications for the Superwind Phenomenon*, ApJ, 523, 575

Leroy A. K., et al., 2015, *The Multi-phase Cold Fountain in M82 Revealed by a Wide, Sensitive Map of the Molecular Interstellar Medium*, ApJ, 814, 83

Lu Y., Blanc G. A., Benson A., 2015, *An Analytical Model for Galaxy Metallicity: What do Metallicity Relations Tell Us about Star Formation and Outflow?*, ApJ, 808, 129

Mandelker N., Nagai D., Aung H., Dekel A., Birnboim Y., van den Bosch F. C., 2020, *Instability of supersonic cold streams feeding galaxies - IV. Survival of radiatively cooling streams*, MNRAS, 494, 2641

Martin C. L., 2005, *Mapping Large-Scale Gaseous Outflows in Ultraluminous Galaxies with Keck II ESI Spectra: Variations in Outflow Velocity with Galactic Mass*, ApJ, 621, 227

McClure-Griffiths N. M., Green J. A., Hill A. S., Lockman F. J., Dickey J. M., Gaensler B. M., Green A. J., 2013, *Atomic Hydrogen in a Galactic Center Outflow*, ApJ, 770, L4

McCourt M., O'Leary R. M., Madigan A.-M., Quataert E., 2015, *Magnetized gas clouds can survive acceleration by a hot wind*, MNRAS, 449, 2

Mignone A., Bodo G., Massaglia S., Matsakos T., Tesileanu O., Zanni C., Ferrari A., 2007, in JENAM-2007, "Our Non-Stable Universe". pp 96–96

Miller M. J., Bregman J. N., 2016, *The Interaction of the Fermi Bubbles with the Milky Way's Hot Gas Halo*, ApJ, 829, 9

Miyoshi T., Kusano K., 2005, in AGU Fall Meeting Abstracts. pp SM51B–1295

Muratov A. L., Kereš D., Faucher-Giguère C.-A., Hopkins P. F., Quataert E., Murray N., 2015, *Gusty, gaseous flows of FIRE: galactic winds in cosmological simulations with explicit stellar feedback*, MNRAS, 454, 2691

Muratov A. L., et al., 2017, *Metal flows of the circumgalactic medium, and the metal budget in galactic haloes*, MNRAS, 468, 4170

Murray N., Quataert E., Thompson T. A., 2005, *On the Maximum Luminosity of Galaxies and Their Central Black Holes: Feedback from Momentum-driven Winds*, ApJ, 618, 569

Nelson D., Vogelsberger M., Genel S., Sijacki D., Kereš D., Springel V., Hernquist L., 2013, *Moving mesh cosmology: tracing cosmological gas accretion*, MNRAS, 429, 3353

Oppenheimer B. D., Davé R., 2008, *Mass, metal, and energy feedback in cosmological simulations*, MNRAS, 387, 577

Oppenheimer B. D., Davé R., Kereš D., Fardal M., Katz N., Kollmeier J. A., Weinberg D. H., 2010, *Feedback and recycled wind accretion: assembling the z = 0 galaxy mass function*, MNRAS, 406, 2325

Oppenheimer B. D., et al., 2016, *Bimodality of low-redshift circumgalactic O VI in non-equilibrium EAGLE zoom simulations*, MNRAS, 460, 2157

Peek J. E. G., Ménard B., Corrales L., 2015, *Dust in the Circumgalactic Medium of Low-redshift Galaxies*, ApJ, 813, 7

Peeples M. S., Werk J. K., Tumlinson J., Oppenheimer B. D., Prochaska J. X., Katz N., Weinberg D. H., 2014, *A Budget and Accounting of Metals at z ~0: Results from the COS-Halos Survey*, ApJ, 786, 54

Predehl P., et al., 2020, *Detection of large-scale X-ray bubbles in the Milky Way halo*, Nat, 588, 227

Putman M. E., Peek J. E. G., Joung M. R., 2012, *Gaseous Galaxy Halos*, ARA&A, 50, 491

Rauch M., Becker G. D., Haehnelt M. G., Gauthier J.-R., Ravindranath S., Sargent W. L. W., 2011, *Filamentary infall of cold gas and escape of Lyα and hydrogen ionizing radiation from an interacting high-redshift galaxy*, MNRAS, 418, 1115

Rubin K. H. R., Prochaska J. X., Koo D. C., Phillips A. C., 2012, *The Direct Detection of Cool, Metal-enriched Gas Accretion onto Galaxies at z ~0.5*, ApJ, 747, L26

Rubin K. H. R., Hennawi J. F., Prochaska J. X., Simcoe R. A., Myers A., Lau M. W., 2015, *Dissecting the Gaseous Halos of z ∼ Damped Lyα Systems with Close Quasar Pairs*, ApJ, 808, 38

Scannapieco E., Broadhurst T., 2001, *Linking the Metallicity Distribution of Galactic Halo Stars to the Enrichment History of the Universe*, ApJ, 550, L39

Scannapieco E., Brüggen M., 2015, *The Launching of Cold Clouds by Galaxy Outflows. I. Hydrodynamic Interactions with Radiative Cooling*, ApJ, 805, 158

Scannapieco E., Oh P., 2004, in American Astronomical Society Meeting Abstracts. p. 94.21

Scannapieco E., Thacker R. J., Davis M., 2001, *High-Redshift Galaxy Outflows and the Formation of Dwarf Galaxies*, ApJ, 557, 605

Schneider E. E., Robertson B. E., Thompson T. A., 2018, *Production of Cool Gas in Thermally Driven Outflows*, ApJ, 862, 56

Schneider E. E., Ostriker E. C., Robertson B. E., Thompson T. A., 2020, *The Physical Nature of Starburst-driven Galactic Outflows*, ApJ, 895, 43

Shen S., Madau P., Aguirre A., Guedes J., Mayer L., Wadsley J., 2012, *The Origin of Metals in the Circumgalactic Medium of Massive Galaxies at z = 3*, ApJ, 760, 50

Shopbell P. L., Bland-Hawthorn J., 1998, *The Asymmetric Wind in M82*, ApJ, 493, 129

Smith B., Sigurdsson S., Abel T., 2008, *Metal cooling in simulations of cosmic structure formation*, MNRAS, 385, 1443

Smith B. D., et al., 2017, *GRACKLE: a chemistry and cooling library for astrophysics*, MNRAS, 466, 2217

Somerville R. S., Hopkins P. F., Cox T. J., Robertson B. E., Hernquist L., 2008, *A semi-analytic model for the co-evolution of galaxies, black holes and active galactic nuclei*, MNRAS, 391, 481

Spergel D. N., et al., 2007, *Three-Year Wilkinson Microwave Anisotropy Probe (WMAP) Observations: Implications for Cosmology*, ApJS, 170, 377

Steidel C. C., Erb D. K., Shapley A. E., Pettini M., Reddy N., Bogosavljević M., Rudie G. C., Rakic O., 2010, *The Structure and Kinematics of the Circumgalactic Medium from Far-ultraviolet Spectra of z ∼= 2-3 Galaxies*, ApJ, 717, 289

Stewart K. R., Kaufmann T., Bullock J. S., Barton E. J., Maller A. H., Diemand J., Wadsley J., 2011, *Orbiting Circumgalactic Gas as a Signature of Cosmological Accretion*, ApJ, 738, 39

Strickland D. K., Heckman T. M., 2009, *Supernova Feedback Efficiency and Mass Loading in the Starburst and Galactic Superwind Exemplar M82*, ApJ, 697, 2030

Su M., Slatyer T. R., Finkbeiner D. P., 2010, *Giant Gamma-ray Bubbles from Fermi-LAT: Active Galactic Nucleus Activity or Bipolar Galactic Wind?*, ApJ, 724, 1044

Suresh J., Rubin K. H. R., Kannan R., Werk J. K., Hernquist L., Vogelsberger M., 2017, *On the OVI abundance in the circumgalactic medium of low-redshift galaxies*, MNRAS, 465, 2966

Tchernyshyov K., et al., 2021, *The CGM^2 Survey: Circumgalactic O VI from dwarf to massive star-forming galaxies*, arXiv e-prints, p. arXiv:2110.13167

Teşileanu O., Mignone A., Massaglia S., 2008, *Simulating radiative astrophysical flows with the PLUTO code: a non-equilibrium, multi-species cooling function*, A&A, 488, 429

Tepper-García T., Bland-Hawthorn J., Sutherland R. S., 2015, *The Magellanic Stream: Break-up and Accretion onto the Hot Galactic Corona*, ApJ, 813, 94

Thompson T. A., Fabian A. C., Quataert E., Murray N., 2015, *Dynamics of dusty radiation-pressure-driven shells and clouds: fast outflows from galaxies, star clusters, massive stars, and AGN*, MNRAS, 449, 147

Thompson T. A., Quataert E., Zhang D., Weinberg D. H., 2016, *An origin for multiphase gas in galactic winds and haloes*, MNRAS, 455, 1830

Tremonti C. A., et al., 2004, *The Origin of the Mass-Metallicity Relation: Insights from 53,000 Star-forming Galaxies in the Sloan Digital Sky Survey*, ApJ, 613, 898

Tumlinson J., Peeples M. S., Werk J. K., 2017, *The Circumgalactic Medium*, ARA&A, 55, 389

Turk M. J., Smith B. D., Oishi J. S., Skory S., Skillman S. W., Abel T., Norman M. L., 2011, *yt: A Multi-code Analysis Toolkit for Astrophysical Simulation Data*, The Astrophysical Journal Supplement Series, 192, 9

Vázquez G. A., Leitherer C., 2017, in Charbonnel C., Nota A., eds, Vol. 316, Formation, Evolution, and Survival of Massive Star Clusters. pp 359–360, doi:10.1017/S1743921315009230

Veilleux S., Rupke D. S., 2005, in Braun R., ed., Astronomical Society of the Pacific Conference Series Vol. 331, Extra-Planar Gas. p. 313

Veilleux S., Cecil G., Bland-Hawthorn J., 2005, *Galactic Winds*, ARA&A, 43, 769

Veilleux S., Rupke D. S. N., Swaters R., 2009, *Warm Molecular Hydrogen in the Galactic Wind of M82*, ApJ, 700, L149

Vikhlinin A., Kravtsov A., Forman W., Jones C., Markevitch M., Murray S. S., Van Speybroeck L., 2006, *Chandra Sample of Nearby Relaxed Galaxy Clusters: Mass, Gas Fraction, and Mass-Temperature Relation*, ApJ, 640, 691

Vogelsberger M., et al., 2014, *Introducing the Illustris Project: simulating the coevolution of dark and visible matter in the Universe*, MNRAS, 444, 1518

Wakker B. P., Savage B. D., Fox A. J., Benjamin R. A., Shapiro P. R., 2012, *Characterizing Transition Temperature Gas in the Galactic Corona*, ApJ, 749, 157

Walch S., Naab T., 2015, *The energy and momentum input of supernova explosions in structured and ionized molecular clouds*, MNRAS, 451, 2757

Wang B., 1995, *Cooling Gas Outflows from Galaxies*, ApJ, 444, 590

Werk J. K., et al., 2014, *The COS-Halos Survey: Physical Conditions and Baryonic Mass in the Low-redshift Circumgalactic Medium*, ApJ, 792, 8

Werk J. K., et al., 2016, *The COS-Halos Survey: Origins of the Highly Ionized Circumgalactic Medium of Star-Forming Galaxies*, ApJ, 833, 54

Xu J., Stone J. M., 1995, *The Hydrodynamics of Shock-Cloud Interactions in Three Dimensions*, ApJ, 454, 172

Yoshida M., Kawabata K. S., Ohyama Y., 2011, *Spectropolarimetry of the Superwind Filaments of the Starburst Galaxy M 82: Kinematics of Dust Outflow*, Publ. Astron. Soc. Japan, 63, 493

Zhu G., Ménard B., 2013, *The JHU-SDSS Metal Absorption Line Catalog: Redshift Evolution and Properties of Mg II Absorbers*, ApJ, 770, 130

Zolotov A., et al., 2012, *Baryons Matter: Why Luminous Satellite Galaxies have Reduced Central Masses*, ApJ, 761, 71

de la Cruz L. M., Schneider E. E., Ostriker E. C., 2021, *Synthetic Absorption Lines from Simulations of Multiphase Gas in Galactic Winds*, ApJ, 919, 112